

Imperial College London
Physics Department
Photonics Group

**Advanced Laser Sources
for Industrial Processing
and Remote Sensing**

Achaya Teppitaksak

Thesis submitted in partial fulfilment of the requirements for the degree
of Doctor of Philosophy of Imperial College London

January 2015

I declare that the work presented in this thesis is my own. Information derived from the work of others has been acknowledged in the text and a list of references is supplied at the end of the thesis.

Copyright

The copyright of this thesis rests with the author and is made available under a Creative Commons Attribution Non-Commercial No Derivatives licence. Researchers are free to copy, distribute or transmit the thesis on the condition that they attribute it, that they do not use it for commercial purposes and that they do not alter, transform or build upon it. For any reuse or redistribution, researchers must make clear to others the licence terms of this work.

Acknowledgements

I am heartily thankful to my supervisor, Prof. Mike Damzen for giving me the opportunity to work in his lab and for the encouragement, supervision and support from start of my PhD to the finish which enabled me to develop a deeper understanding of the subject.

Furthermore, I would like to thank Ara, Emma, and Gabs for being such brilliant friends and for all their help in the lab. Special thanks goes to Gabs for sharing her cavity dumped Q-switching laser and Wenjun for designing and constructing a high temperature oven. I would also like to thank Simon, Martin, Judith and Marcia for being very helpful.

I would like to thank all of my PhD friends in the Photonics Group for being lovely and making these four years such a great experience and to all my friends from Thailand for making my lunches so much fun. Special thanks go to Graham, Hugh and my family for being supportive over the last few months of writing up.

Last but not least, the financial support of the Thai government is also gratefully acknowledged.

Abstract

In the fifty years since their discovery, the use of laser oscillators and amplifiers has increased to cover a wide range of applications. This thesis develops diode-pumped solid-state (DPSS) lasers for two main applications: industrial processing and remote sensing.

The first half of this thesis investigates the development of bounce geometry lasers that can be used to generate high power light sources suitable for industrial processing using diode-pumped Nd:YVO₄ laser sources at both 1342nm and 1064nm transitions. The first of these investigations develops bounce geometry configuration Nd:YVO₄ laser sources operating at 1342nm. For continuous wave (CW) operation at powers of 15.9W with 30% optical-to-optical efficiency were achieved. For pulsed operation, Q-switching based on an acousto-optic modulator and mode-locking based on nonlinear-mirror mode-locking were demonstrated.

To suit a range of different industrial applications, a versatile gain switched laser diode source at a wavelength of 1064nm was developed to have independently adjustable pulse energies, pulse duration and repetition rates. To reach a commercially useful power level, a seed laser was amplified in a master oscillator power amplifier (MOPA) configuration using two ultrahigh-gain Nd:YVO₄ bounce amplifiers in series. In a first amplifier (preamplifier), a small-signal gain of ~50dB with good TEM₀₀ beam quality preservation was achieved with 24W pumping while a second power amplifier was used to achieve an average output power of up to ~14W using an input seed power of 188μW.

The second part of this thesis develops laser sources for remote sensing applications based on direct diode pumping of Alexandrite lasers in an end-pumping configuration. When compared to Q-switched Nd:YAG lasers, which are typically used for satellite based remote sensing, Alexandrite lasers have the potential to be more efficient and offer more flexible wavelength tunability. Following a broad

overview of Alexandrite lasers, this thesis investigates diode-pumped Alexandrite laser performance. To achieve a high average power, a compact laser cavity was built with output power as high as 26.2W and slope efficiency of 49%. This was more than an order of magnitude higher than previously reported from diode pumped Alexandrite lasers. To achieve TEM₀₀ laser output, many extended cavity designs were investigated.

Following this, to enhance the laser efficiency, an Alexandrite laser was developed utilizing the unique characteristics of temperature-dependent gain of Alexandrite and the performance from 20-150°C was characterised. To demonstrate high pulse energies, suitable for remote sensing applications, for the first time, a direct diode pumping Q-switched Alexandrite was demonstrated. A Q-switched output pulse energy of >1mJ at 100Hz pulse repetition rate in TEM₀₀ mode was achieved.

Publications

Journal Papers

1. **A Teppitaksak**, G. M. Thomas, and M. J. Damzen, "Investigation of a versatile pulsed laser source based on a diode seed and ultra-high gain bounce geometry amplifiers.," *Opt. Express*, vol. 23, no. 9, pp. 12328–36, May 2015.
2. **A. Teppitaksak**, A. Minassian, G. M. Thomas, and M. J. Damzen, "High efficiency >26 W diode end-pumped Alexandrite laser.," *Opt. Express*, vol. 22, no. 13, pp. 16386–92, 2014.

Conference Submissions

1. M. J. Damzen, G. M. Thomas, **A. Teppitaksak**, E. Arbabzadah, W. Kerridge-Johns, and A. Minassian, "Diode-Pumped Alexandrite Laser—a new prospect for Remote Sensing. In Conference on Lasers and Electro-Optics/Pacific Rim (p. 25B3_2). Optical Society of America, 2015
2. G. M. Thomas, A. Minassian, **A. Teppitaksak**, and M. J. Damzen, "High Energy Q-switching and Cavity Dumped Q-switching of a Diode-pumped Alexandrite Laser," in *Advanced Solid State Lasers*, (Optical Society of America, talk, paper ATu3A.7. 2015
3. **A. Teppitaksak**, G. M. Thomas, and M. J. Damzen, "Gain-switched diode laser seeding of ultra-high-gain Nd:YVO₄ bounce amplifier system as a versatile pulsed laser source," in *2015 European Conference on Lasers and Electro-Optics - European Quantum Electronics Conference*, (Optical Society of America, talk , paper CA_3_4, 2015
4. M. Damzen, **A. Teppitaksak**, G.M. Thomas, and A. Minassian, Progress in diode-pumped Alexandrite lasers as a new resource for future space Lidar missions. In International Conference on Space Optics, Vol. 7, p. 10, OCT 2014
5. **A. Teppitaksak**, G. M. Thomas, and M. J. Damzen, High efficiency diode-pumped Alexandrite laser for remote sensing", In Photon14 (p.5) Poster, 2014
6. M. J. Damzen, **A. Teppitaksak**, G. M. Thomas, A. Minassian, Highest power and Q-switched diode end-pumped Alexandrite laser, 6th EPS-QEOD Europhoton Talk ThD-T1-O-06, 2014
7. **A. Teppitaksak**, G. M. Thomas, and M. J. Damzen (2013, May). Versatile Pulsed Source using a pulsed diode seed and ultrahigh gain bounce geometry amplifier. In Lasers and Electro-Optics Europe (CLEO EUROPE/IQEC), Poster, 2013

Contents

1	Introduction.....	11
1.1	Background.....	11
1.2	Diode Pump Solid-State Laser.....	12
1.2.1	Laser Diode.....	13
1.2.2	Solid-State Material.....	15
1.3	Diode Pumped Solid-State Laser Geometries.....	18
1.3.1	Rod.....	19
1.3.2	Slab.....	20
1.3.3	Thin Disk.....	21
1.4	Thermal Effects.....	22
1.4.1	The Generation of Heat.....	22
1.4.2	Impact of Heating on Laser Operation.....	24
1.4.3	Cavity Stability.....	25
1.5	Pulse Operation.....	29
1.6	Q-Switching.....	29
1.6.1	Method of Q-Switching.....	30
1.7	Mode-locking.....	34
1.7.1	Methods of Mode-locking.....	36
1.8	Gain Switching.....	41
1.9	Thesis Outline.....	42
2	Bounce Geometry Laser.....	45
2.1	Introduction.....	45
2.2	Bounce Geometry.....	46
2.2.1	Bounce Geometry Concept.....	47
2.2.2	Laser Gain Media.....	48
2.2.3	Thermal Effect.....	50
2.3	Bounce Geometry Nd:YVO ₄ Demonstration of 1342nm Transition.....	52
2.3.1	CW Multimode Operation.....	53
2.3.2	CW Single Mode Operation.....	54
2.3.3	Q-switching Operation.....	56
2.4	Nonlinear Mirror Mode-Locking.....	59
2.4.1	Nonlinear Mirror Mode-Locking Technique.....	60

2.4.2	Extended Cavity for NLM Mode-locking Setup.....	61
2.4.3	Experimental Results.....	62
2.5	Conclusion.....	64
3	Versatile Pulse Laser Sources for Industrial Applications	66
3.1	Introduction.....	66
3.2	Experimental Systems.....	67
3.2.1	Pulsed Laser Seed System.....	68
3.2.2	Preamplifier and Power Amplifier.....	71
3.2.3	Theoretical Analysis of Bounce Geometry Amplifier.....	72
3.3	Experimental Results.....	74
3.3.1	Preamplifier Results.....	74
3.3.2	Power Amplifier Results.....	77
3.4	Conclusion.....	81
4	Alexandrite Laser	83
4.1	Introduction.....	83
4.2	Alexandrite Physical Properties.....	86
4.3	Alexandrite Laser Properties.....	88
4.3.1	Energy Levels.....	88
4.3.2	Temperature Dependent Characteristics.....	91
4.3.3	Excited State Absorption (ESA).....	93
4.4	Pump Sources for Alexandrite.....	94
4.5	Thermal Effect for End Pumped Laser Geometry.....	97
4.6	Alexandrite Applications.....	100
4.6.1	Current Applications.....	100
4.6.2	Potential Applications.....	101
4.7	Conclusion.....	102
5	Preliminary Design and Operation of Alexandrite Lasers	103
5.1	Introduction.....	103
5.2	Pump Laser Diode.....	104
5.3	Alexandrite Laser Crystal.....	105
5.4	Compact Laser Cavity.....	106
5.4.1	CW Operation.....	107
5.4.2	Quasi-CW Operation.....	109
5.4.3	Lasing Wavelength.....	110
5.4.4	Beam Quality.....	110

5.4.5	Intracavity Loss	111
5.5	Extended Cavity for Single Mode Operation	112
5.5.1	Extended Compact Cavity.....	112
5.5.2	Extended Cavity with Internal Spherical Lens.....	114
5.5.3	Double-End-Pumping.....	117
5.6	Spectral Properties of Alexandrite.....	119
5.6.1	Wavelength Tuning	120
5.7	Comparison to Side Pumping in a Bounce Geometry	122
5.8	Conclusion	124
6	Enhanced Alexandrite Laser Towards Remote Sensing Application	126
6.1	Introduction	126
6.2	Diode Pumped Beam Shaping.....	128
6.3	High Temperature Alexandrite Crystal Operation.....	130
6.3.1	Temperature Control Oven.....	130
6.3.2	Laser Performance.....	131
6.4	Q-Switching.....	137
6.4.1	Q-switching for Alexandrite Laser System	138
6.4.2	Q-switching Experimental Results.....	142
6.4.3	Pulse Duration and Pulse Build Up Time.....	151
6.5	Second Harmonic Generation.....	152
6.6	Conclusion	155
7	Conclusion	158
7.1	Bounce Geometry Oscillator	158
7.1.1	Summary	158
7.2	Versatile Pulse Laser Sources for Industrial Applications	159
7.2.1	Summary	159
7.2.2	Future work	160
7.3	Alexandrite Lasers	160
7.3.1	Summary	160
7.3.2	Future Work	163
8	References.....	164

1 Introduction

1.1 Background

Over fifty years of development since 1960 [1], lasers today are used in a variety of applications. Lasers have created a whole new generation of telecommunications via optical fiber [2]. Lasers also allow us to store a large amount of information effectively via optical storage on CD, DVD or Blu-ray disk [3][4]. In the industrial world, lasers play important roles in manufacturing such as cutting, drilling, and welding [5]. Lasers are also used in many medical applications such as eye surgery (LASIK) and dermatology [6]. These are just some examples, there are a lot of other applications not mentioned here, such as scientific research, and laser displays. Laser-based remote sensing itself leads to applications in many fields such as atmospheric monitoring, metrology and military [7]

The advancement of lasers is an achievement from the many contributions of scientists and engineers over the last century. Among these works, one of the important steps forward was the principal mechanism of a laser called stimulated emission, first proposed by Einstein in 1917 [3]. It was, however, almost 40 years after that when Charles Townes first successfully demonstrated the principle experimentally [8]. They successfully generated electromagnetic radiation via stimulated emission in the microwave region of the electromagnetic spectrum, which was referred to as a “Maser”. Based on the theoretical work of Townes and Schawlow, Maiman demonstrated the generation of EM radiation in the optical region, calling it an “optical maser” (Microwave Amplified by Stimulated Emission Radiation) [1], [9]. Subsequently, the name was changed to “laser”. This name is used as a general term for radiation in infrared, visible and ultraviolet region. The first “Laser” emission was achieved by Maiman in 1960, using a ruby crystal as the gain medium [1]. Since then, a large number of lasers have been achieved using

gases, liquids and solid-state materials [10][11][12]. Lasers have been demonstrated in both continuous wave (CW) and pulsed operation, covering a range of wavelengths, beam qualities and output powers [13][12][14][15].

This thesis focuses on the development of solid-state lasers for applications in industry and remote sensing. It should be noted that while fiber lasers are also a type of solid-state laser, they are not developed in this work. To put the work in this thesis into context, this chapter provides some understanding of diode pumped solid-state lasers. The solid-state materials (host materials and active ions) and diode pumping geometries will be described. Thermal issues that can arise in a laser system will be presented. This includes the generation of heat, impact on laser oscillation and cavity stability. After that, some important methods to generate pulsed laser output, which will be used throughout this thesis, will be explained. These methods are Q-switching, mode-locking and gain switching.

1.2 Diode Pump Solid-State Laser

There are two main types of optical pump source for solid-state lasers: lamps and laser diodes [16]. Lamp pump sources can be divided into two categories, flash lamps and arc lamps. Flash lamps are designed for pulsed operation whilst arc lamps are capable of operating in continuous wave (CW). Both flash lamps and arc lamps are made of tubes filled with high-pressure discharge gas [17]. Lamp pumping has been widely used especially in high power laser due to simplicity and the relatively low cost per watt. However, lamp pumping often has very low wall plug efficiency, typically less than a few percent. This is not only from low electrical to optical efficiency, but also low absorption efficiency since the light generated from both types of lamp is very broadband [16].

Compared to flash lamps or arc lamps, laser diodes have very narrow bandwidth (a few nm) [16]. By choosing a laser diode that matches the absorption line or band of a specific solid-state material, diode pumping can provide a significantly greater efficiency. As improvements in laser diode manufacturing techniques continue to

increase their power and reduce their cost, there is an increasing desire to use them as pump sources for commercial industrial lasers.

1.2.1 Laser Diode

Laser diodes are based on semiconductor materials, where one part is doped with electron donors (n-type) and another part is doped with electron acceptor (p-type) to form a p-n or p-i-n junction. The acronym ‘i’ is an intrinsic or undoped layer. When current flows through this region, electrons-holes recombine and release energy in form of photons. Optical feedback is achieved from cleaving the edge of the semiconductor medium to form a Fabry-Pérot resonator for laser oscillation. Figure 1.1 shows a schematic of an internal structure gain guided diode laser. An active layer in the vertical direction is around $0.005\text{-}0.02\mu\text{m}$ and it is confined by a multilayer of a structure of p-n junction [17].

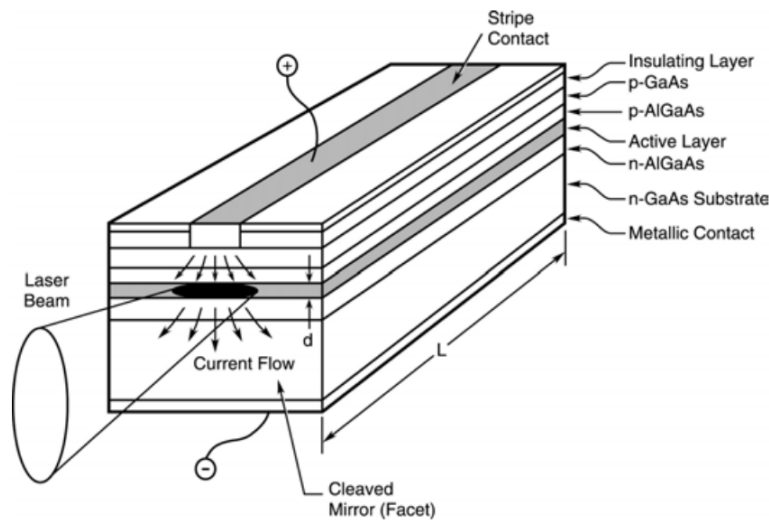


Figure 1.1: Schematic diagram of an internal structure of gain guided heterojunction laser diode [16].

The optical mode size in this vertical dimension $\sim 1\mu\text{m}$ with near diffraction limited beam quality and beam divergence of $\sim 40^\circ$ [17]. The gain region in a horizontal direction can be various sizes, typically much larger than in a vertical direction. For single mode emitter this width is $\sim 3\text{-}10\mu\text{m}$. For higher power, larger emitter widths are required to prevent optical damage to output facet, typical widths from $50\text{-}200\mu\text{m}$. The output in the horizontal is usually several times diffraction limited

with a beam divergence of $\sim 10^\circ$ [17]. This makes the output of laser diode highly non-symmetric. In practice, a micro lens is usually attached at the front face of the laser diode to reduce the divergence angle in a vertical direction.

The emission wavelength of a laser diode depends on the energy band gap which is determined by the internal structure and the chemical composition of the semiconductors. The spectral bandwidth of laser diode is usually only a few nanometres [16]. However, laser diode emission wavelength is very sensitive to temperature. The wavelength of a laser diode is shifted with temperature, typically $\sim 0.3\text{nm}/^\circ\text{C}$ [16]. Table 1.1 shows some important wavelengths available from commercial diode lasers.

Material/Substrate	Typical emission wavelength [nm]
AlGaAs/GaAs	720-850
InGaAsP/InP	1200-1650
InGaAs/GaAs	900-1100
InGaAlP/GaAs	630-700

Table 1.1: Important emission wavelengths for various semiconductor materials [18].

A laser diode with a single emitter usually provides output power with limited maximum power of a few watts as it is limited by the size of the gain region. Depending on the output power requirement, laser diodes can be combined to form one- or two-dimensional arrays to scale the output power to more than 1kW [16]. As well as the temperature dependence on the lasing wavelength, laser diodes require a cooling system due to large amounts of power being deposited in a small region as heat. For output powers less than 100W conduction cooling is sufficient, while a more complicated cooling system, typically in the form of micro-channels, is required for higher powers. Compared to flashlamps or arc lamps, laser diodes usually have comparatively long lifetime (\sim ten thousands of hours) [16]. However, like other semiconductor material, laser diodes are very sensitive to electro-static discharges and electrical transients. Precaution during handle a laser diode is required as a voltage spike could lead to degradation of a laser diode or even destroy a laser diode permanently [16].

1.2.2 Solid-State Material

The gain medium of a solid-state laser is comprised of a solid-state material (or so called host material) doped with an active ion. A host material tends to define the macroscopic properties while the active ion defines microscopic properties [17]. This section will present some important host materials and active ions in solid-state laser materials.

1.2.2.1 Host material

The host material is important as it tends to define macroscopic properties of a solid-state laser such as thermal-mechanical behavior, refractive index and fracture limit. Moreover, host material also affects gain bandwidth, lifetime and lasing wavelength of a laser [17]. There are many desirable properties for a host material, which can be summarized as follows: (1) good optical quality such as high transparency at the lasing wavelength and high homogeneity of refractive index; (2) good thermal properties such as high conductivity and low thermo-optic coefficient; (3) good mechanical properties such as hardness, low sensitivity to mechanical stress and have a high optical damage threshold allowing high power operation; (4) a host material must accept an active ion; (5) can be made to have a high doping concentration without losing optical quality [17].

The two main types of host material in solid-state lasers are crystals and glasses. In general, crystals are a preferable choice of host material due to higher emission cross-sections and higher thermal conductivities [17]. Crystals also tend to have narrower bandwidth and higher hardness. However, crystals tend to have poorer optical quality and inhomogeneous doping [17]. There are a large number of oxide crystal hosts available, common examples are:

- Sapphire e.g. Al_2O_3 : Sapphire has exceptional thermal mechanical properties offering high thermal conductivity and hardness. Sapphire can cooperate with a transition ion such as Cr^{3+} or Ti^{3+} [19][1]. The first laser is, in fact, based on sapphire doped with transition metal $\text{Cr}^{3+}:\text{Al}_2\text{O}_3$ or ruby. $\text{Ti}:\text{Sapphire}$, which is $\text{Ti}^{3+}:\text{Al}_2\text{O}_3$, is one of the most important lasers, offering a large tunability range.

- Garnets e.g. $\text{Y}_3\text{Al}_5\text{O}_{12}$ (YAG), $\text{Gd}_3\text{Ga}_5\text{O}_{12}$ (GGG): Garnets are isotropic crystals which offer good hardness and high thermal conductivity. Garnets can cooperate with a large number of rare earth ions such as Nd^{3+} , Tm^{3+} , Er^{3+} , Ho^{3+} and Yb^{3+} offering an various emission wavelengths in the infrared region [20][21][22][23]. YAG doped with Nd^{3+} in particular is one of the most commonly used solid-state lasers emitting a wavelength around $1\mu\text{m}$. Technology of fabrication of Nd^{3+} :YAG has been well developed offering high output power [24][25].
- Vanadates e.g. YVO_4 and GdVO_4 : Vanadate also offers good hardness and high thermal conductivity. Besides, vanadate is naturally birefringent, which could reduce the effect of thermally-induced depolarization losses. Similar to garnets, vanadates can cooperate with many rare-earth ions [26][27][28]. The most popular vanadate laser is Nd^{3+} : YVO_4 , offering very high emission cross-section and broad absorption bandwidth.

Another group of crystal host is fluoride crystals. Compared to oxide crystals, fluoride crystals typically have poorer thermal conductivity and mechanical properties [17]. Their thermo-optic dn/dT value can be better and in some cases are negative in value. Fluorides are often doped with transition active ions Cr^{3+} such as Cr:LiCAF and Cr:LiSAF offering tunable laser application. Fluorides can cooperate with rare-earth ions, however, the growing process is more complicated [29]. An important fluoride crystal is yttrium lithium fluoride YLiF_4 (YLF), and mainly doped with Nd^{3+} . Nd:YLF offer a reduction of thermal lensing due to negative value of dn/dT .

Another group is ceramics. Unlike crystals listed above which are monocrystalline, ceramics are made of aggregated crystalline grains [17]. Ceramic host material has recently gained interest due to improved fabrication techniques that have reduced scattering losses and allowed higher doping. An important example is Nd:YAG ceramic [24][30]. As well as higher doping, it is also possible to makes very large Nd:YAG ceramic gain media, than would be possible to grow (or too high cost) by convenient means.

Glass is comparatively easier to fabricate compared to crystals. A capability to produce a large size makes glass host crystal ideal for very high power operation. An average output power of over kilowatt has been achieved [31]. Glass host material can cooperate with various rare earth ions such as Nd^{3+} and Er^{3+} [32][31]. However, glass has very low thermal conductivity leading to optical distortion and thermally induced birefringence[17] [33] [34].

1.2.2.2 Active ions

Active ions define the microscopic properties of a laser such as the energy level structure, transition cross-section and upper state lifetime [17]. There are two groups of active ions: rare earth ions and transition metal ions. Rare earth ions have outer electrons shielded. Therefore rare earth ions exhibit very sharp fluorescence lines and their energy level structure changes only slightly for different host crystals. Transition metal ions, in contrast to rare earth ions, do not have their outer electrons shielded. Transition metal ions therefore exhibit broad fluorescence bands and the energy level structure is strongly affected by the crystal field host. The charge state of rare earth ions is mainly trivalent. Some important trivalent rare earth ions are:

- Neodymium (Nd^{3+}): Nd^{3+} is the most popular active ion as it provides higher emission cross section compared with other 4-level lasers [17]. The strongest emission wavelength of Nd^{3+} is $\sim 1\mu\text{m}$ while wavelengths of $\sim 0.9\mu\text{m}$ and $\sim 1.3\mu\text{m}$ are also available [35]. The wavelength of $\sim 1.1\mu\text{m}$ is the most important wavelength, covering various applications such as industrial, military and medical applications. Nd^{3+} has a strong absorption band around 808nm which can be pumped by a commercially available diode laser. Nd^{3+} has been incorporated into over 100 host materials. Some common host materials are Nd:YAG and Nd:YVO₄ [36][37].

- Erbium (Er^{3+}): Er^{3+} has two particularly interesting laser transitions at around $1.54\mu\text{m}$ and $2.94\mu\text{m}$. Emission at $2.94\mu\text{m}$ can be achieved from Er:YAG in a four-level transition. This wavelength matches with strong absorption of water, leading to many medical applications [23][38]. Emission around $1.54\mu\text{m}$ can be achieved from Er:glass in a quasi three-level transition. This wavelength is

interesting as it is in the “eye-safe” window, between 1.45-1.70 μm , which leads to many applications particularly in the fields of medicine and communications [39].

- Thulium (Tm^{3+}) and Holmium (Ho^{3+}): Tm^{3+} and Ho^{3+} emit a laser wavelength of 2.1 μm [40][41]. Tm^{3+} has high absorption at a wavelength of 785nm, which allows direct diode pumping. However, this has a very high quantum defect (785nm - 2 μm). Ho^{3+} has high absorption at a wavelength of 1.9 μm . Pumping at 1.9 μm is not straightforward due to no available diode laser at this wavelength, however, Ho^{3+} has a very low quantum defect offering good beam quality and the capability of power scaling.

Transition metal ions have no outer electron shielding and therefore, the electric field is strongly influenced by the lattice vibration quanta (phonons) of the host crystal field [17]. Unlike rare earth ions, the energy levels are spread into bands, leading to broad absorption and emission spectra. These are usually referred to as “vibronic lasers”, which not only offer wavelength tunability but also the potential to generate ultrashort pulses due to very large gain bandwidth. Two main transition metal ions are chromium (Cr^{3+}) and titanium (Ti^{3+}). Among vibronic lasers, Ti:Sapphire is the most popular gain medium due to a high emission cross section and very large tunability range (from 670-1070nm) [42]. Cr^{3+} doped lasers have a smaller tuning range (~100nm), with the centre wavelength shifted depending on the host crystal. Cr^{3+} also tends to have lower emission cross-section. However, Cr^{3+} has very good chemical stability and a broad absorption band [17]. This makes Cr^{3+} ions suitable to many laser hosts. Some important Cr-doped lasers are ruby ($\text{Cr}^{3+}:\text{Al}_2\text{O}_3$), alexandrite ($\text{Cr}^{3+}:\text{BeAl}_2\text{O}_4$), Cr:LiSAF and Cr:LiCAF.

1.3 Diode Pumped Solid-State Laser

Geometries

Diode pumping geometry is important as it determines how pump radiation transfers to a solid state gain medium. Laser geometry also defines how heat is removed which directly affects thermal gradient in the gain medium. Suitable laser

geometry results in high overall efficiency and good beam quality. Traditionally, the rod gain medium, which is the most common shape of gain medium, has been widely used in flash lamp pumping. Pumping can be easily done by placing a rod in an enclosed highly reflective material [17]. Laser diodes allow pumping either by longitudinal pumping (end-pumping) or transverse pumping (side-pumping) depending on the shape of the gain medium. This section will present pumping geometries for the three main shapes of solid state gain medium: rod, slab and thin disk.

1.3.1 Rod

A rod gain medium allows laser diode pumping either by end pumping or side pumping. In the end pumping configuration, as shown in Figure 1.2 (a), pump radiation is delivered along the resonator axis and heat is removed laterally. This geometry offers good spatial overlap between the pump radiation and the fundamental laser mode (TEM_{00}) leading to an excellent beam quality. Moreover, this geometry usually has low lasing threshold and high efficiency due to high pump density [43]. However, end-pumping suffers from severe thermal loading as the pump radiation is focused to a small area, leading to thermally induced effects which highly degrade the beam quality and finally limit the maximum output power [44].

Figure 1.2 (b) shows a schematic diagram of side pumped rod. Side pumping has the advantage of a larger pump area, leading to a decrease of thermal loading in the gain medium. Therefore, side pumping is suitable for high power operation, especially for $>100W$ output power [25][45]. In practice, a rod gain medium is usually side-pumped by several laser diodes. Compared to end pumping, it is more difficult to achieve TEM_{00} by side pumping due to poor overlap of the gain region with the fundamental mode. The efficiency is also usually lower as some pump energy is deposited outside the active gain region [25].

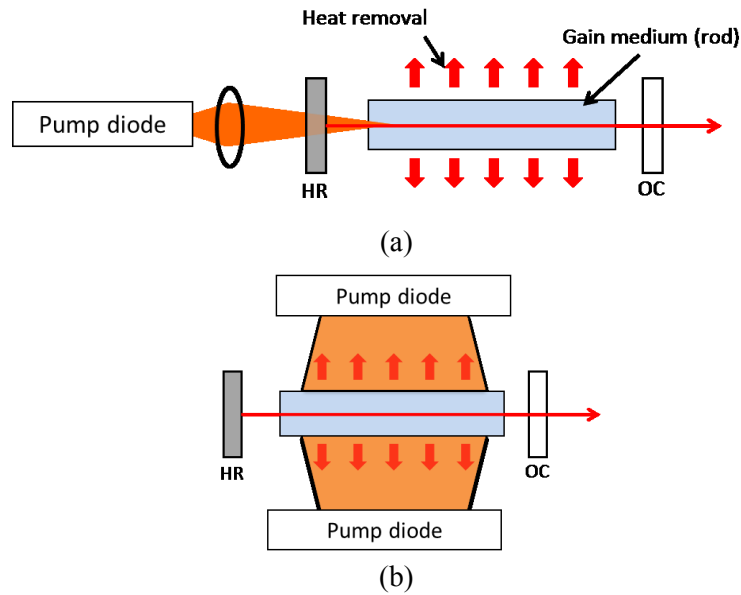


Figure 1.2: Schematic diagrams of rod pumping configurations for (a) end pumping and (b) side pumping.

1.3.2 Slab

A slab gain medium is a rectangular shaped gain medium with one very thin side compared to the other two dimensions. Compared to side pumping a rod gain medium, however, the slab gain medium allows very simple and straightforward construction by pumping at a narrow face (or two faces) of the crystal and conductively cooling from the large top and bottom faces of the crystal. Figure 1.3 shows a schematic diagram of a side pumping slab gain medium based on two geometries: (a) zig-zag geometry and (b) bounce geometry.

The zig-zag geometry was invented by Martin and Chernoch in 1969 [46]. Basically, the laser mode has multiple total internal reflections. This spatially averages the gain profile and the thermal distortion from the pump inside the slab resulting in a uniform output laser [24][47]. The edges of the slab are usually cut at the Brewster angle to minimize internal reflections.

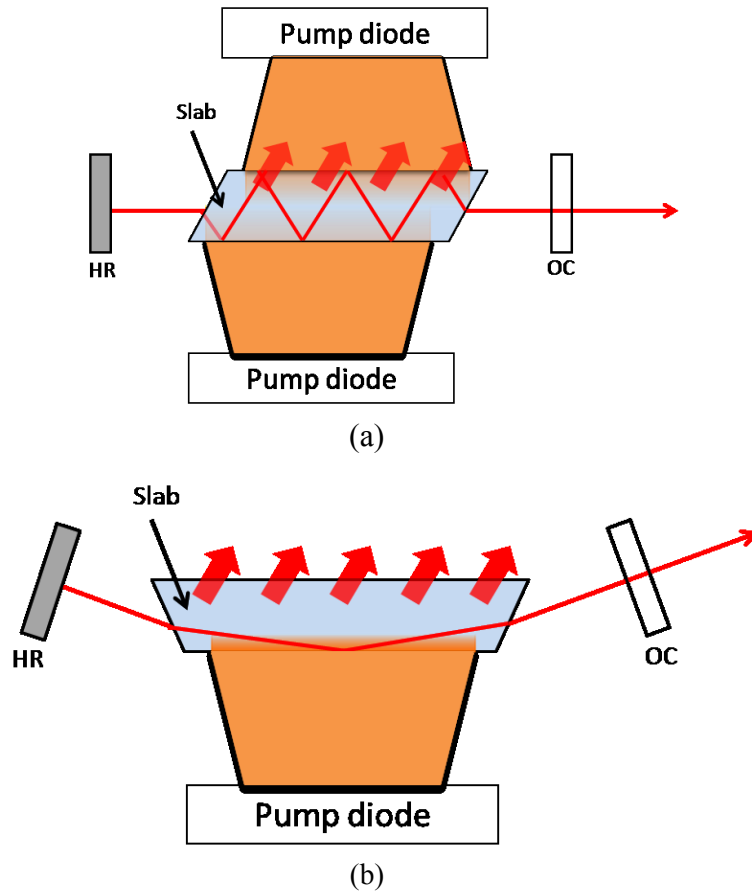


Figure 1.3: Schematic diagrams of slab pumping for (a) zig-zag configuration and (b) bounce geometry configuration

Bounce geometry is a special case where the laser mode has one total internal reflection at the pump face of the crystal [48]. This geometry has the advantage of averaging gain along the optical path like the zig-zag design. However, the bounce geometry is also usually operated at grazing-incidence TIR angle in highly absorbing gain media giving higher spatial matching with the highest pump density at the pump face of the gain medium. This leads to an extremely high gain and efficiency, along with good beam quality being achievable [49][50]. Further details of this geometric configuration will be presented in chapter 2.

1.3.3 Thin Disk

The thin disk gain medium offers a great power scaling capability for laser diode pumping, it was introduced by Giesen [51]. Figure 1.4 shows a schematic diagram

of a thin disk laser. As suggested by the name, the thin disk laser consists of a very thin gain medium ($\sim 100 \mu\text{m}$) with a large aperture attached to a heat sink. This leads to a uniform temperature distribution in the transverse direction (over pump face) and the heat flows only in the longitudinal direction. Therefore, the thin disk geometry reduces the effect of thermal distortion compared to other designs [52]. This allows pumping with extremely high power with minimum effect of thermal loading. This is particularly interesting for quasi 3-level lasers as high pump power is required. Moreover, power scaling using thin disk gain medium can easily be done by increasing pump area. An output power of over 1kW with 40% optical efficiency in a near fundamental mode has been reported based on a single disk [22].

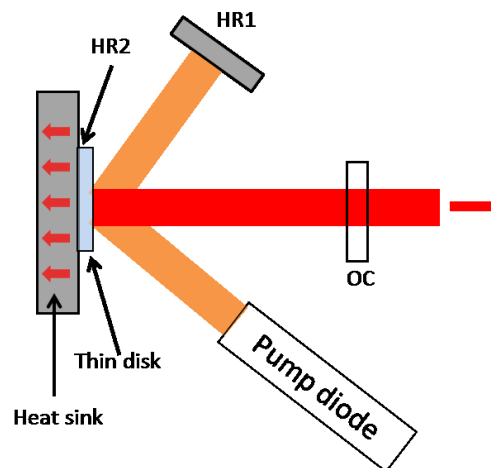


Figure 1.4: A schematic diagram of thin disk pumping configuration

1.4 Thermal Effects

1.4.1 The Generation of Heat

There are two mechanisms related to the decay of excited ions: radiative decay and non-radiative decay. Most of the absorbed pump energy gives rise to radiative decay, either by spontaneous emission or stimulated emission. However, some of the energy involves non-radiative decay where the energy dissipates in a vibration in the solid-state lattice, resulting in heating in the gain medium.

Most significant heating in solid-state lasers is generated from the quantum defect. The quantum defect is defined as the difference between the energy of the pump photon and the laser photon,

$$\Delta E = h\nu_{pump} - h\nu_{laser} = h\nu_{pump} \left(1 - \frac{\lambda_{pump}}{\lambda_{laser}}\right) \quad \text{Eq. 1.1}$$

The quantum defect arises from non-radiative decay of excited electrons, as shown in Figure 1.5 for energy diagrams for 3-level and 4-level laser systems. Quantum defect is an unavoidable loss, which therefore sets the upper limit of overall power conversion efficiency in a laser system. For a Nd:YAG laser emitting at 1064nm, with pumping by a diode laser at 808nm, 24% of the pump energy is lost, mostly as heat.

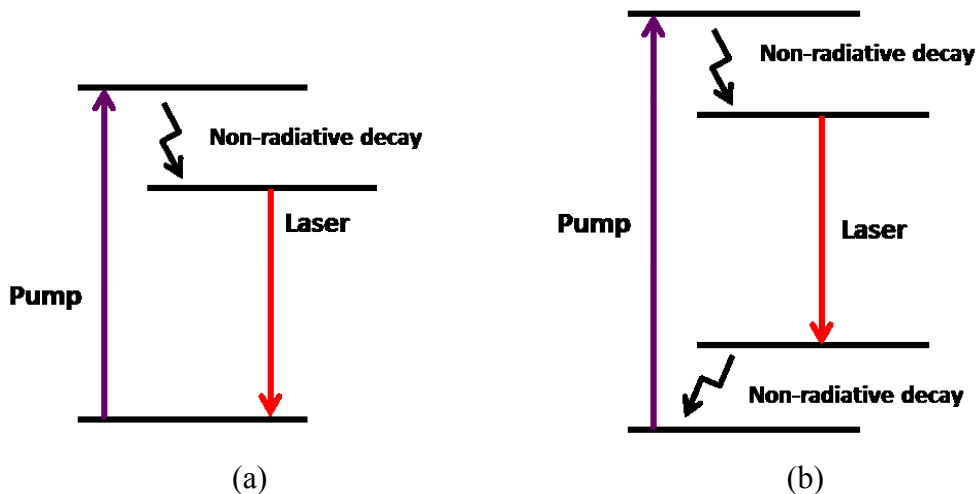


Figure 1.5: Energy diagram showing non-radiative decay in (a) three-level laser system and (b) four-level laser system.

Another process that generates heat in a laser system is excited state absorption (ESA). ESA is a process in which ions in the upper state level absorb photons to a higher excited state level, as shown in Figure 1.6(a). Ions from the higher upper state level either radiatively decay (usually at a wavelength shorter than the lasing wavelength) or non-radiatively decay to the upper state level resulting in heating in the gain medium [53]. ESA includes absorption from either pump photons or emission photons. This process is highly affects vibronic lasers due to the broad energy levels. This sometimes leads to shifting of the lasing wavelength from the peak gain cross section such as in Alexandrite lasers [54].

Heating could also be generated by energy transfer between ions in the gain medium. Two important processes that could lead to heat generation are cross relaxation and up-conversion. Cross-relaxation is the process whereby part of the energy of an ion in the upper state level transfers to an ion in the ground state level, as shown in Figure 1.6(b). This results in both ions ending up somewhere between the intermediate levels and generally non-radiatively decaying to the ground state level. The up-conversion process, on the other hand, occurs when the ions in the upper state level transfer all their energy to other ions in the same level. As shown in Figure 1.6(c), the ions that receive energy end up at a higher energy level while the ions that lose energy end up at the ground state level. The ion in the higher upper state level, similarly to ESA, decays either via radiative decay at shorter wavelengths or non-radiative decay to the ground state. In general, these processes are unwanted as the radiative decay does not contribute to the laser gain and the non-radiative decay losses cause heat in the gain medium.

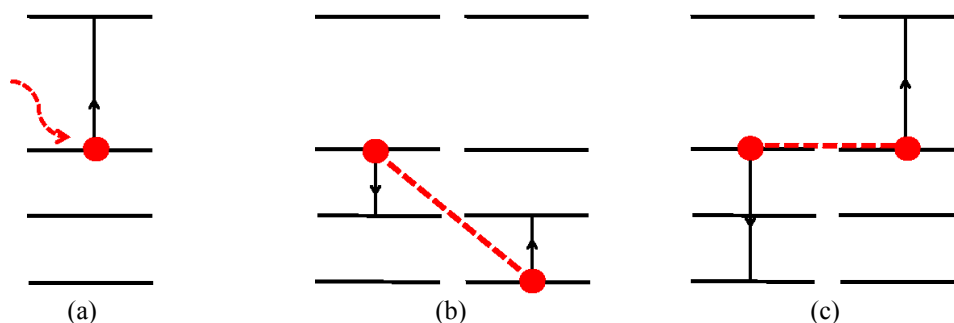


Figure 1.6: (a) Excited state absorption (b) Cross-relaxation and (c) Up-conversion

1.4.2 Impact of Heating on Laser Operation

Heating of the gain medium could lead to stress fracture of the gain medium [17]. This limits the maximum pump power and thus, the maximum continuous output power of a solid-state laser. In less extreme cases, heating causes a temperature gradient in the gain medium. Temperature gradients lead to lensing and stress induced birefringence optical distortion resulting in degradation of the output power and the beam quality [17]. Note that the thermal gradient in the laser gain medium depends on many parameters such as the gain material, pumping geometry and

cooling method. The thermal gradient of side pumping in a bounce geometry configuration and end pumping rod will be presented separately in section 2.2 and 4.5 respectively.

In general, thermal lensing is the most common problem that highly affects laser performance and cavity stability. Thermal lensing occurs from both refractive index changes due to temperature (a thermo-optic effect), refractive index changes from thermally induced mechanical stress (photoelastic-effect) and end-face curvature of the gain medium [17]. In a cylindrical rod, assuming uniform heat generation and the radial heat flow only, the effective focal length of the whole rod can be expressed by [17],

$$f = \frac{KA}{P_h} \left(\frac{1}{2} \frac{dn}{dT} + \alpha C_{r,\phi} n_0^3 + \frac{\alpha r_0 (n_0 - 1)}{l} \right)^{-1} \quad \text{Eq. 1.2}$$

where K is the thermal conductivity of the rod gain medium,

A is the rod cross-sectional area,

P_h is the total heat power dissipated in the rod,

α is the thermal expansion coefficient,

$C_{r,\phi}$ is the photo-elastic coefficient,

n_0 is the refractive index at the centre of the rod,

r_0 is the radius of the rod,

l is the rod length.

The first term in the bracket in Eq.1.2 represents the thermo-optic effect, the second term represents the photo-elastic effect and the last term represents the end-effect. Eq. 1.2 shows that the effective focal length of the thermal lensing is inversely-proportional to the pump power. Therefore, the dioptric power of the thermal lensing ($1/f$) increases proportionally with the pump power.

1.4.3 Cavity Stability

Thermal lensing affects the laser mode behaviour and laser cavity stability [55]. Cavity stability as a function of the dioptric power of the thermal lens is fully discussed by Magni [55]. Consider a simple cavity configuration, consisting of two curved mirrors with a rod gain medium in the cavity, as shown in Figure 1.7 (a). If

we are interested only in the beam profile outside the gain medium, the gain medium can be replaced with a thin lens in a middle of a rod, as shown in Figure 1.7 (b). The thin lens can be either a positive or negative lens depending on the thermo-optic coefficient (dn/dT) of the gain medium. As most gain media have a positive value the lens acts as a positive lens [55][17]. The cavity can be simplified further as a thin lens in a cavity, with a cavity arm length (L_1 and L_2) measured from a principal plane of a lens, as shown in Figure 1.7(c).

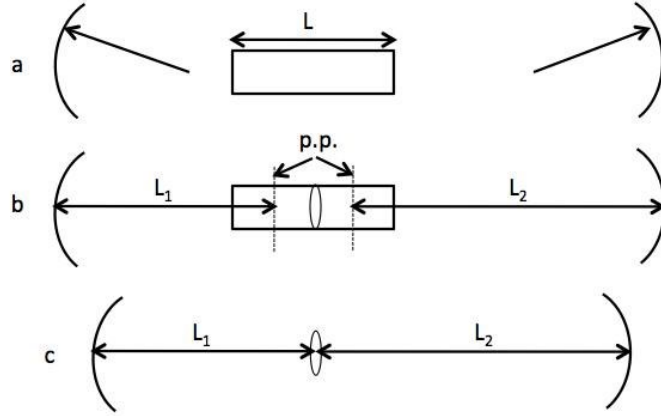


Figure 1.7: (a) Simple cavity containing a rod gain medium (b) thin lens placed at the middle of the rod representing thermal lens arising in the gain medium and p.p. are principal planes of the thermal lens and (c) Simplified equivalent cavity [55].

For a cavity with a thermal lens with focal length (f), the effective length of the resonator is defined as [55],

$$L_{eff} = L_1 + L_2 - \left[\frac{L_1 L_2}{f} \right] \quad Eq. 1.3$$

The cavity stability can be described in term of g-parameters, which are defined as [55],

$$g_1 = 1 - \frac{L_2}{f} - \frac{L_{eff}}{R_1}, \quad g_2 = 1 - \frac{L_1}{f} - \frac{L_{eff}}{R_2} \quad Eq. 1.4$$

where R_1 and R_2 are the radii of curvature of the mirrors, and are positive for concave mirrors. The stability condition can be written as [55],

$$0 \leq g_1 g_2 \leq 1 \quad Eq. 1.5$$

Figure 1.8 shows the stability diagram in terms of g-parameters. The shaded area represents two separated stable zones, referred to here as the positive g-region and the negative g-region. For a cavity consisting of two plane-plane mirrors, the radii of curvature, R_1 and R_2 , are equal to infinity. Thus, the g-parameters reduce to $g_1 = 1 - L_2 / f$ and $g_2 = 1 - L_1 / f$. Starting with no thermal lens ($f = \infty$), the cavity configuration is at point 1. As the pumping increases, the dioptric power increases and the cavity configuration moves linearly along a straight line. For a symmetric cavity where $L_1 = L_2$, the cavity moves along the solid lines through the two stability zones with no effect from the unstable region. The cavity is stable all the way until the thermal lens is too strong to support stable oscillation. However, for an asymmetric cavity, as the dioptric power increases, the cavity is initially stable in the positive g-region. For the case where $L_1 > L_2$, the cavity moves along the dotted line and becomes unstable as the thermal lens is between point 2 to 3. As the thermal lens increases, the cavity reaches the negative g-region at point 3. The cavity then becomes stable until the thermal lens increases and the edge of the stability zone is reached (point 4).

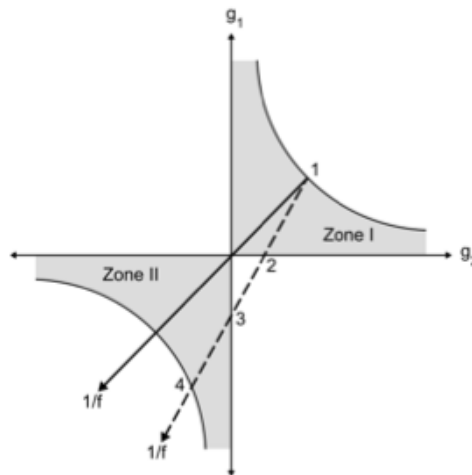


Figure 1.8: Stability diagram and mode profiles. The shaded area represents the stable region [55].

Another important parameter is the spot size in the gain medium. The spot size in the gain medium (w_g) determines the laser mode volume, which is related directly to the output power. The spot size at the gain medium taken to be the location of the intracavity (thermal) lens. The radius was measured from the beam axis to a

distance where the amplitude fell by 1/e from the maximum value. The spot size of a fundamental mode at the gain medium can be calculated by [55],

$$w_g^2 = \frac{\lambda}{\pi} \left[\frac{4u_1 u_2 g_1 g_2 + (u_1 - u_2)^2}{(1 - g_1 g_2) g_1 g_2} \right]^{1/2} \quad \text{Eq. 1.6}$$

where

$$u_1 = L_1 \left(1 - \frac{L_1}{R_1} \right), \quad u_2 = L_2 \left(1 - \frac{L_2}{R_2} \right) \quad \text{Eq. 1.7}$$

It can be seen that at the edge of the stability zone ($g_1 g_2 = 0$ or 1), the spot size goes to infinity. Figure 1.9 shows the spot size as a function of dioptric power. Two separated stability zones occur where the width ($\Delta(1/f)$) represents the ranges of dioptric power where the cavity is in the stable region. Besides, the spot size in the gain medium could also indicate how sensitive the cavity is to the thermal lensing [55]. The most stable point is obtained where w_g is minimum, which is the same

for both stability zones. By solving $\frac{dw_g}{d(1/f)} = 0$, the minimum spot size can be calculated by [55],

$$w_{g0}^2 = \frac{2\lambda}{\pi} \max(|u_1|, |u_2|) \quad \text{Eq. 1.8}$$

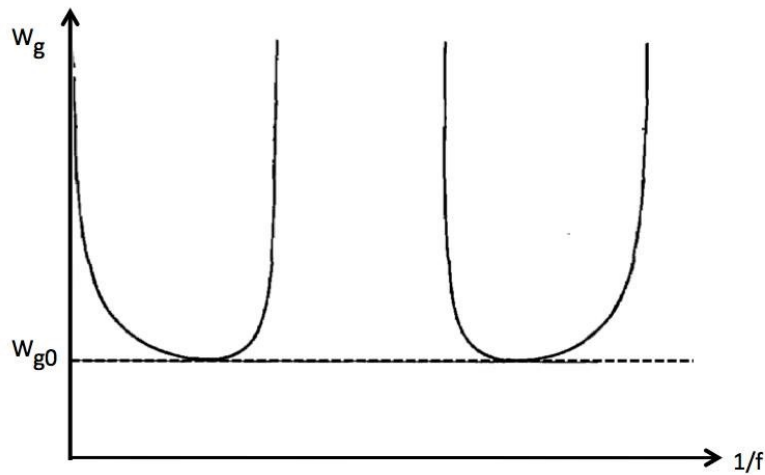


Figure 1.9: Spot size at the centre of the rod gain medium as a function of dioptric power

Therefore, the range of the stability zone and the minimum spot size $w_{g_0}^2$ of the fundamental mode depends on the radii of curvature (R_1, R_2) and cavity arm lengths. The cavity design to achieve the fundamental mode at high pump power by operating in the g-negative region of the stability zone will be shown in Chapter 2 and Chapter 5.

1.5 Pulsed Operation

There are many practical applications where a short and intense light pulse is more suitable than having the same amount of energy distributed over a longer time. This includes industrial processing, such as laser cutting and drilling, laser remote sensing and especially for nonlinear optical effects where a high peak power is required. There are several methods to produce pulsed lasers such as Q-switching, mode-locking and gain switching. Each method is suitable for a specific application, which may require different pulse properties such as pulse duration, pulse energy and repetition rate.

1.6 Q-Switching

Q-switching is a common method for producing a pulsed laser with a much higher peak power than when operating in a continuous wave (CW) mode [17]. The method allows the generation of pulses with a duration of nanoseconds (from sub-picosecond to hundreds of nanoseconds) and a peak power in the kilowatt to megawatt range [56][57]. Q-switching is implemented by modulating intracavity losses, or quality factor Q , of a laser resonator. The formation of a Q-switched pulse is illustrated in Figure 1.10. Assuming there is a shutter (or loss modulator) in the cavity, the shutter is initially “closed”. This produces high losses to the resonator and inhibits laser action. The large amount of energy from the pumping process is therefore stored in the gain medium. The maximum population inversion level (n_i) is much higher than when the laser is running in CW mode, which is just at

threshold value. After a certain time, the shutter is suddenly “opened” and the cavity loss rapidly reduces to a low value. The photon flux builds up exponentially and at the same time the population inversion is depleted. The photon flux reaches its peak when the population inversion is at the threshold. After this point, the net gain becomes lower than the loss. The inversion continues to decrease after this photon peak. The inversion decreases down to a final value (n_f), which occurs at the same time as the photon flux decreases to zero. As the photon flux in this process builds up rapidly, the giant Q-switched pulse is released in a short time. Note that the cavity dynamic described here is in the case of fast switching.

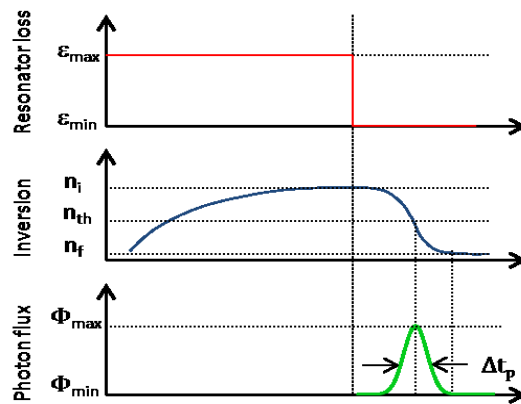


Figure 1.10: The development of a Q-switched pulse. The resonator loss, population inversion and photon flux as a function of time are shown [17].

The energy of Q-switching pulses depends upon the population inversion stored in the gain medium or more specifically, the difference of initial and final inversion ($n_i - n_f$). The population inversion increases with pump duration though it is limited by the upper state lifetime (τ) of the gain medium. The population inversion, when pumped for longer than this value, would decay in the form of spontaneous emission. Therefore, this method is best suited to gain media with a long upper state lifetime.

1.6.1 Method of Q-Switching

There are two methods that can be used to modulate losses in the cavity: Active Q-switching and Passive Q-switching. Active Q-switching requires an externally-modulated active element. The most commonly used techniques are

acousto-optic and electro-optic modulators. On the other hand, passive Q-switching occurs automatically without active operation. This technique based mainly on using a saturable absorber to introduce losses to the cavity.

1.6.1.1 Active Q-Switching

Active Q-switching requires an external active element to actively modulate losses. Two commonly used methods are based on acousto-optic (AO) or electro-optic (EO) Q-switching. In AO Q-switching, a piezoelectric transducer is used to generate an acoustic wave in the optical material. The other side of the optical material is cut at some angle and coated with an absorber in order to suppress the acoustic wave [18]. The strain from the acoustic wave creates a sinusoidal modulation of the refractive index of the optical material through the photoelastic effect. Thus, the optical material acts like an optical phase grating with the same period and proportional in amplitude to the acoustic wave. When the driving voltage to the transducer is on, some of the light incident on the optical material will be diffracted, which creates high losses in the cavity, as shown in Figure 1.11. When the driving voltage is off, the optical material allows full transmission and so the cavity is switched to low loss state.

AO-modulation has the advantages of low insertion loss (usually $<0.5\%$ per pass) and a low operating power. However, the switching time is quite long compared to EO modulators due to the acoustic transit time. Besides, losses created from diffraction are usually quite low, which could lead to a pulse break though for high gain materials.

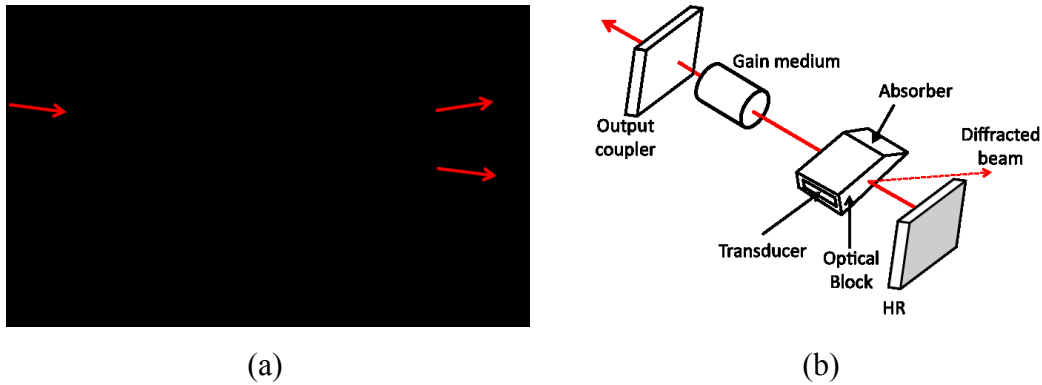


Figure 1.11: (a) Acousto optic modulator when the driving voltage is on. Light is partially diffracted (b) schematic diagram acousto-optic Q-switching cavity (adapted from [18])

Electro-Optic Q-switching exploits the electro-optic effect, also known as Pockels effect, to create changes in the refractive index of a crystal. For crystals that are non-centrosymmetric, the crystal exhibits an induced birefringence linearly with the external applied voltage. If linearly polarized light is incident on the birefringent crystal at 45° to the birefringence axes, the light will be resolved into two components, E_x and E_y . Each component experiences a different refractive index resulting in a different phase shift ($\Delta\phi$) after transmission through the crystal.

Figure 1.12 shows a common arrangement for the EO Q-switching setup. The system consists of a Pockels cell and a polarizer inserted between a gain medium and an output coupler. The Pockels cell is an Electro-Optic crystal attached with DC voltage. If the voltage is adjusted to create a phase shift, $\Delta\phi = \pi/2$, the Pockels cell will act like a quarter-wave plate leading to circular polarisation. After reflection from the mirror and a second pass through the Pockels cell, the light experiences another phase shift $\Delta\phi = \pi/2$, resulting in linear polarization. However, the polarization of the overall field is rotated by 90° to the original polarization which results in the light being reflected out of the cavity by the polarizer, creating a high loss level. When the applied voltage is switched off, the Pockels cell transmits the light without a change of polarization. Therefore, the cavity switches to a low loss level which allows a Q-switch pulse to build up.

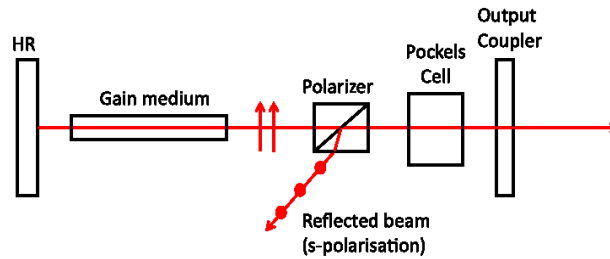


Figure 1.12: (a) Schematic diagram of EO Q-switching setup. Polarizer was inserted at Brewster angle to minimise the losses for p-polarization and to reflect light with s-polarisation.

1.6.1.2 Passive Q-switching

Passive Q-switching does not require active operation. The method relies on a saturable absorber to modulate losses in the cavity. A saturable absorber has a characteristic of nonlinear transmission at a laser wavelength according to the light intensity as shown in Figure 1.13. At low intensity, the saturable absorber initially absorbs the light creating high losses in the cavity, inhibiting laser oscillation. With increasing inversion the round trip gain exceeds the round trip losses, which are a combination of general intracavity losses and the loss created from the saturable absorber. The intracavity flux therefore increases dramatically. The saturable absorber is then rapidly saturated or bleached and becomes more transparent. As the same time, the cavity switches to a low loss level, and thus, the Q-switched pulse build up. Note that a suitable saturable absorber is required for high absorption/transmission at the lasing wavelength. For a wavelength of $\sim 1\mu\text{m}$, the most common saturable absorber $\text{Cr}^{4+}:\text{YAG}$.

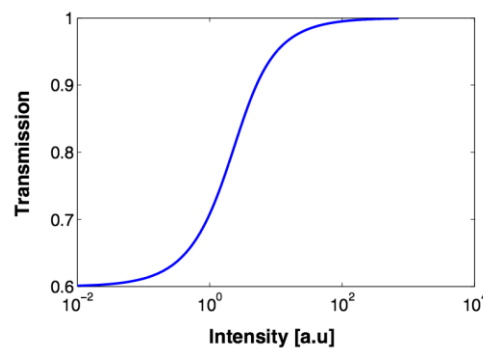


Figure 1.13: Nonlinear transmission as a function of light intensity of a saturable absorber

[17]

1.7 Mode-locking

Mode-locking is a technique for producing ultrashort pulses, typically in the range of femtoseconds to picoseconds. This method allows extremely short pulse duration compared to Q-switching as the pulse formation is controlled by manipulating the longitudinal modes of the laser rather than the dynamics of the gain medium.

In general, a laser can support a large number of longitudinal modes. Each mode is separated in frequency by $\Delta\nu = \frac{c}{2L}$, where L is the laser cavity length and c is the speed of light. In a non mode-locked laser, as shown in Figure 1.14 (a), each mode oscillates with a random phase relation. This results in a randomly fluctuating (short pulse) noise inside the laser cavity. For a large gain bandwidth gain medium, the short pulse noise is in the range of picoseconds or less. The laser output observed using a slow detector is a time-averaged value of this rapid intensity variation and therefore results in a nearly constant output power. In a mode locked laser, as shown in Figure 1.14 (b), each longitudinal mode oscillates with a fixed phase relation, which is known as “phase locked” or “mode locked”. At a position where the phase relation is zero, constructive interference of longitudinal modes produces a well-defined train of pulses. In a case of perfect mode-locking, all the modes are locked. The FWHM pulse duration ($\Delta\tau_p$) can be estimated by,

$$\Delta t_p \sim 1 / \Delta\nu \quad \text{Eq. 1.9}$$

where $\Delta\nu$ is the natural bandwidth of the pulse. This pulse duration is called “bandwidth limited” or “transform limited”, which indicates it is the minimum pulse duration achievable.

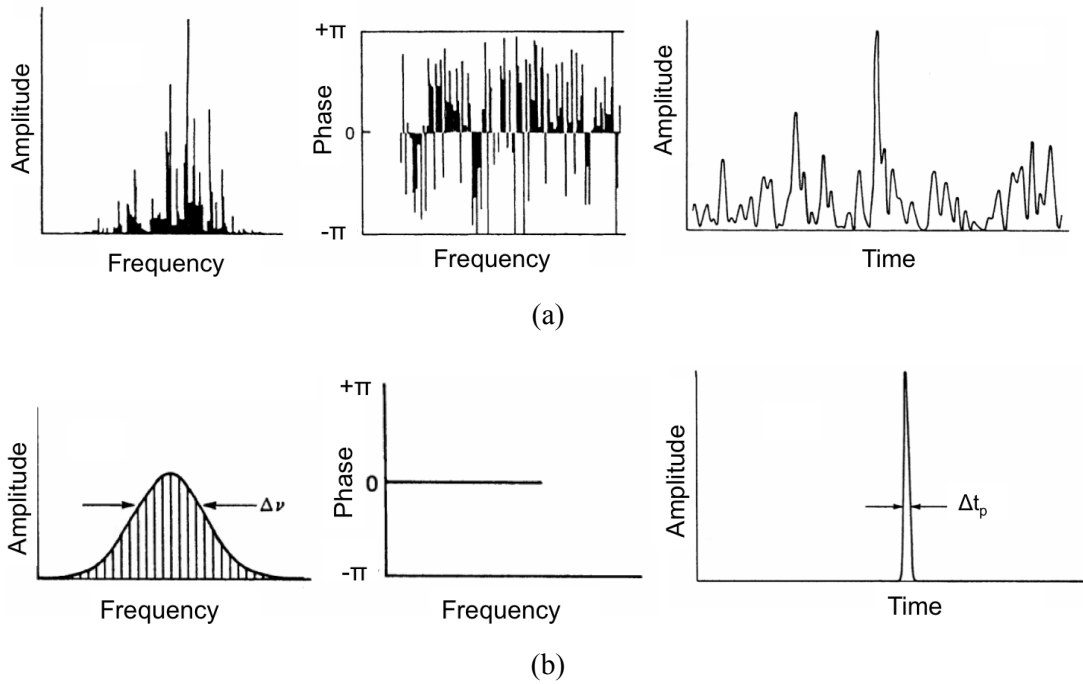


Figure 1.14: Signal structure in both time domain and frequency domain for (a) non-mode locked laser and (b) mode locked laser.

Mode-locking can also be explained in the time domain, as shown in Figure 1.15. Assuming there is an ultrafast optical shutter at one end of the cavity and unlike Q-switching, the ultrafast shutter can open and close with a period exactly equal the cavity round trip time $T_{cav} = 2L/c$. Therefore, only one light pulse survives within the cavity. The pulse travels in the cavity with the speed of light bouncing between the two mirrors. On each cavity round trip, some of the energy is released through the OC. Therefore, in the time domain picture, the mode locked laser is a train of pulses separated by the cavity round trip time.

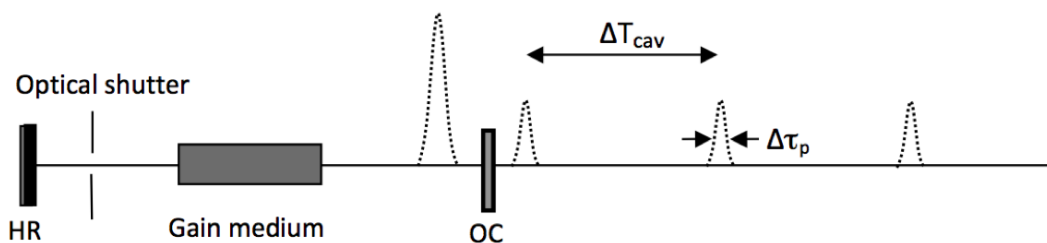


Figure 1.15: Time domain picture of mode-locking.

1.7.1 Methods of Mode-locking

Mode-locking can be divided into two categories: active mode-locking and passive mode-locking. Similarly to Q-switching, active mode-locking requires an external signal to modulate light while passive mode-locking exploits the nonlinearity of an optical element for self-modulation.

1.7.1.1 Active Mode-locking

Active mode-locking can be divided into two categories: amplitude modulated mode-locking (AM-mode-locking) and frequency modulated mode-locking (FM-mode-locking). Similar to Q-switching, AM mode-locking can be achieved with an acousto-optic modulator. The difference is that the AOM is driven by a sinusoidal signal in order to create a time varying loss with a period equal to the T_{cav} . Figure 1.16 (a) shows the mode coupling behavior in the case of AM mode-locking. In each cavity round trip, only one of the light pulses would build up at the time of minimum loss, assuming a modulator is placed at the end of the cavity. In this method, a pulse-shortening process occurs in each round trip as the leading and trailing edges of the light pulse experience some losses, while the peak of the light pulse experiences zero loss. The pulse shortening process will eventually be limited by the finite bandwidth of the gain medium.

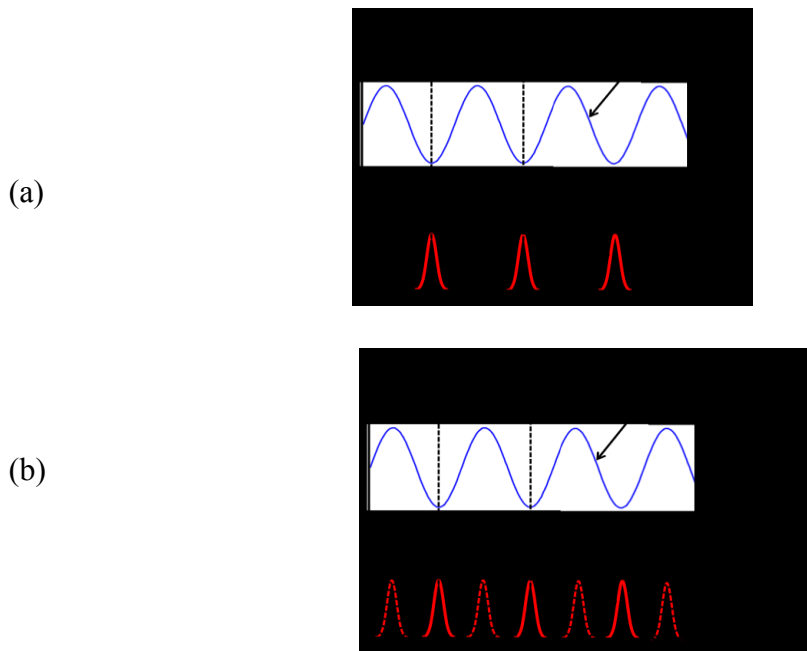


Figure 1.16: Steady state of mode-locking in time domain (a) AM mode-locking (b) FM mode-locking. Dotted red line pulse represent another possible mode that could occurred.

FM mode-locking is achieved by introducing an electro-optic element with a sinusoidal modulating signal to create a sinusoidally varying phase shift. Light passing through the EO element will experience some phase shift ($\Delta\phi$). After many repetitions, the frequency shift accumulates and is finally pushed out of the bandwidth of the gain medium. However, when the modulating signal is at the minimum or maximum, the light can pass through the modulator with no phase shift. The pulse can build up at these two positions, as shown in Figure 1.16 (b). The EO modulator introduces losses in the cavity in the same way as the amplitude modulation. However, switching between two modes sometimes occurs in practice. This leads to unstable mode-locking. Note that mode-locking can also be achieved by synchronous pumping. However, this technique is less widely used as it relies on pumping with another mode locked laser where precise matching of both of the cavity lengths is required.

1.7.1.2 Passive mode-locking

Passive mode-locking does not require an active element for modulating the signal. Self-modulation in passive mode-locking can be achieved from an intensity dependent loss mechanism within the cavity. Three important methods of passive mode-locking that will be discussed here are: saturable absorber mode-locking, Kerr lens mode-locking and nonlinear mirror mode-locking.

Saturable absorber

In general, a saturable absorber with much longer recovery time than the cavity round trip time would lead to Q-switching. Mode-locking can be generated by a saturable absorber with a recovery time shorter than the duration of mode-locking pulses, typically in the range of a few picoseconds or shorter. Liquid dye was initially used as saturable absorber. However, the mode-locking output from liquid dye can be unpredictable unless careful control of dye concentration, optical pumping and alignment is maintained, which limits the use of liquid dye saturable absorber [17]. Today, passive mode-locking is mainly based on semiconductor saturable absorber modelocking (SESAM). The technology of semiconductor saturable absorber allow accurate controlling of the parameter such as absorption wavelength, saturation energy and recovery time, which adaptable to various types of lasers [58]. Moreover, SESAM setup is very simple.

Passive mode-locking is usually self-starting from a random fluctuation in the cavity. Light pulses with low intensity will be attenuated by the saturable absorber more than light pulses with high intensity. Therefore, after a certain time, only one light pulse will survive in the cavity. Figure 1.17 shows a physical picture of the pulse shortening process of fast saturable absorber mode-locking. As the pulse arrives at the absorber, the absorber saturates. The loss from the absorber reduces creating a window of new gain between t_1 and t_2 . The leading and trailing edge of the pulse, however, experience losses. This process leads to the pulse shortening mechanism. Note that the gain is assumed to be constant (or “saturated gain”) during the passage of the pulse, which is a valid assumption for most of the solid state lasers in which the upper state lifetime is several magnitudes longer than the cavity round trip time.

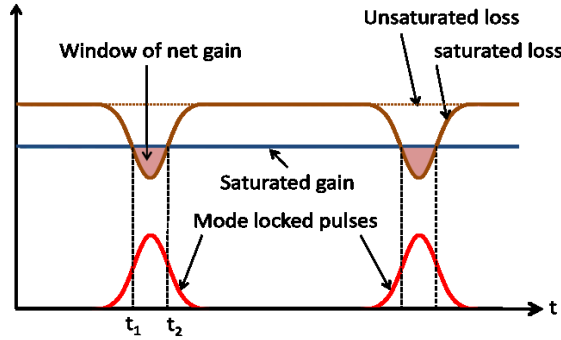


Figure 1.17: a physical picture of fast saturable mode-locking.

A saturable absorber with a recovery time shorter than mode locked pulses is known as a “fast saturable absorber”. A saturable absorber with a recovery time longer than mode-locking pulse duration is known as a “slow saturable absorber”. The mechanism of slow saturable absorbers is much more complicated than fast saturable absorbers. Mechanism of both fast saturable absorber and slow saturable absorber were fully explained in detail by Haus [59], [60]. However, as most solid-state lasers have a long upper state lifetime, the mechanism of slow saturable absorber mode-locking will not be presented.

Kerr lens mode-locking

Kerr lens mode-locking (KLM) is based on an intensity dependent change of refractive index in an optical material. In general, to first approximation, the refractive index of an optical material when intense light propagates through it can be written as,

$$n = n_0 + n_2 I \quad \text{Eq.1.10}$$

where n_2 is the nonlinear index and I is the intensity. The value of n_2 is a natural characteristic of a material, it is $\sim 4.5 \times 10^{-16} \text{ cm}^2/\text{W}$ for fused quartz. This change of the refractive index is known as the “Kerr effect”. When a pulse with a Gaussian

beam profile, $I = I_p \exp\left(\frac{-2r^2}{w^2}\right)$, travels through an optical material, to first order approximation, the refractive index variation is a parabolic function. The optical material then acts like a spherical lens with a focal length (f), which can be calculated [17],

$$f = \frac{w^2}{4n_2 I_p L} \quad \text{Eq. 1.12}$$

where L is the optical material length. The light passing through this material is then “self – focusing” with higher intensity light being focused more than lower intensity, as shown in Figure 1.18. By introducing an aperture to the cavity, light with higher intensity focuses more and thus experiences lower loss. This creates intensity dependent losses, which leads to the generation of mode-locking in a similar way to the fast saturable absorber. The advantage of KLM is that the response time of the Kerr effect is very fast (\sim femtoseconds) allowing the generation of ultrafast laser with a pulse duration close to bandwidth-limited.

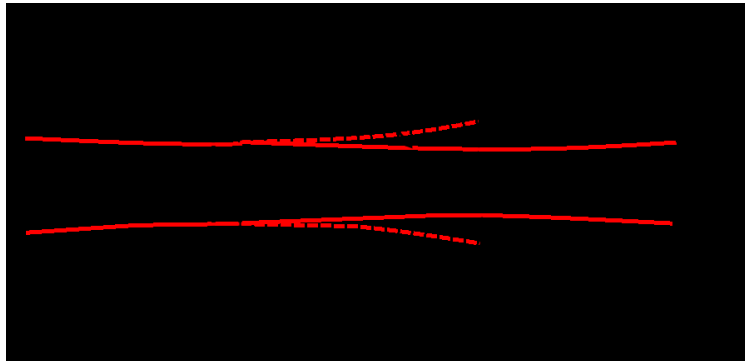


Figure 1.18: A demonstration of optical Kerr effect [18].

Nonlinear mirror mode-locking

Nonlinear mirror mode-locking is based on a nonlinear mirror (NLM) with an intensity dependent reflection. The concept is illustrated in Figure 1.19. A nonlinear mirror comprises a nonlinear crystal with $\chi^{(2)}$ susceptibility and a dichroic output coupler (DOC). The DOC has low reflection ($R < 100\%$) at the lasing wavelength and high reflection ($R \sim 100\%$) at the second harmonic (SH). When light passes through the nonlinear crystal, part of the light is converted to the SH. Light converted to SH is totally reflected by the DOC and under the right condition, is converted back to the fundamental after a second pass through the nonlinear crystal. The unconverted fundamental wavelength, however, loses some of its power as laser output. Therefore, the NLM has a nonlinear reflectivity depending upon the conversion efficiency to the SH, which is proportional to the light intensity. This also leads to the generation of mode-locking in the same way as the fast saturable

absorber. The mechanism of NLM mode-locking is discussed in more detail in section 2.4.

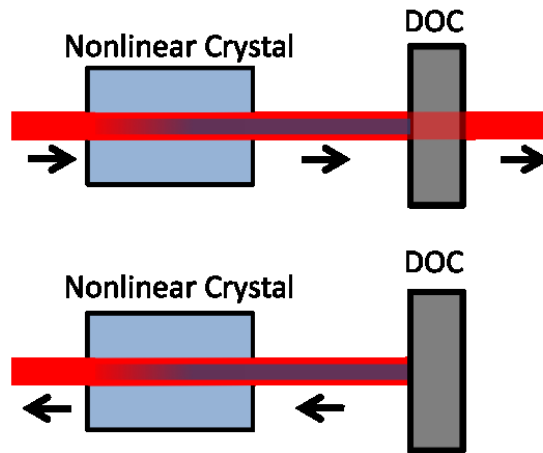


Figure 1.19: Conceptual diagram of NLM mode-locking technique. The upper picture shows part of the beam is converted to SH. In the case of correct phase difference, in the return part, as shown in the lower picture, some of the SH is converted back to the fundamental wavelength. The DOC has $R=80\%$ @1342nm and $R=100\%$ @671nm.

1.8 Gain Switching

Gain switching is commonly used in gain media with very short upper state lifetime such as semiconductor diode lasers. To gain-switch a diode laser the current is pulsed by the electrical circuitry. Even though the electrically pulsed diode laser cannot produce as short a pulse duration as mode-locking techniques or the peak power of Q-switching technique there are some advantages worth considering. Most significant is the flexibility of controlling the pulse repetition rate and pulse duration independently. As the technology has advanced, single emitter laser diodes at center wavelengths from 400– 2000nm have become available commercially. As well as the laser diodes, inexpensive commercial diode drivers which can produce nanosecond pulses with repetition rates in the range of MHz, are also commercially available.

1.9 Thesis Outline

Chapter 2 provides general knowledge and experimental demonstrations of the bounce geometry configuration. Firstly, the concept of bounce geometry including cooling systems and thermal effects will be described. Some important gain media Nd:YAG, Nd:YVO₄ and Nd:GdVO₄ will be compared. The second part of the chapter is a series of experimental demonstrations. The experiment throughout this chapter is based on Nd:YVO₄ operating at the 1342nm transition. In CW operation, laser performance in symmetric and asymmetric cavities will be presented; along with a discussion on output beam quality and cavity stability obtained from these configurations. For pulsed operation, Q-switching operation based on an acousto-optic modulator is presented. The final part of the chapter provides a general overview and demonstration of nonlinear mirror (NLM) mode-locking. NLM in combination with a bounce geometry configuration allows the generation of a high power mode locked laser as an alternative method to SESAM, particularly for 1342nm due to the high cost of fabrication of a suitable saturable absorber.

Chapter 3 introduces a versatile pulsed laser source at 1064nm based on a gain switched diode laser. A laser diode is driven by an electrical driving circuit, which allows control of the pulse duration (from 3.5ns to over 10μs) and pulse repetition rate (from single shot to 2MHz) independently. Firstly, the seed diode system is described in detail. The output from a diode laser is amplified by a two stage bounce geometry amplifier based on the MOPA configuration to provide useful pulsed energy as would be appropriate for industrial applications. The key results of the bounce amplifier are described, including the output power and gain obtained from different bounce angles. Other issues associate with laser amplifiers such as ASE, temporal and spatial characteristics are also discussed.

Chapter 4 provides an introduction and background knowledge of the Alexandrite laser, which is the main laser in the rest of the thesis. The crystal properties of Alexandrite compared to other tunable lasers are presented. The energy level scheme of Alexandrite in both 3-level laser and 4-level laser is explained. Other important parameters i.e. emission cross-section, fluorescence lifetime and excited state absorption of Alexandrite will also be presented. Alexandrite results from the

literature are summarised, pointing out some advantages of diode pumping compared to lamp pumping such as efficiency and compactness. This includes thermal lensing arising from diode end pumping a rod, which is the main geometry used in the experiment in chapters 5 and 6. Finally, some potential applications of Alexandrite lasers are presented.

In chapter 5, a demonstration of Alexandrite laser operation with pumping by high power diode laser is presented. Firstly, the laser diode optical and spatial characteristics are presented, followed by the optical delivery system. A simple compact cavity is demonstrated providing $> 26\text{W}$ output power, which is more than an order of magnitude higher than previously reported from diode pumped Alexandrite lasers. A slope efficiency of $\sim 49\%$ has been achieved, providing the highest slope efficiency diode pumped Alexandrite reported. Many other extended cavity configurations, which operate in both the positive and negative g-parameter regions of cavity stability, are also investigated. The design is developed further from single end pumping to double end pumping in order to reduce thermal load at the end of the Alexandrite crystal. In this chapter, the wavelength tunability of alexandrite is demonstrated using a self-seeding method. Finally, the performance of end-pumping is compared with side pumping in bounce geometry which was conducted by colleagues in the same group.

Chapter 6 is the final chapter of experimental work. The work in this chapter develops the diode pump Alexandrite laser towards remote sensing applications. Firstly, a beam shaping technique is used to improve the beam quality of the laser diode, which is used throughout the chapter. The characteristics of Alexandrite (CW, Quasi-CW and pulsed operation) as a function of temperature are studied. Alexandrite laser performance in Q-switching operation is studied based on an EO modulator. Some important parameters for Remote sensing applications such as pulse energy, efficiency and pulse duration as a function of temperature are investigated. A Q-switched pulse energy of over 1mJ at 100Hz was achieved from a compact cavity. Various cavity configurations are designed in order to improve beam quality and stability of Q-switched pulses. The final part is a demonstration of the frequency doubling of Alexandrite to the blue/UV region. Note that the

frequency doubling experiment is carried out in collaboration with other colleagues in the group.

Chapter 7 summarises the key results of the work in each chapter. The results are reviewed and discussed to compare in a broader context and finally provides some suggestions of directions for further development.

2 Bounce Geometry Laser

2.1 Introduction

In this chapter, bounce geometry laser designs are discussed and some results by the author from CW, Q-switching and mode-locking bounce lasers are presented.

The first part of the chapter focuses on general background about bounce geometry configuration. The importance of bounce angle and suitable gain mediums for the bounce geometry configuration are described in detail. Thermal lensing effect on spatial laser operation in bounce geometry will be discussed.

The second part of the chapter is a demonstration of a bounce geometry configuration. The gain medium used in this chapter is 1.1 at.% doping Nd:YVO₄ crystal and the system is optimised for a laser wavelength of 1342nm. In this section, the cavity was first set up in a simple compact symmetric cavity, where CW high-power (~15.9W) multimode lasing was achieved. After that, the cavity was adapted to obtain single mode output. The M-squared of 1.13 and 1.47 in a vertical and horizontal are obtained with minimal optimisation. The latter part of the section is a demonstration of Q-switching operation. The Q-switching technique is based on an acousto-optic modulator where average power of ~10W with high repetition rate (40 - 460kHz) could be achieved

The final part of this chapter is a demonstration of the nonlinear mirror (NLM) mode-locking technique incorporated with the bounce geometry configuration. As discussed in chapter 1, NLM mode-locking is a passive mode-locking technique and is based on intensity dependent reflection of a NLM. In this section, the arm length of the bounce geometry laser was significantly extended in order to increase the

cavity round trip time for mode-locking operation. An average output power of 9.1W at a pulse repetition rate of 113MHz was achieved from 51W pump power. A main pulse duration of 13.8ps was achieved.

2.2 Bounce Geometry

The bounce geometry, first proposed by Bernard and Alcock in 1993 [48] is based on total internal reflection (TIR) of the laser mode at the pump face of a gain medium. Like the ‘zig-zag’ slab design, the bounce geometry distributes the pump radiation over the large area of the pump face so the thermal effect can be better managed in the end-pumped rod system.

In bounce geometry, a laser mode has a grazing angle of incidence TIR at the pump face of a gain medium. By using a gain medium with high absorption at the pump wavelength, most of the energy of the pump is localized near the pump face. This ensures the laser mode experiences high inversion. The bounce geometry has the advantage over the ‘zig-zag’ as the laser mode has higher spatial matching with the highest pump density near the pump face of the crystal throughout the beam passage. This gives rise to high efficiency along with good beam quality. The first bounce geometry demonstration obtained a slope efficiency as high as 44% with laser mode near single transverse electromagnetic mode (TEM_{00}) in a quasi-CW operation [48]. The same group also achieved Q-switch operation of almost 1mJ at 1kHz repetition rate [61]. The first CW operation based on bounce geometry and obtaining a slope efficiency as high as 72% was shown by Damzen et. al. in 2001 [62]. The average output power was 22.5W, which is over a magnitude higher than previous bounce geometry work [62]. Since then, bounce geometry configuration has been employed in many high power laser in both CW and pulse operation including Q-switching and mode-locking [14]. In terms of power scaling, compared to end pumping, bounce geometries offer reduced thermal lensing and simplicity in optical pump delivery from high power diode array. Power scaling to >100W in a TEM_{00} mode based on a bounce geometry amplifier in a MOPA configuration also has been demonstrated [50].

2.2.1 Bounce Geometry Concept

For the simplest bounce geometry, the laser mode has a single total internal reflection (TIR) or bounce with a small angle at the pump face of the gain medium. The bounce geometry configuration is illustrated in Figure 2.1. In general, the bounce angle (θ_{bounce}) is defined as the angle between the laser mode and the front face of the crystal. The pump beam, shown in the orange colour, is focused by the vertical cylindrical lens (VCL_D) to the pump face of the crystal. This creates a thin line of high inversion at the pump face, the size of which is generally approximately $10\text{mm} \times 100\mu\text{m}$. The vertical length (y-direction) depends upon the focal length of the vertical cylindrical lens (VCL_D) while the horizontal length (x-direction) depends upon the distance between the laser diode and the gain medium. By using a gain medium with high absorption at the pump beam wavelength, a high inversion density will be created in a shallow region of the pump face of the gain medium.

Bounce geometry also benefits from averaging the nonuniform gain profile [16]. As the maximum pump intensity is at the pump face and decreases exponentially as penetrating through the crystal, the part of laser-mode which is closer to the front face experiences higher gain. The TIR at the pump face, however, reverses the position of the laser mode relative to the front face of the crystal. Therefore, the laser mode experiences a similar amount of gain across its whole cross-section. In general, the crystal ends are cut at some angle in order to avoid parasitic self-lasing which could occur with a medium, which has very high gain.

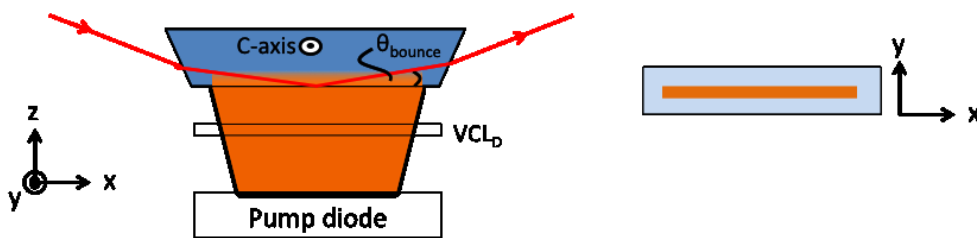


Figure 2.1: Schematic of bounce geometry.

2.2.2 Laser Gain Media

The laser gain medium is one of the most important parts of a laser oscillator. In addition to many of the desirable properties of a laser gain medium (such as high emission cross-section, high fracture limit and high thermal conductivity), in bounce geometry high absorption at the pump wavelength is necessary for optimum performance. High absorption ensures that the most of the energy of the pump is localized near the pump face of the crystal. For a low absorption gain medium, the absorption length is longer and thus, requires a larger bounce angle for sufficient overlap between the laser mode and the gain region.

Among all gain media, Nd^{3+} is one of the most popular rare earth ions used. The energy level diagram of Nd^{3+} is shown in Figure 2.2. Nd^{3+} crystals have a highest absorption band at around 808nm, which can be pumped from commercially available diode laser. Another interesting pump transition is around 880nm, which is a directly excited ion to the upper laser level. This will reduce the quantum defect and reduce thermal loading [63], [64] although the absorption coefficient and bandwidth are smaller than for the 808nm transition. The peak emission wavelengths obtained from Nd^{3+} are around 0.9, 1.1 and 1.3 μs and depending on the host crystal (see table 2.1). The relative emission strength of Nd^{3+} is determined by the radiation rate between an upper state level and a lower state level, which has highest rate between the ${}^4\text{F}_{3/2}$ and ${}^4\text{I}_{11/2}$ levels. This leads to the highest stimulated emission cross-section of $\sim 1.1\mu\text{s}$. The Nd^{3+} gain mediums such as Nd:YAG, Nd:YVO₄ and Nd:GdVO₄ have been demonstrated to work efficiently at around 1064nm in a bounce geometry configuration [62][65][50]. Table 2.1 shows a comparison of the popular Nd^{3+} gain mediums used in bounce geometry.

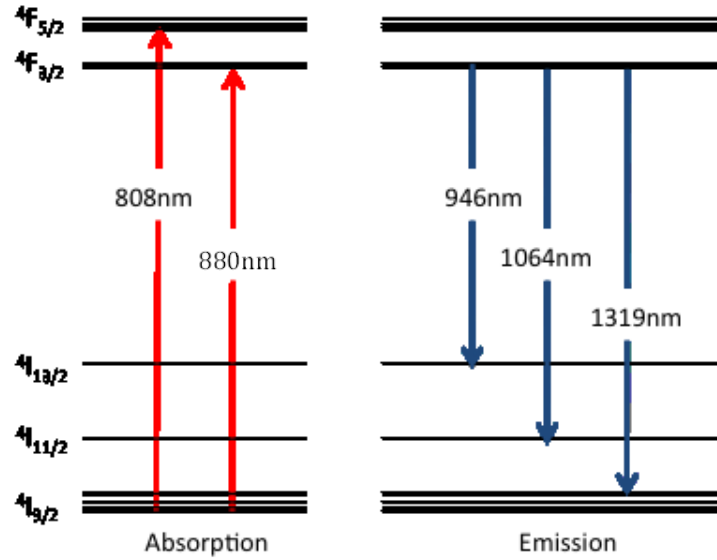


Figure 2.2: Partial energy level diagram for Nd:YAG crystal.

Nd:YAG crystal is one of the most commonly used laser gain media. It has many desirable characteristics such as hardness, high thermal conductivity and low thermo-optic coefficient. In addition, Nd:YAG has the advantage of relatively a long upper state lifetime of $230\mu\text{s}$ [42], which makes it suitable for generating high pulse energies by Q-switching. However, because Nd:YAG has a comparatively low absorption coefficient, high doping concentrations are required for sufficiently strong absorption when used in a bounce geometry configuration. Using a 2 at. % doped Nd:YAG, output powers as high as 46W at a laser wavelength of 1064nm and a slope efficiency of 60% has been demonstrated with a bounce geometry configuration [65].

Another popular gain medium used in bounce geometry is Nd:YVO₄. This medium has a very high pump absorption which is ~ 4 times higher than Nd:YAG. Also it has a high stimulated emission cross section that is ~ 3 and ~ 7 times higher than Nd:YAG at 1064nm and $\sim 1.3\mu\text{m}$ respectively. In addition, due to the nature of its birefringent structure, Nd:YVO₄ emission cross-section is polarization dependent which can reduce laser efficiency loss due to thermally induced depolarization. The slope efficiency of 72%, which is the highest reported from bounce geometry at 1064nm has been demonstrated using this crystal [62]. At 1342nm the slope efficiency of 38% has been achieved [66], this is comparatively lower due to larger quantum defect and significantly higher ESA [37][67]. The drawback of Nd:YVO₄

is a comparatively large thermal lensing, due to its lower thermal conductivity, which must be compensated for in the laser. Another gain medium is Nd:GdVO₄, which has fairly similar properties and comparable performance to Nd:YVO₄ [26], [68]. However, due to the benefits of larger stimulated emission cross section and the better availability of the crystal, all the bounce geometry work in this thesis is based on Nd:YVO₄.

Symbol definition		Nd:YAG	Nd:YVO ₄	Nd:GdVO ₄
Absorption coefficient at 808nm [cm ⁻¹]	α	8	40	78
Fluorescence lifetime at 300K [μ s]	τ	230	90	90
Laser wavelength ⁴ F _{3/2} → ⁴ I _{9/2} [nm]	λ	946	914	912
Stimulated emission cross-section[10 ⁻¹⁹ cm ²]	σ	0.5	0.5 c	0.7 c
Laser wavelength ⁴ F _{3/2} → ⁴ I _{11/2} [nm]	λ	1064	1064	1064
Stimulated emission cross-section[10 ⁻¹⁹ cm ²]	σ	2.8	11.4 c	7.6 c
Laser wavelength ⁴ F _{3/2} → ⁴ I _{13/2} [nm]	λ	1319	1342	1342
Stimulated emission cross-section[10 ⁻¹⁹ cm ²]	σ	1.0 c	7.0 c	1.8 c
Thermal conductivity [Wm ⁻¹ K ⁻¹]	κ	14	3.0 c 8.6 ⊥c	4.7 c 6.9 ⊥c
Thermal expansion [10 ⁻⁶ K ⁻¹]	α	8.2 7.7	8.4 c 2.2 ⊥c	7.3 c 1.5 ⊥c
Thermo-optic coefficient [10 ⁻⁶ K ⁻¹]	dn/dT	7.3	3.0 c 8.6 ⊥c	4.7 c 6.9 ⊥c

Table 2.1: Comparison of optical, thermal and physical properties of Nd³⁺ crystals commonly used in bounce geometry laser configurations [35][18][17][50]. For Nd:YVO₄ and Nd:GdVO₄ which are birefringence crystals, some properties in parallel (||c) and perpendicular (⊥c) to the c-axis of the crystal.

2.2.3 Thermal Effect

The most significant heating in Nd:YVO₄ is due to heat energy generated caused by the quantum defect. When pumping at 808nm and lasing at 1064nm and 1342nm, respective quantum defects of 24% and 40% are achieved. As mentioned in Chapter 1, a common problem affecting laser performance is thermal lensing, leading to cavity instability, degradation in the output power and beam quality. Thermal lensing arises from the temperature dependent change of refractive index (dn/dT), stress induce changes of refractive index and distortion of the flatness of the crystal faces (end-effect) [42][17]. However, stress induce changes of refractive index

occurs in the Nd:YVO₄ in a bounce geometry configuration is relatively small and can be neglected [69].

In bounce geometry generally, a crystal is conduction cooled by contacting with a copper heat sink, as shown in Figure 2.3. The copper heat sink, which has a temperature-controlled constant flow of water, is connected to the top and the bottom of the crystal. The effect of thermal lensing on a laser mode in this geometry can be decomposed into the horizontal direction, the plane orthogonal to the front face, and the vertical direction, the plane parallel to the front face. The small vertical pump dimensions and the direction of the heat transfer results in high temperature gradients and end deformation effect. This results in thermal lensing in the vertical direction approximately 20 times higher than the horizontal direction [70]. Therefore, thermal lensing in bounce geometry is highly astigmatic.

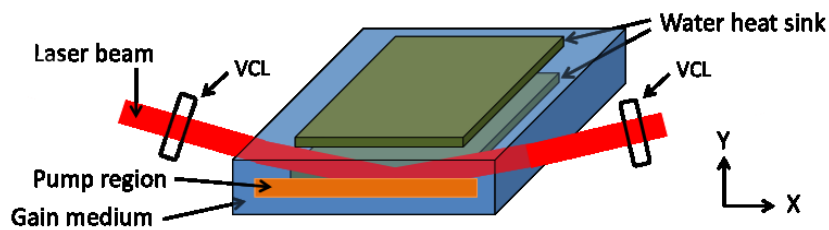


Figure 2.3: Schematic diagram of bounce geometry in a slab gain medium where the orange area shows the pump region. The gain medium is a slab with face cooled from top and bottom of the plate.

To compensate the strong thermal lensing in the vertical direction, two (intracavity) vertical cylindrical lenses (VCLs) are usually placed to focus the laser mode to match the small pump size in the gain medium, as shown in Figure 2.4. The two VCLs are placed at a distance from the center of the rod that is roughly equal to the focal length of the VCLs. As the laser mode passes through the center of the gain medium, the thermal lensing in the vertical direction diminishes due lower diffraction of the laser mode.

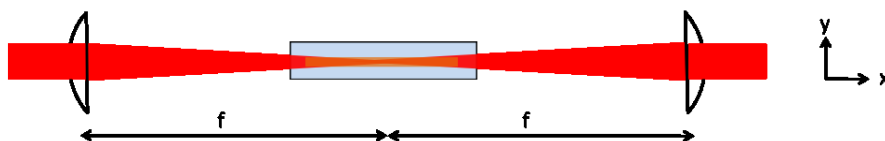


Figure 2.4: Laser mode size in the vertical direction. When thermal lensing is present the rod acts like a lens-like gain medium.

A thermal gradient in the horizontal direction arises because of the exponential absorption from the pump face of the gain medium. The effect of thermal lensing in the horizontal direction can be visualized by considering the beam passing through the mirror-like gain medium, as shown in Figure 2.5 for (a) end-deformation effect and (b) temperature gradient effect [71]. Even though the thermal lens is much smaller compared to the vertical direction, the laser mode size in the horizontal direction is much larger. Therefore, in bounce geometry, the thermal lensing in the horizontal direction usually has a larger effect on the performance of the laser mode [62][66].

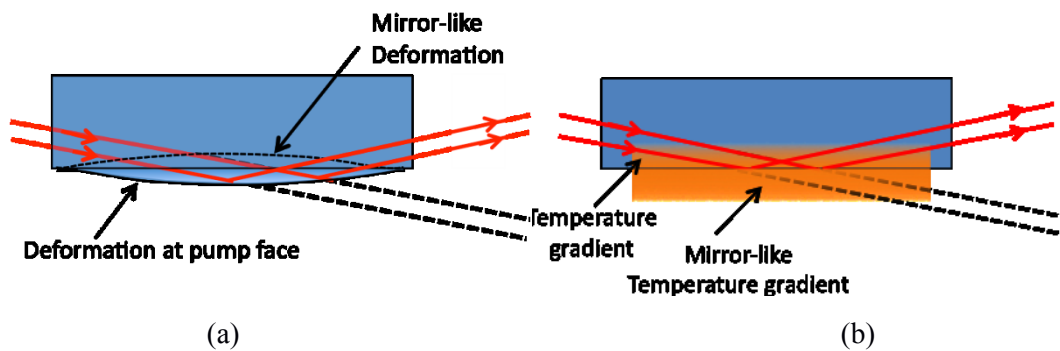


Figure 2.5: Thermal lens in a horizontal direction occurs from (a) end-effect deformation. The blue region represents expansion and mirror-like expansion occurs from deformation at the pump face. (b) Temperature gradient changes of refractive index. The orange are represent exponential absorption of the pump beam. Note that dimensions and angles are highly exaggerated.

2.3 Bounce Geometry Nd:YVO₄ Demonstration of 1342nm Transition

This section describes a series of laser demonstration based on bounce geometry configuration at a transition of 1342nm. This wavelength is of great interest for material processing applications, spectroscopy and scientific research. It can also be used as a source to generate a high power laser with good beam quality at 671nm through frequency doubling. This section starts with a demonstration in CW operation in a compact cavity for high power and high efficiency operation. The

cavity is later extended to achieve single mode output laser. Note that the results of CW Nd:YVO₄ operation is a continuation of the authors previous work for Master's research. The results will be reproduced and presented here as background for better understanding the bounce geometry configuration. The final part of this section is a demonstration of Q-switching operation based on AO modulator.

2.3.1 CW Multimode Operation

In the bounce geometry, high power output and high efficiency can be obtained from a compact-symmetric cavity. The cavity configuration is shown in Figure 2.6. The gain medium was a 1.1 at. % doped Nd:YVO₄ crystal. The gain medium was side-pumped by an 808nm laser diode bar, which results in an absorption depth of ~240μm. The polarization of the laser diode was arranged to have the same direction as the C-axis of the crystal in order to obtain highest absorption. The laser diode was focused onto the crystal by VCL_D with a focal length of 25mm.

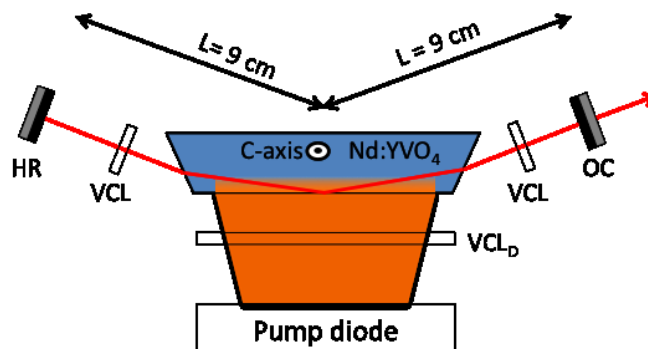


Figure 2.6: Schematic diagram for a compact-symmetric cavity.

To optimize the system, the distance between VCL_D and the crystal could be adjusted to alter the size of the diode laser in the crystal in a vertical direction, and also the distance between the laser diode and the crystal to alter the size in the horizontal direction. The pump faces of the crystal were anti-reflection coated (AR-coated) at 808nm, while the end faces were AR-coated at the lasing wavelength of 1342nm. The high reflection mirror (HR) was coated for high reflectivity at 1342nm and has lower reflectivity at 1064nm in order to suppress laser lasing at 1064nm. The output coupler (OC) had 80% reflectivity at 1342nm. Two VCLs with focal length 50mm were placed to match the laser mode with the high

gain region in the vertical direction and AR-coated at 1342nm. Both arm lengths used in this compact-symmetric cavity were set at 9cm.

The highest output power was obtained from an 8° bounce angle. Figure 2.7 shows the output power as pump power varies. The maximum power of 15.9W was achieved from 53W incident pump power, which corresponds to an optical-to-optical conversion efficiency of 30%. The result shows that the output power increases linearly with the pump power with little indication of roll over. The spatial profile at full pump power is shown on the right hand side of the figure. The beam profile was a single mode in the vertical direction, but multimode in the horizontal direction. In the vertical direction, the laser mode size is very small and matches the fundamental mode well with the gain region. In the horizontal direction, in contrast, the gain region is much larger in size allowing the laser to operate at higher order modes.

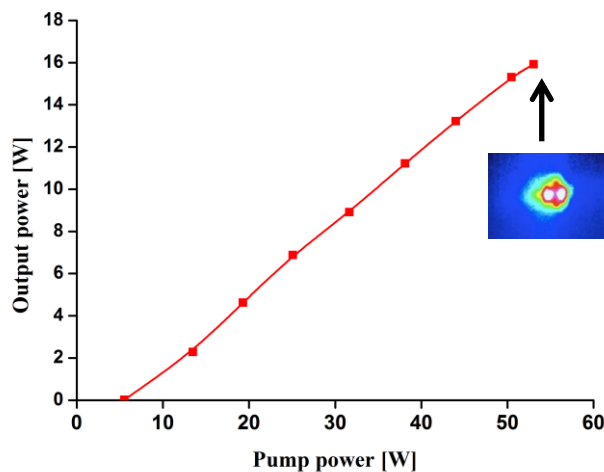


Figure 2.7: Output power as a function of pump power for compact-symmetric cavity

2.3.2 CW Single Mode Operation

Single mode operation can be obtained using an asymmetric cavity. The asymmetric cavity controls the laser mode size to match the fundamental laser mode with the highest gain region in the crystal. This cavity design exploits the thermal lensing and cavity stability to suppress higher order modes from lasing, allowing single mode operation at high pump power. The experimental setup is shown Figure 2.8.

The experiment was conducted by adjusting the two arm lengths of the compact symmetric cavity. The HR mirror and the output coupler arm were extended to 12 cm and 25 cm respectively. Note that the cavity was optimised for highest power in the fundamental mode at full pump power.

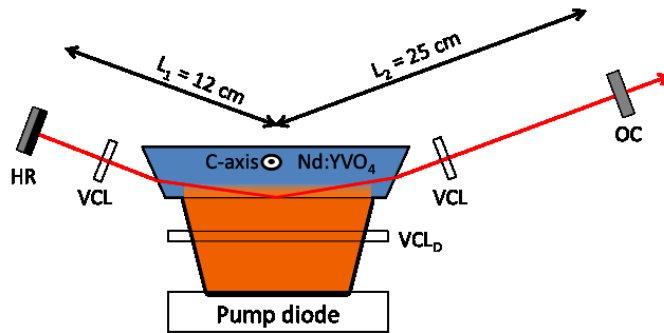


Figure 2.8: Schematic diagram for a symmetric cavity.

Figure 2.9 shows the output power versus the pump power. The output power of 10.5W was obtained from 53W pump power. This corresponds to an optical-to-optical conversion efficiency of 20%. The power curve also shows that the output power initially increases with the pump power. The cavity become unstable, where the power drops significantly, at pumping level from ~30W and became stable again at over 50W pump power. The single mode laser output was achieved at full pump power, as shown in Figure 2.9. However, the M-squared was measured to be 1.13 and 1.47 in the horizontal and vertical respectively, which indicates that the output was good but not perfect TEM₀₀.

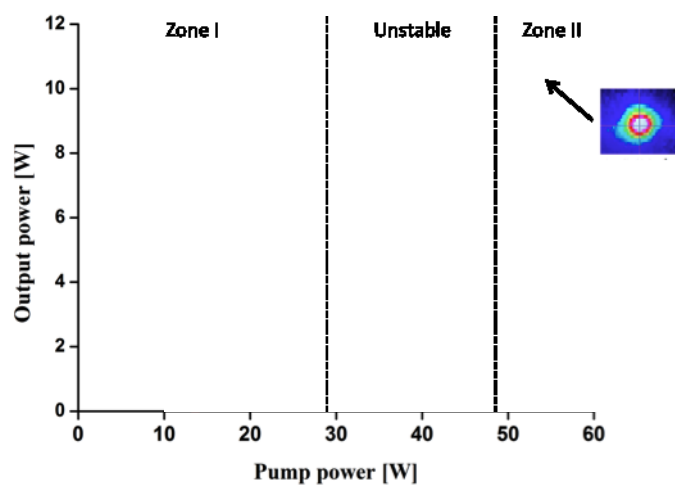


Figure 2.9: Output power as a function of pump power for asymmetric cavity.

The two separated stability zones is common behaviour for an asymmetric cavity with intracavity lens, which can be explained using a stability diagram in terms of g parameters, as shown in Figure 2.10. For a symmetric cavity, as the thermal lensing increases, the cavity moves from point 1, along the solid line. The symmetric cavity therefore has one stable zone. For an asymmetric cavity, as the pump power is increased, so does the thermal lensing and the cavity stability moves from point 1 along the dotted line. Therefore, the cavity is initially stable in zone 1, however, between points 2 and 3, the cavity becomes unstable. The instability of the cavity results in a significant drop in the output power and a degradation of the beam quality. As the thermal lensing increases, the cavity enters zone II of the stable region. The output power and the beam quality are then recovered.

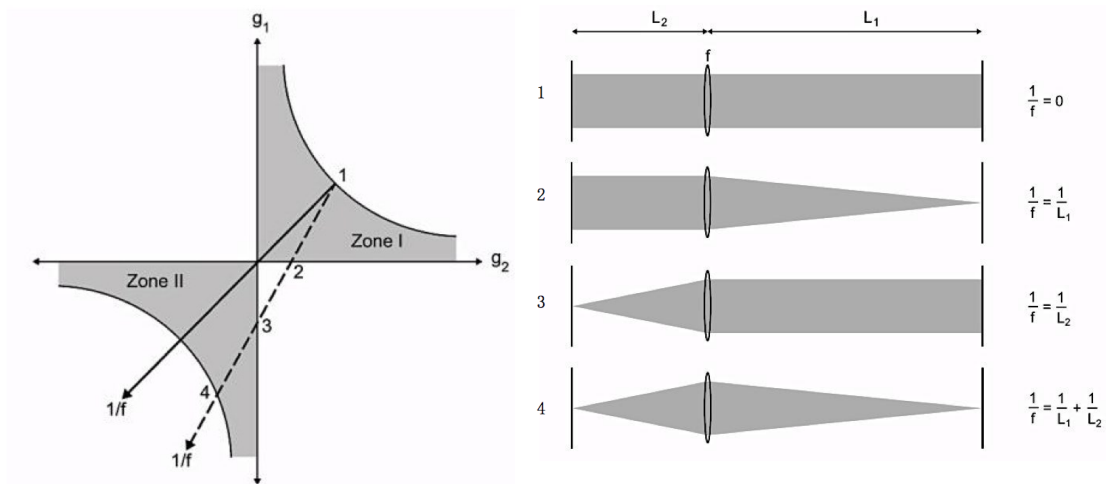


Figure 2.10: (a) Stability diagram of parallel-plane cavity represented by g-parameter. The cavity moves along a dotted line for an asymmetric cavity [55]. (b) Laser mode behaviour for an asymmetric cavity at four critical points in the stability diagram for plain-plain mirror [55].

2.3.3 Q-switching Operation

A schematic diagram of the Q-switching experimental set up is shown in Figure 2.11. An acousto-optic modulator was inserted between the VCL and the OC (R= 80% reflectivity), the arm lengths were unchanged from the asymmetric cavity described above. The gain media was CW pumping with 808nm diode. For each

period, the time of the AO modulator driving voltage switched off, or the cavity was “opened”, was fixed at two microseconds.

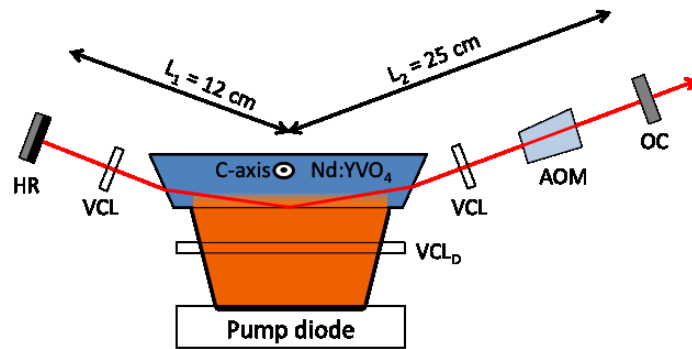


Figure 2.11: Experimental set-up for Q-switching in an asymmetric cavity.

Figure 2.12 shows the average output power and pulse duration full width half maximum (FWHM) as a function of the repetition rate using 53W pump power. Clean Q-switched TEM₀₀ pulses with an average output power of around 10W was achieved with pulse repetition rates from 40 – 460kHz. At a repetition rate below 40kHz some of the energy was released as a small pulses, or pre-pulses, before the giant pulse. For pulse repetition rates of 460kHz and above, pulse skipping was observed. The results also show pulse duration increases almost linearly, from 24 - 94ns, with repetition rate. This is due to lower energy being stored in the gain medium at higher repetition rates, thus, the pulse requires longer time to build up to exceed threshold.

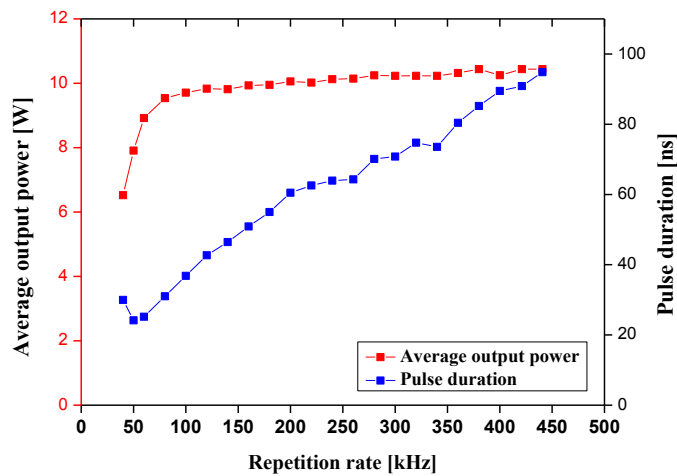


Figure 2.12: Average output power and pulse duration as a function of repetition rate.

Figure 2.13 shows pulse energy and peak power as a function of repetition rate. The pulse energy was calculated by dividing the average output power by the repetition rate. Peak power was estimated by dividing the pulse energy by the pulse width. The maximum pulse energy of $162\mu\text{J}$, corresponding to a peak power of 5.5kW , was achieved at 40kHz . The pulse energy reduces with repetition rate to $23\mu\text{J}$, corresponding to a peak power of 1.25 kW , at 460kHz . The reduction of both pulse energy and peak power resulted from shorter build up time, and thus less energy, stored in the gain medium.

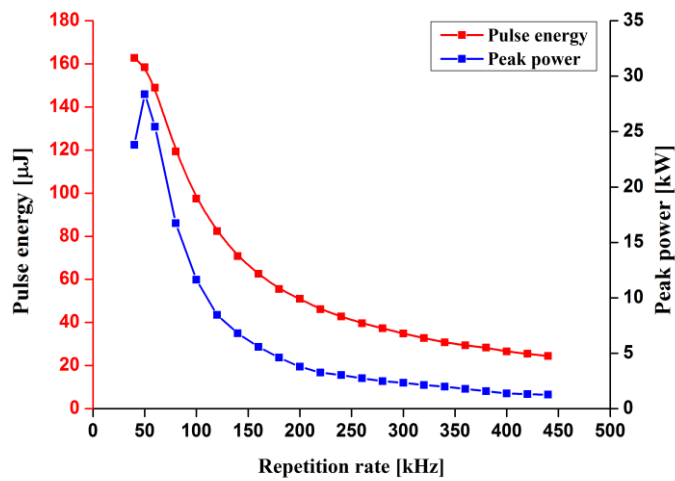


Figure 2.13: Pulse energy and peak power as a function of repetition rate.

The difficulties of achieving clean Q-switched pulses at low repetition rate has been observed in many active Q-switching lasers, especially for a high gain mediums. The inefficient hold-off of the laser at low repetition rate indicated that, at some point when the cavity still “closed”, the accumulated round trip gain is high enough to exceed the total round trip losses (or threshold level) introduced by the loss modulator and the output coupler. One way to suppress pre-pulsing is based on using a secondary cavity to clamp the gain of the laser to below the limit of the hold off level. This pulse-control technique, which has been implemented within the group, has allowed a cavity to obtain clean Q-switched pulses at much lower repetition rate [72]. However, no further experiment was developed in this study. The maximum Q-switch repetition rate, however, is limited by the time the cavity requires to build up the gain after each giant pulse in order to exceed the lasing threshold. When the pulse build up gain does not reach the lasing threshold at the

time the cavity is “open”, pulse skipping will occur. Therefore, to achieve high repetition rate, a high gain material is required.

2.4 Nonlinear Mirror Mode-locking

As mentioned in chapter 1, the most common passive mode-locking method is based on a semiconductor saturable absorber mirror (SESAM) where the light intensity dependent loss mechanism is created from a saturable absorber. However, the output power is usually limited by heating damage of the SESAM [73]. It was noted that scaling approaches for SESAM mode-locking have been proposed and implemented with high average powers [74]. However,, a saturable absorber is designed for a specific wavelength. A semiconductor, GaInNAs, has been developed for 1342nm but has high costs due to difficulties in fabrication [75]. Nonlinear mirror (NLM) mode-locking was first proposed by Stavkov in 1988 [76]. NLM is an alternative passive mode-locking technique based on a nonlinear mirror with an intensity dependent reflection. The NLM mode-locking technique is an interesting alternative method for the generation of a high power mode locked laser, mainly as the process does not rely on absorption, thus, heating damage from absorption can be avoided. Besides, NLM is based on the nonlinear effect, which is instantaneous so the pulse duration is not limited by recovery time. Theoretically, bandwidth-limited pulse duration can be achieved from NLM technique. A high-power mode locked laser using the NLM technique in a bounce geometry operating at 1064nm has been demonstrated. An 11.3W average output power with a pulse duration of 57ps has been achieved from Nd:GdVO₄ crystal [77]. NLM mode-locking is, in fact, particularly interesting for 1342nm due to difficulties in the fabrication of an appropriate saturable absorber at this wavelength [78]. A number of studies of NLM mode-locking at 1342nm have been reported using different nonlinear crystals[79]–[81].

In this chapter, a BIBO was used as a nonlinear crystal. This crystal has been previously demonstrated to provide an average output of 1W with pulse duration less than 7ps from Nd:YVO₄ and Nd:YLF, which is very close to the theoretical

value of a bandwidth-limited pulse [79]. However, the average power of most of the work involving mode locked lasers working at 1342nm was limited by the maximum power achieved in CW operation. In this chapter, by applying the nonlinear mirror technique with bounce geometry, a mode locked laser with short pulse duration and high average power could be achieved.

2.4.1 Nonlinear Mirror Mode-locking Technique

Nonlinear mirror mode-locking (NML) is a passive mode-locking technique which is based on the use of a nonlinear mirror with an intensity dependent reflection. The intensity dependence of the nonlinear mirror comes from the combination of the nonlinear crystal with $\chi^{(2)}$ susceptibility and the dichroic output coupler (DOC), similar to the combination of a saturable absorber and a mirror. The conceptual diagram is illustrated in Figure 2.14.

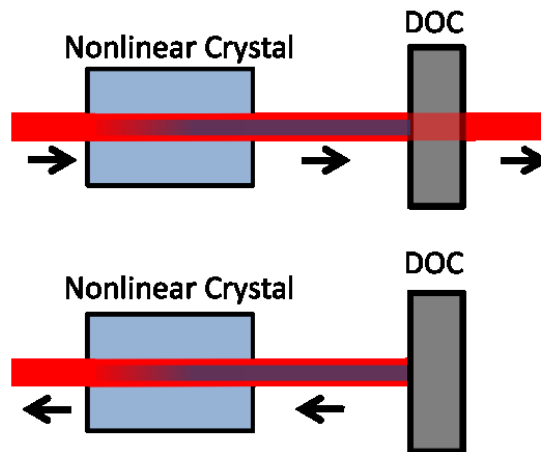


Figure 2.14: Conceptual diagram of NLM mode-locking technique. The upper picture shows part of the beam is converted to SH. In the case of correct phase difference, in a return part, as shown on the lower picture, some of the SH is converted back to fundamental. The DOC has $R=80\%$ @1342nm and $R=100\%$ @671nm.

The upper picture shows that the fundamental laser beam, shown in red, initially passes through the nonlinear crystal. The beam has correct phase matching for SHG and is partially frequency doubled. The fundamental and second harmonic wavelengths propagate to the DOC. The DOC partially reflects the fundamental wavelength (ω_1) and totally reflects the second harmonic wavelength (ω_2). In a return pass, if the phase difference at the right hand side of the nonlinear crystal was

$\Delta\phi = 2\phi_{\omega_1} - \phi_{\omega_2} = +\frac{\pi}{2}$, where ϕ_{ω_1} is the phase of the fundamental beam and ϕ_{ω_2} is the phase of the second harmonic beam, the SHG will continue growing as long as the phase matching condition is satisfied. On the other hand, if the phase difference ($\Delta\phi$) was, $\Delta\phi = 2\phi_{\omega_1} - \phi_{\omega_2} = -\frac{\pi}{2}$, some of the second harmonic is converted back to ω_1 by difference frequency generation (DFG). By carefully adjusting the distance between the nonlinear crystal and the dichroic output coupler, the required phase difference between the fundamental and second harmonic can be accomplished through dispersion in the air. The mathematical analysis is explained in detail by Stankov [76].

At the leading and trailing edge of the pulse, the intensity is low. The conversion efficiency to SHG is negligible, and thus, the NLM reflectivity is equal to the reflectivity of ω_1 . However, the intensity near the centre of the peak is high. The conversion efficiency to and from the SH increases significantly and thus, the reflectivity of the NLM increases. The nonlinearity of the reflection of the NLM according to light intensity is the basis of passive mode-locking, which finally leads to the pulse shortening process. Note that, the nonlinearity of the NLM according to light intensity, in general, depends upon the conversion efficiency to the SH and the reflectivity of ω_1 [76].

2.4.2 Extended Cavity for NLM Mode-locking Setup

The cavity used in NLM mode-locking was based on an asymmetric cavity to ensure a single mode laser output. As the total length of the asymmetric cavity was only 37cm, the cavity was extended in order to increase the cavity round trip time, and thus increase the stored energy for the mode locked pulses. The experimental setup for NLM mode-locking is shown in

Figure 2.15. In order to maintain laser properties such as beam quality and cavity stability, the cavity was extended using two positive spherical lenses to form a telescope (4f system). The nonlinear crystal (NLC) was introduced between the second lens and the dichroic output coupler (DOC). The two lenses have focal

lengths of 300mm (SPL_1) and 150mm (SPL_2), positioned 450mm apart in order to reduce the size of the intracavity waist near the NLC by a factor of two which increases the intensity, and so the conversion efficiency into SHG. The NLC was BIBO of dimensions 10x3x3mm and was placed in the oven which was temperature controlled at 40°C. To ensure that the phase difference between the fundamental and second harmonic was correct for DFG, the BIBO was placed on a translational stage so that the distance between the BIBO and DOC could be adjusted. The distance between the BIBO and the DOC required for the phase matching condition for DFG was about 37mm. The total cavity length of the extended cavity was ~140cm. The DOC had a reflectivity >99% at 671nm, and a reflectivity of 80% at 1342nm.

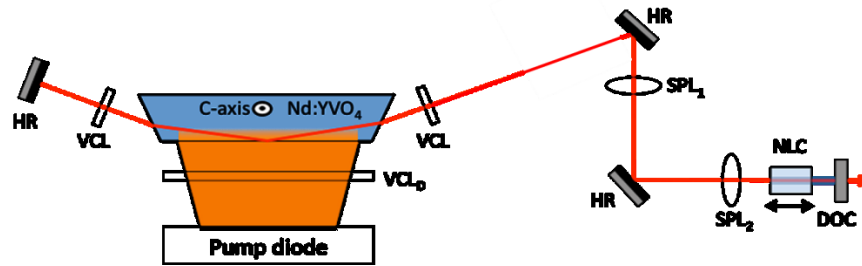


Figure 2.15: Experimental set-up for NLM mode-locking.

2.4.3 Experimental Results

The cavity alignment was very sensitive due to the small acceptance angle of the BIBO. However, when the cavity was well aligned, the mode-locking was spontaneous. Continuous mode-locking with an average output power of 9.1W was achieved from 53W pump power. This corresponds to an optical efficiency of 17%. Figure 2.16 shows the photodiode signal of a mode locked pulse train using a 10ns rise time photodiode. The signal shows a stable mode locked pulse train with repetition rate of 113MHz, corresponding to a cavity round trip time of 9ns.

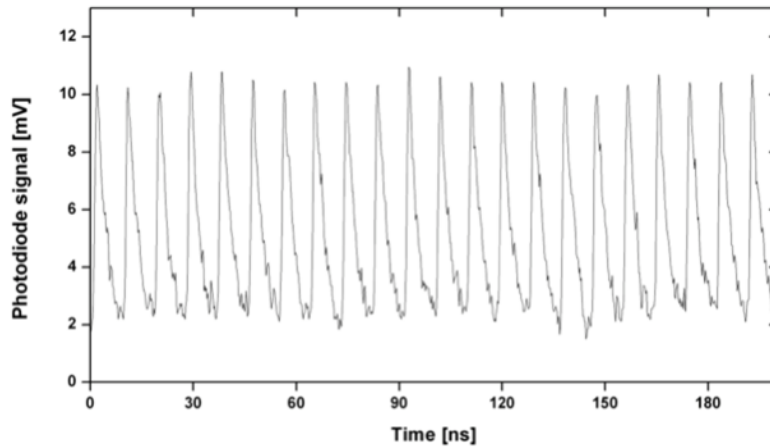


Figure 2.16: Mode locked pulse train

Figure 2.17 shows the autocorrelation trace of the mode locked pulse train using a home-built background-free intensity autocorrelator. The result shows that the main pulse is accompanied by many satellite pulses. The pulse duration (FWHM) of the “main” pulse, was 25ps, assuming a Sec-squared shaped pulse.

One of the main limitations for achieving bandwidth-limited pulse duration was the group velocity mismatch (GVM), i.e. the difference in group velocity between the fundamental frequency and the second harmonic frequency in the NLC. The group velocity mismatch in the NLC leads to temporal walk-off, which limits the effective length of the nonlinear frequency conversion, and thus limits the performance of the pulse shortening. The theory of the effect of the group velocity mismatch on the pulse shortening process is described in detail by Stankov [76].

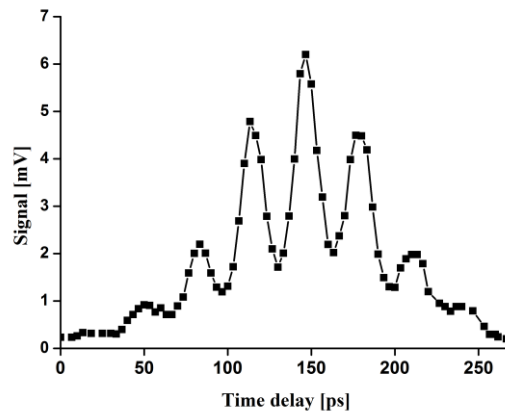


Figure 2.17: Autocorrelation trace

The satellite pulses shown in the autocorrelation trace indicate that the mode-locking of the pulses is incomplete and broken-up into two or more pulses. These satellite pulses sometimes occur in mode-locking, particularly in passive mode-locking as passive mode-locking relies on an initial noise spike to trigger the mode-locking mechanism [82]. Two or more of the initial noise spikes that are the same, or very close, in intensity may lead to the main pulse being accompanied by a satellite. However, as most of the gain is extracted by the main pulse, the satellite pulses usually contain comparatively less energy. However, it is possible that mode-locking performance such as shorter pulse duration and smaller satellite pulses could be improved with better alignment of the laser components. For instance, a bounce geometry configuration using NLM mode-locking was shown to generate a mode-locked pulse train at an average power of >7W and with a pulse duration of 5.7ps at 1064nm [77]. However, after four months, it was decided not to pursue this further but move to other core research for this PhD thesis.

2.5 Conclusion

This chapter introduced a bounce geometry configuration. Firstly, the concepts of bounce geometry and bounce angle were described. Suitable gain media for bounce geometry such as Nd³⁺ crystals were discussed and compared while, in this study, Nd:YVO₄ was used as a gain medium. Physical, optical and spectral properties of laser crystals were discussed in detail. Heat generation and thermal loading in the bounce geometry configuration were also presented.

The second part of the chapter was a demonstration of bounce geometry lasers at 1342nm. A symmetric compact cavity Nd:YVO₄ system lasing at 1342nm was presented. An output power of 15.9W in multimode operation was achieved with 30% optical-to-optical efficiency. The cavity was then adapted to an asymmetric cavity which utilised thermally induced lensing to match the fundamental laser mode with the gain medium. However, due to the asymmetry of the cavity, the cavity exhibits two separated stability zones. The first stability zone occurred at pump powers up to about 29W. At pump powers between 29W and 49W, the laser

moved to an unstable region which resulted in a decrease of output power and a degradation of the beam quality. When the pump power was increased, the thermal lensing became stronger and the laser could operate in the second stability zone. The beam spatial quality was high but the laser mode was not pure TEM₀₀, as indicated by the high M-squared value. The M-squared was equal to 1.13 in the horizontal direction and 1.47 in the vertical direction. For pulsed operation, Q-switching was demonstrated using an acousto-optic modulator. A Q-switched TEM₀₀ pulse with an average power of around 10W was achieved. A clean Q-switched pulse was obtained from pulse repetition rates from 40 - 460kHz. At 40kHz, the maximum pulse energy (162μJ) was achieved and this decreased with increasing repetition rate due to lower amounts of stored energy in the gain medium.

The final part of the chapter was a demonstration of NLM mode-locking incorporated within the bounce geometry configuration. The intensity dependence of the nonlinear mirror was provided by a combination of a nonlinear crystal (BIBO) and dichroic output coupler. This experiment is based on the asymmetric cavity, which was extended to increase the cavity round-trip time, and thus the pulse energy. The total length of the cavity was extended to around 140cm using two spherical lenses in a 4f system. This resulted in a self-started mode locked pulse train with a repetition rate of 113MHz. An average power of 9.1W was achieved from a pump power of 53W. This corresponds to an optical-to-optical conversion efficiency of 17%. The results from the autocorrelation trace show that the main mode locked pulse was accompanied by many satellite pulses. The pulse duration of the 'main' pulse was 25ps assuming Gaussian pulse shape.

3 Versatile Pulse Laser Sources for Industrial Applications

3.1 Introduction

Pulsed laser sources are useful for industrial applications such as drilling, cutting, high precision micromachining and laser marking [5]. Common methods for producing pulsed laser sources such as Q-switching and Mode-locking have proven to have good efficiency and high beam quality [45][83]. Among laser sources, diode-pumped solid-state lasers such as Nd:YAG and Nd:YVO₄ are proven sources of pulsed power with good efficiency and high beam quality. Most variable pulse rate solid-state lasers are achieved using active Q-switching, typically producing pulse durations of ~10–100ns, although sub-nanosecond pulses can be achieved from passively Q-switched microchip Nd:YVO₄, Nd:GdVO₄ and Nd:YAG lasers with ultra-compact cavities [84]–[86]. However, Q-switched laser systems are limited in pulse versatility since the pulse rate, pulse energy and pulse duration are in general not independent but interlinked by the stored inversion and cavity dynamics.

Another approach to producing versatile pulsed laser sources is by amplifying a seed source with variable pulse parameters in a master oscillator power amplifier (MOPA) configuration. The MOPA approach with diode seed is extensively used in high gain fibre laser systems, often using a series of fibre amplification stages [87], [88]. However, a difficulty arises in fibre amplifiers due to high amplified spontaneous emission (ASE) and, more significantly, the onset of optical damage and fibre nonlinearity that typically limits the pulse energy and achievable peak power [89]. An alternative approach involves amplification using a bulk solid-state gain medium. However, except for a recent work by Delen et al. [90], this approach usually provides limited gain [91][92]. An exception to this is the ultra-high gain

that can be achieved in the bounce amplifier geometry [48][50][93]. In chapter 2, Nd:YVO₄ in a bounce geometry has been shown to be an effective gain medium for continuous (CW), Q-switching and mode-locking in an oscillator. Following from the previous chapter, this chapter continues use of Nd:YVO₄ in a bounce geometry as a gain medium in the amplification stages based on MOPA configurations.

In this chapter, firstly, a laser diode seed system will be described. A versatile pulsed seed laser source is produced based on a gain-switched semiconductor laser diode. There are two amplification stages, called the pre-amplifier and power amplifier. In a preamplifier, initially, the effect of bounce angle on the gain are studied analytically and experimentally using CW Nd:YVO₄ as a seed laser. After that, the experimental results from both amplifiers for variable pulse parameters will be presented. Finally, the temporal and spatial characteristics of the amplified pulsed lasers will be discussed.

3.2 Experimental Systems

The schematic diagram of the versatile MOPA pulse source is shown in Figure 3.1. The system comprised a pulsed seed laser at 1064nm and two stages of amplifiers called pre-amplifier and a power amplifier, both based on Nd:YVO₄ gain medium in the bounce geometry configurations.

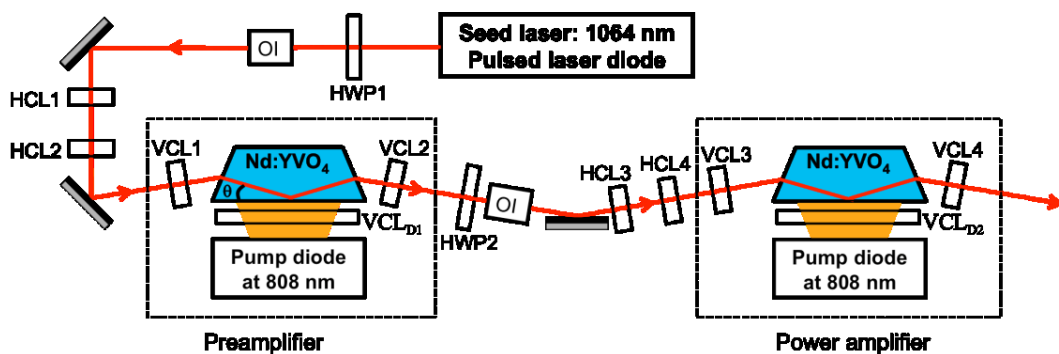


Figure 3.1: Schematic diagram of the MOPA system with gain-switched diode laser seeding a pre-amplifier and power amplifier, both in the bounce geometry. HCL and VCL are horizontal and vertical cylindrical lenses, respectively; OI are optical isolators and HWP are half waveplates.

3.2.1 Pulsed Laser Seed System.

The pulsed seed source used in this system was a semiconductor laser diode. The laser diode was connected to a pulsed electrical driving circuit for gain-switched operation. The electrical drive circuit was capable of generating an optical pulse durations from 3.5ns to over 10 μ s with adjustable pulse repetition rate, ranging from single shot up to 2MHz. The minimum pulse duration of this system was limited by the finite inductance of the laser diode and the cabling system, rather than being a fundamental limit.

The laser diode was spatially single mode and had a nominal free-running wavelength of 1064nm, and CW rated power of 200mW. It was housed in a 9mm TO-can package and temperature stabilised with a thermo-electric (Peltier) device. It was collimated with an aspheric lens producing an elliptical (~3:1 ratio) spatial output but with near-diffraction-limited beam quality. Figure 3.2 (a) shows the spatial and spectral output of the seed laser diode (after two horizontal cylindrical lenses (HCLs) in Figure 3.1). The M^2 beam quality of the beam was determined using the ISO 11146-1 method, based on the second moment beam size. The beam quality was measured to be 1.1 and 1.3 in a horizontal and vertical respectively. Figure 3.2 (b) show the spectral output of the seed laser diode. The diode has spectrally multimode output due to the nature of its Fabry-Perot cavity.

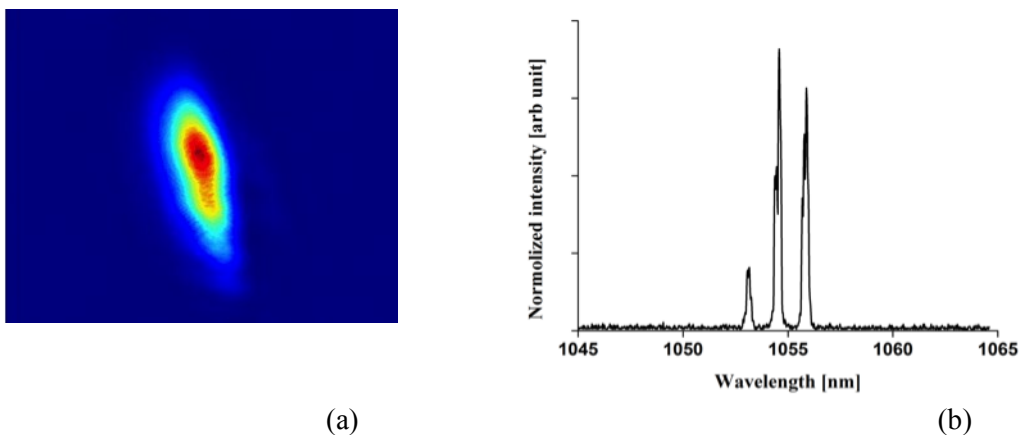


Figure 3.2 Seed laser diode output (a) spatial after two HCLs (b) Spectrum

Figure 3.3 shows the output spectrum of the laser diode for different temperatures. The centre of the wavelength increases proportionally with temperature. However, the laser exhibits mode hopping, where the lasing wavelength hops over discrete wavelength. Mode hopping and the discrete longitudinal mode spectrum meant that the wavelength could not be continuously tuned, nor fully matched in general to the narrow (<1nm) gain bandwidth of the Nd:YVO₄ amplifiers.

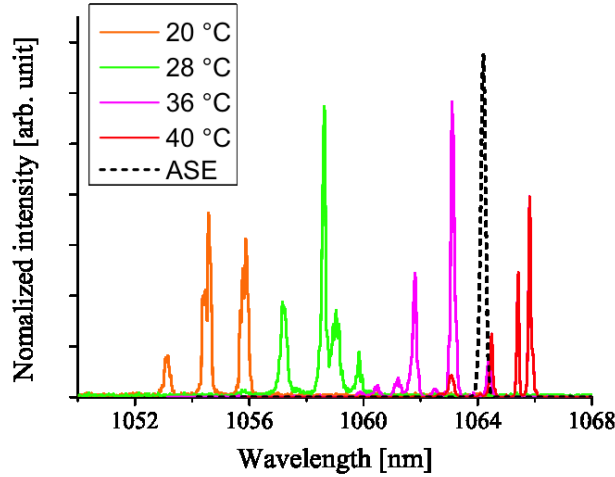


Figure 3.3: Laser diode spectrum at different temperatures and also shows ASE spectrum of bounce Nd:YVO₄ amplifier .

The wavelength of the laser diode was therefore tuned using a diffraction grating. The laser diode was set up with an external cavity in the Littman-Metcalf configuration as shown in Figure 3.4 [94]. For light incident on the grating, the diffraction pattern is determined by [94],

$$m\lambda = d(\sin \theta_i + \sin \theta_m) \quad \text{Eq. 3.1}$$

where m is an integer defining the diffraction order, λ is the wavelength of the incident light, d is the grating spacing and θ_i and θ_m are the incident and diffracted angles respectively. In this configuration, the zeroth diffraction order ($m = 0$) was used as the laser seed output and the first diffraction order ($m = 1$) was directed to a mirror for tuning the laser wavelength. The mirror was oriented so a fraction of incident light was returned to the laser diode as optical feedback. Because the angular position of the diffraction peaks are a function of wavelength, the optical

feedback wavelength could be tuned by adjusting the angle of the mirror's surface with respect to the incident light. Because the laser will work most efficiently at the optical feedback wavelength the laser wavelength is effectively tuned. An important feature of the Littman-Metcalf configuration is that the angle of the laser seed output remains fixed as the wavelength is tuned because the zeroth diffraction order is independent of the wavelength.

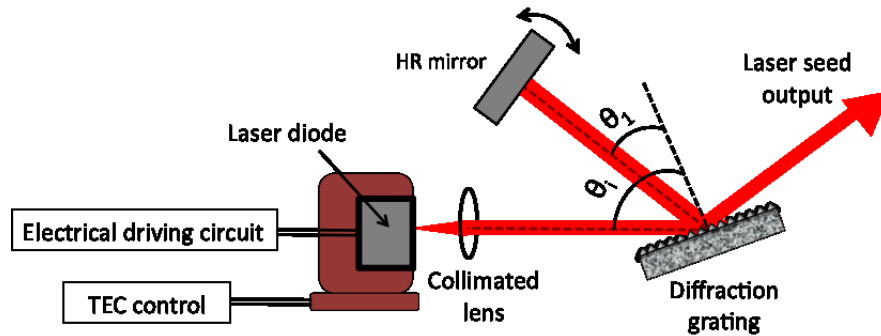


Figure 3.4: Laser diode system with external cavity using Littman-Metcalf configuration. HR mirror has high reflection $\sim 1064\text{nm}$. The laser seed output wavelength was tuned by rotating the HR mirror.

Figure 3.5 shows the spectrum produced from the diode seed with an external grating. The output laser had a single longitudinal mode and its spectral bandwidth was measured to be $< 1\text{GHz}$ (the limit of spectral resolution of the measurement etalon). The seed laser was wavelength tuned to match the peak in the spectrum of the ASE from the pre-amplifier gain module, which occurred at a centre wavelength of $\sim 1064.2\text{nm}$.

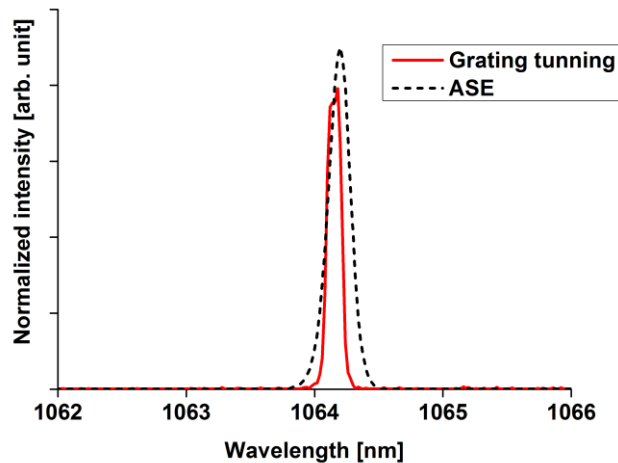


Figure 3.5: Spectrum of laser diode using external diffraction grating to tune the frequency compared with the spectrum of an amplified spontaneous emission of the gain medium.

The power of the seed laser could be varied by the electrical driving circuit, but fuller variation of power (by several orders of magnitude) in this study was accomplished by using an external optical attenuator based on adjusting a retardation half-waveplate (HWP) placed before the first optical isolator (OI) (see Figure 3.1). The OI was included to minimize unwanted feedback to the diode seed from the ultra-high gain amplifier that could affect the gain measurements and potentially cause optical damage to the diode laser itself.

3.2.2 Preamplifier and Power Amplifier

The pre-amplifier and power amplifier were both based on 1.1 at. % Nd:YVO₄ crystal using bounce geometry configuration. The crystal was side-pumped by a laser diode bar emitting at 808nm, which was anti-reflection (AR) coated for the pump wavelength. The two end laser faces were AR coated at 1064nm. The heat was removed from the top and bottom faces of the crystal using water-cooling system, setting at 20°C. The crystal ends were cut angled to minimize parasitic lasing effects occurred from unwanted internal oscillations in the gain medium. The crystal face in this study was cut at 14°, which leads to bounce angle of about 7° when the input beam is parallel to the front face of the crystal.

For the pre-amplifier, the pump diode bar was focused onto the crystal by a vertical cylindrical lens (VCL_{D1}) with $f = 6.35\text{mm}$, creating a pump dimension of $\sim 50\mu\text{m}$ in a vertical direction and $\sim 15\text{mm}$ in a horizontal direction. Two horizontal cylindrical lenses (HCL1, HCL2) with $f = 200\text{mm}$, -50mm formed a reducing telescope to create a horizontal seed mode diameter $\sim 1\text{mm}$ at the pre-amplifier. In a vertical direction, a vertical cylindrical lens (VCL1) with $f = 50\text{mm}$ was used to spatially match the seed beam to the vertically narrow gain region of the pre-amplifier. A second vertical lens VCL2 ($f = 50\text{mm}$) placed after the pre-amplifier was used to re-collimate the beam in the vertical dimension. The HWP2 and OI were placed to minimize the feedback from the power amplifier. The OI introduced loss to the system of approximately 10%.

The power amplifier was placed at a distance approximately 50cm away from the preamplifier in order to reduce the acceptance angle of ASE from the pre-amplifier system entering the power amplifier. For the power amplifier, the pump diode bar was focused onto the crystal by a vertical cylindrical lens (VCLD2) with $f = 25\text{mm}$ producing pump height $h \sim 200\mu\text{m}$. Two horizontal cylindrical lenses (HCL1, HCL2) with $f = 100\text{mm}$, -50mm form a reducing telescope in a horizontal direction by a factor of 2. A vertical cylindrical lens (VCL3) of focal length 100mm was used to spatially match the beam in a vertical direction with the gain in the power amplifier.

3.2.3 Theoretical Analysis of Bounce Geometry Amplifier

As discussed in Chapter 2, the key feature of the bounce geometry involves the laser mode making a path of TIR, or bounce at the pump face of the gain medium. Figure 3.6 shows the schematic diagram of a single pass bounce geometry amplifier where the beam is amplified while traveling through the gain medium.

The crystal is diode pumped over a length l of the pump face. The crystal has an absorption depth for the pump (x_0), indicated by the shaded region. The maximum pump intensity is at the pump face of the crystal and decreases exponentially with penetration distance (x). The local gain coefficient of the amplifier is given by,

$$\alpha(x) = \alpha_0 \exp(-x/x_0) \quad \text{Eq. 3.2}$$

where α_0 is the gain coefficient at the pump face, and the absorption depth of pump beam is $x_0 = l/\alpha_p$ where α_p is the pump absorption coefficient.

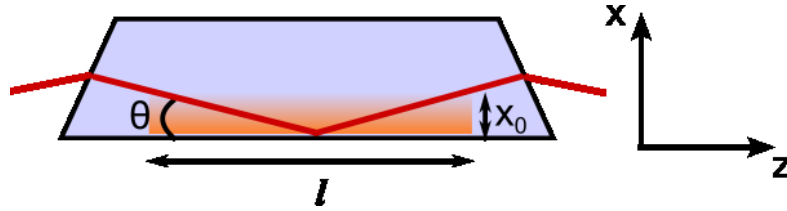


Figure 3.6: Bounce amplifier geometry showing central beam path with bounce angle θ , and pumped length of crystal l , with absorption depth x_0 .

As the beam propagates through the gain medium, the gain (g) can be calculated by integrating the gain-length along the beam path,

$$g = \int \alpha(r) dr, \quad \text{Eq. 3.3}$$

where $\alpha(r)$ is the local gain coefficient. For the central part of the beam, the gain-length product coefficient can be integrated to obtain,

$$g(\theta) = \frac{2\alpha_0 x_0}{\sin(\theta)} \left[1 - \exp\left(\frac{-l \tan(\theta)}{2x_0}\right) \right] \quad \text{Eq. 3.4}$$

Eq. 3.4 shows that the gain coefficient $g(\theta)$ depends strongly on the bounce angle θ , especially at shallow incidence angles, and since the gain (G) is exponentially related to g , the gain (G) can be strongly dependent on angle.

In this calculation, the diode pump is assumed constant over the length of the irradiated pump face l , where l is typically less than the length of the crystal to avoid diffraction effects at the edges of the slab.

The calculation for Eq. 3.4 is for the central ray which experiences the maximum gain through the crystal. The actual gain experienced by the laser mode will be the net amplification of the whole 2D transverse laser mode distribution; hence Eq. 3.4 will be an upper limit on the gain.

Another spatial consideration of the bounce geometry is the projection of the laser mode on the pump face. For a bounce angle θ , a laser beam of transverse diameter

d_0 will have a projection length (l_d) across the pump face. Assuming $\sin(\theta) \sim \theta$ for a small angle, the projection length is equal to,

$$l_d = d_0 / \theta \quad \text{Eq. 3.5}$$

The projection length should be matched to the length of the irradiated pump face (l) for optimal extraction. The projection of the laser mode on the pump face can be controlled by the input size mode size d_0 and / or bounce angle θ . However, it is important to avoid the laser mode excessively overspilling the pump length or, more critically, the slab face itself, causing diffractive clipping that will degrade beam quality. A further spatial issue is that for spatial averaging of the bounce to apply across the beam width, the bounce angle should sufficiently exceed the angle defined by the angular extent of the pump region ($\theta_p = x_0/l$). For this experimental case, the absorption coefficient of Nd:YVO₄ is $\alpha_p \sim 30\text{cm}^{-1}$ ($x_0 \sim 0.33\text{mm}$) and the pump length $l \sim 15\text{mm}$, giving $\theta_p = x_0 / l, \sim 22 \text{ mrad}$ or 1.26° . The minimum bounce angle tested in these experiments was therefore set as $\theta = 3^\circ$.

3.3 Experimental Results

3.3.1 Pre-amplifier Results

The bounce angle was initially investigated using a 1mW CW Nd:YVO₄ seed laser. The pre-amplifier was the bounce configuration described in section 3.2.2. Figure 3.7 shows the average output power as a function of pump power for 3° , 5° and 7° bounce angles. The amplification of 10^3 (gain of 30dB) was achieved at 12W pumping level using 3° bounce angle. However, the gain is highly saturated and does not follow the calculated small signal gain value. The output power at smaller angle was higher than larger angle. This is because the laser mode experiences a longer path near the pump face of the crystal, which has high population inversion. This is in agreement with Eq.3.4. It was also observed that at the smallest bounce angle ($\theta_{\text{bounce}} = 3^\circ$) the laser spatial mode displays some weak clipping in the horizontal direction due to overspill from the pump region and at the crystal edges.

The projection length onto the pump face of the seed beam at $\theta_{bounce} = 3^\circ$ with input seed horizontal diameter $d_0 \sim 1\text{mm}$ is $l_d = d_0 / \sin(\theta) \sim 19.1\text{mm}$, which is close to the slab crystal length of 20mm.

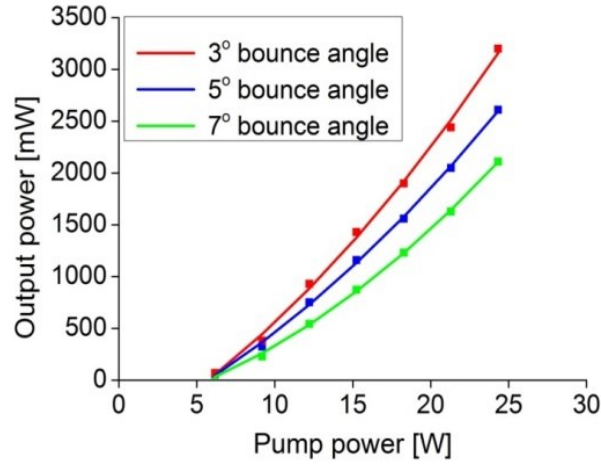


Figure 3.7: Output power versus pump power at different pre-amplifier bounce angles

To preserve spatial quality and to minimize any diffractive clipping effects, the experiment to assess the small signal gain of the amplifier was set up with the $\theta=5^\circ$ bounce angle. The projection length onto the pump face of a 1mm diameter beam at this angle is $l_d \sim 11.5\text{mm}$ which is reasonably well-matched to the pump width ($\sim 15\text{mm}$) and safely within the slab length of 20mm.

In this and all subsequent experiments, the pulsed laser diode seed system described in section 3.2.1 was used. Figure 3.8 shows the gain of the amplifier with varying diode seed average power (using the HWP and OI) for fixed seed pulse duration of 500ns and at a repetition rate of 100kHz. At a seed average power of $2\mu\text{W}$, a small signal gain of $\sim 39\text{ dB}$ (or an amplification of $\sim 10^4$) was measured at 12W pump power. A small-signal gain of $\sim 50\text{dB}$ (or an amplification of 10^5) was measured at 24W pump power. Note that at this pump power level, the ASE could become comparatively high competing for gain with the seed beam. The effect of ASE on the gain of the amplifier will be discussed later on.

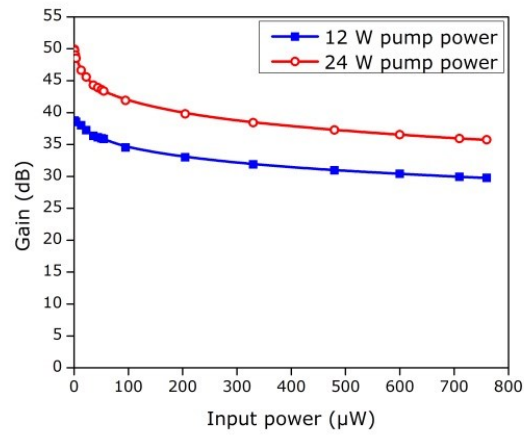


Figure 3.8: Gain of the amplifier in dB as a function of seed power at 5° bounce angle, for two different pump powers.

Figure 3.9 shows the spatial profile of the beam after passing through the pre-amplifier at 24W pump power. The measured beam quality was $M_x^2=1.1$ and $M_y^2=1.4$. Comparing to the input seed laser of $M_x^2=1.1$ and $M_y^2=1.3$ in the horizontal and vertical respectively, this result shows that the beam quality is well preserved in the pre-amplifier.

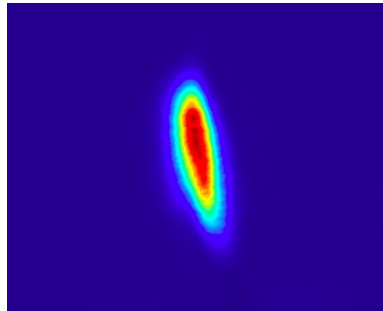


Figure 3.9: Spatial beam profile after passing through the preamplifier.

To quantify further the power scaling potential of a single high gain amplifier stage, the seed power was varied by adjusting the seed pulse duration (10ns; 100ns; 1000ns; 5000ns) at a fixed pulse rate of 100kHz. The corresponding input seed powers to the pre-amplifier were 21μW; 188μW; 1.62mW; and 8.1mW, for the four pulse duration cases, respectively.

Figure 3.10 shows the average output power against pump power at the 5° bounce angle for these four seed input cases. Output power of 6.5W is achieved at 32W pump power for the highest input seed power (8.1mW). However, roll-over at high pump powers was observed for all cases. The power roll-over can be attributed to ASE that becomes comparatively high as the pump power increases, extracting significant power and competing for gain with the seed beam. As the seed pulse duration and hence input seed power increases, the output power rollover was observed to occur at higher pump power. This is explained by the increased gain saturation that occurs for large seed input that reduces the level of ASE, compared to the lower seed case. In general, however, the single amplifier becomes ASE limited and for higher power scaling it is therefore necessary to incorporate a further power amplifier module.

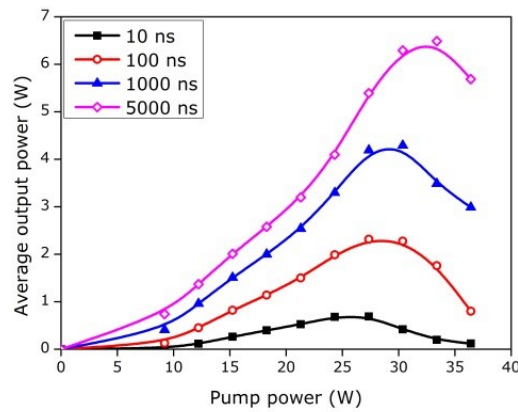


Figure 3.10: Output power versus pump power for different input seed pulse durations (and hence seed powers).

3.3.2 Power Amplifier Results

The details of the power amplifier are given in Section 3.2.2. The main difference compared to the pre-amplifier is the longer diode vertical focusing lens (VCL_{D2}) used ($f = 25\text{mm}$, compared to $f = 6.35\text{mm}$ for the pre-amplifier) to give a larger vertical pump size as this amplifier is more concerned with power extraction than achieving the highest gain. With less intensive pumping the ASE issues are also reduced. The power amplifier was operated at 5° bounce angle, as with the

pre-amplifier. The pre-amplifier pump power was fixed at 24W in the following experiments.

Figure 3.11 shows the average output power after the power amplifier stage as a function of diode pump powers for different seed pulse durations (FWHM). The variation of seed pulse duration controls proportionately the average power of the seed. A maximum output power of $\sim 14\text{W}$ was obtained from 100ns (188 μW) seed pulse and 55W pump power into the power amplifier.

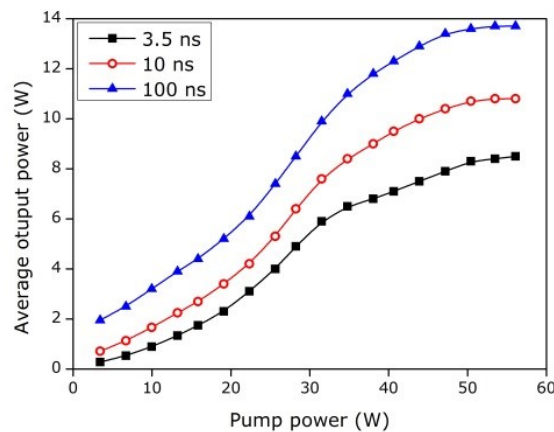
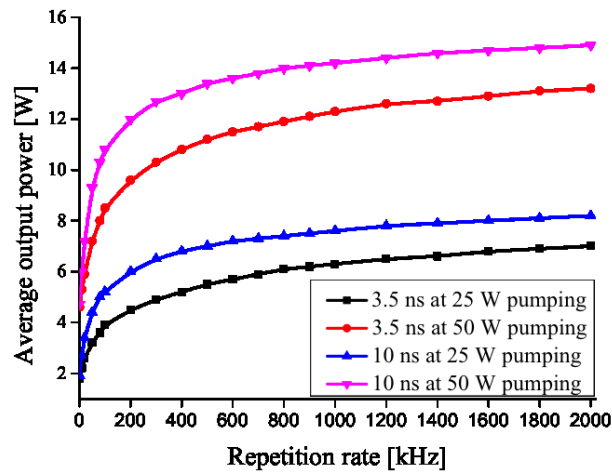


Figure 3.11: Average output power for different pulse durations, with varying pump power, at 100kHz.

The average output power after the power amplifier with varying repetition rate is shown in Figure 3.12 (a) for two different seed pulse durations (3.5ns and 10ns), at 25W and 50W pumping of the power amplifier. The average output power increases with repetition rate, since the seed input power is increasing. At low repetition rates, the output power increases rapidly (quasi-linearly) but tends to reach an asymptotic limit at high repetition rates due to gain saturation. Figure 3.12 (b) displays the corresponding peak power for the case of the 3.5ns pulse seed. The peak power is highest at lower repetition rate as the time between pulses was longer, accessing a higher population inversion at the time the pulse arrives at the gain medium. A peak power of 42kW was obtained at a repetition rate of 50kHz at 50W pumping to the power amplifier.

(a)



(b)

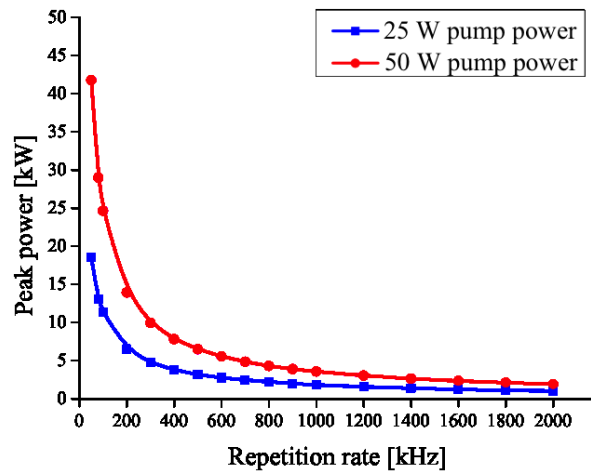


Figure 3.12: (a) Average output power with varying repetition rate. (b) Peak pulse power with varying repetition rate for fixed seed input duration 3.5ns. Note that the input seed average power changes proportionately with repetition rate change.

At 25W pumping to the power amplifier, the beam quality was measured to be $M_x^2=1.3$ and $M_y^2=1.1$ and at 50W pumping, the beam quality $M_x^2=1.5$ and $M_y^2=1.1$. Further optimisation of the system would improve the beam quality. No obvious parasitic lasing was observed. It is noted that at full pump power (55W), the thermal lensing due to the power amplifier in the horizontal direction was very strong, creating a thermally-induced focal length of approximately 60mm. The output beam however was readily re-collimated using a suitable HCL at an appropriate distance from the amplifier.

Figure 3.13 shows temporal profiles comparing the laser diode seed input and amplified output pulses after two amplification stages. Figure 3.13 (a) shows the “Gaussian-like” temporal profile for a seed with pulse duration of 3.5ns at 100kHz repetition rate and shows that the changes in pulse shape and pulse duration were small after amplification. Figure 3.13 (b) shows the temporal profiles for “square-shaped” seed with pulse duration of 60ns. The pulse has a sharp rising edge followed by exponential decay due to the effect of gain saturation as the trailing pulse edge sees lower gain than the leading edge. This effect was even more apparent at low repetition rates, where the gain is higher and the gain saturation changes more appreciably during the pulse duration. However, pulse reshaping could be undesirable for some applications where pulse shape and pulse duration is critical. In general, the rectangular optical output pulse in a MOPA system could be achieved by reshaping the optical seed waveform to compensate the effect of gain saturation [95].

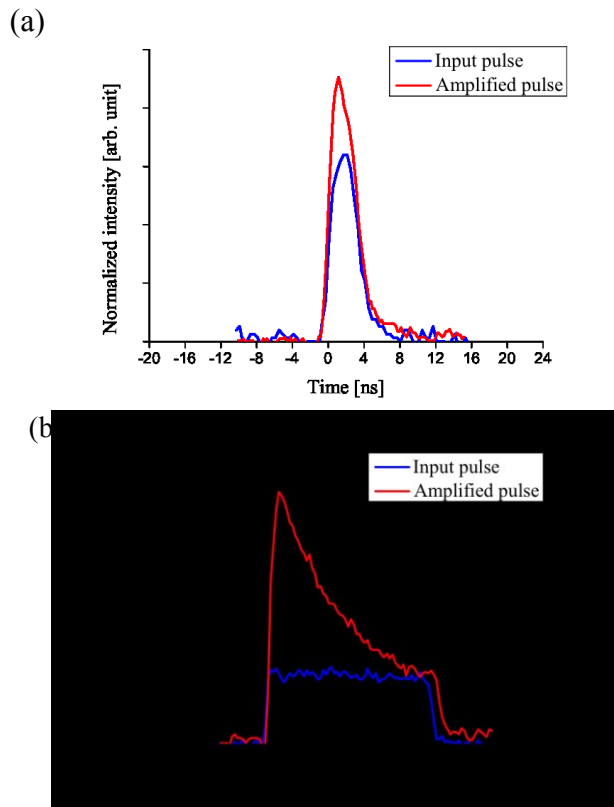


Figure 3.13: Temporal profile of laser diode seed and amplified pulse. (a) Seed pulse duration of 3.5ns, showing negligible pulse shortening. (b) Seed pulse duration of 60ns, showing the FWHM pulse duration decrease to 21ns due to pulse reshaping by gain saturation.

3.4 Conclusion

This chapter presented a study of the use of a low power, gain-switched diode seed and ultra-high gain bounce geometry Nd:YVO₄ amplifier system to create a versatile pulsed source at 1064nm. Firstly, a seed diode system has been described. The seed diode laser was driven by an electrical driving circuit, which allowed independent control of the pulse duration and repetition rate. The pulse duration ranged from 3.5ns and the pulse repetition rate from single shot to 2MHz, limited only by the diode driving circuit. The wavelength of the seed laser diode was tuned using an external grating to match the high gain bandwidth of the Nd:YVO₄.

The key feature of the bounce amplifiers, the geometry used in this setup, was presented. The output power and gain obtained from different bounce angles and pump powers from a pre-amplifier was investigated experimentally. Small signal gain of 50dB was demonstrated from a pre-amplifier with just 24W pumping. At higher pump powers, the amplifier becomes limited by competition from ASE. The beam quality was well preserved in this stage of amplification.

The second bounce geometry amplifier was necessary for amplifying to further power scaling. With the power amplifier, an average output power of ~14W was achieved for a diode seed input with 188 μ W power, 100ns pulse duration at 100kHz. As the repetition rate increases, average output power initially increases rapidly and reaches a limit at high repetition rate due to gain saturation. The highest peak power was obtained at the lowest repetition rate. For 3.5ns pulse duration, a peak power of 42 kW was achieved at 50kHz. The beam quality was measured to be $M_x^2 = 1.5$ and $M_y^2 = 1.1$ for 50W pumping. The pulse reshaping effect was observed especially in long pulses due to gain saturation. Further optimization of the system would improve the temporal and spatial output characteristics.

In this study, the bounce geometry has demonstrated the use of the bounce geometry amplifier for flexible pulse amplification. However, the pulse duration was limited by the laser diode driver. In fact, higher peak power can be obtained using a seed laser with sub-nanosecond or picosecond pulse seed and hence to address a wider class of applications.

4 Alexandrite Laser

4.1 Introduction

A wide laser wavelength tunability range has proved to be useful in a number of applications such as in basic scientific investigations, in atomic trace gas monitoring, and in several medical applications. There are many lasers in which the frequency can be varied over a large fraction of its central frequency such as the liquid medium dye lasers. However, the interest in solid-state laser has increased significantly in the last few decades. Compared to the dye lasers, solid-state gain media offer near unlimited operating lifetime. Pump sources will limit the solid-state laser lifetime (lamp ~1000s hours and diode ~10,000s hours). They can also have significant energy storage capability owing to long upper state lifetime, enabling the generation of high peak powers via Q-switching. In addition, the tuning range in some vibronic solid state lasers is broader than in dye lasers and extends further into the infrared region. Among tunable solid-state lasers the Titanium-doped sapphire, or Ti:Al₂O₃, laser has the largest tuning range, from 670 to 1070nm [17]. It is widely used as a tunable laser due to its excellent thermo-mechanical properties [17]. Ti:Sapphire lasers can also generate very short pulses. Using the Kerr-lens modelocking technique mode locked pulses as short as 5 fs generated directly from a laser oscillator were achieved in 2001 [96]. A drawback of Ti:Sapphire is the lack of the high power pump laser diodes around its absorption peak at ~500nm. Currently, Ti:Sapphire lasers are predominantly pumped by frequency-doubled diode-pumped neodymium lasers [96][97]. In these systems, the overall efficiency is low and system cost is usually expensive.

Cr³⁺ doped lasers have broad absorption bands that include the red part of the spectrum [17]. This allows efficient direct diode pumping with available red diode lasers in visible region [98]. These Cr³⁺ -doped lasers can provide broadly tunable

operation with tuning ranges $\sim 100\text{nm}$, and center wavelength around 800nm depending on the particular crystal host [18]. The Cr^{3+} -doped laser media such as $\text{Cr}^{3+}:\text{LiSrAlF}_6$ (usually abbreviated to $\text{Cr}:\text{LiSAF}$), $\text{Cr}^{3+}:\text{LiCaAlF}_6$ ($\text{Cr}:\text{LiCAF}$), and $\text{Cr}^{3+}:\text{BeAl}_2\text{O}_4$ (Alexandrite) are biaxial in nature and results in the absorption and emission spectra being strongly polarization dependent.

For $\text{Cr}:\text{LiSAF}$, the pump bands are in the range from $550\text{-}700\text{nm}$ and $400\text{-}500\text{nm}$, and the vibronic transition offers wavelength tunability from $780\text{--}1010\text{nm}$ [3]. In 1991, a tunable flashlamp-pump $\text{Cr}:\text{LiSAF}$ laser with long pulses and Q-switched pulses of $40\text{--}50\text{ns}$ with output energy of 150mJ was demonstrated [99]. As the absorption peak is around 650nm , it is possible to pump using $\text{GaInP}/\text{AlGaInP}$ quantum well laser diodes operating at 670nm . The first diode pumped $\text{Cr}:\text{LiSAF}$ laser was built by Richard et al. and they obtained a CW output power of 19.9 mW . In 1997, power output as high as 1.42W CW was obtained using a 15W diode laser array [100]. This high power resulted from optimized mode-matching between the pump beam and the cavity mode, combined with a specialized crystal size and cooling geometry. The broad emission bandwidth of the $\text{Cr}:\text{LiSAF}$ also supports the generation of femtosecond pulses. The first mode locked $\text{Cr}:\text{LiSAF}$ lasers using diode pumping were demonstrated by French et al. and Rizvi et al [101], [102] and pulses as short as 10fs were achieved using Kerr lens modelocking in 2000 [103]. The availability of inexpensive single mode laser diodes as pump sources led to compact and effective femtosecond lasers. Mode locked pulses as short as 113fs with an average power of 20mW from only 110mW laser diode pump power were achieved in 2002 [104]

There have been relatively fewer studies of $\text{Cr}:\text{LiCAF}$ as $\text{Cr}:\text{LiSAF}$ has a larger optical gain cross-section, and the tuning range is larger. However, thermal quenching of $\text{Cr}:\text{LiCAF}$ occurs at a relatively high temperature of 255°C compared to $\sim 69^\circ\text{C}$ for $\text{Cr}:\text{LiSAF}$ [105]. This favorable thermal property of $\text{Cr}:\text{LiCAF}$ and the improvement in crystal growth and high power diode lasers make $\text{Cr}:\text{LiCAF}$ another promising candidate for efficient tunable CW and femtosecond lasers using standard cavity configuration.

The tunability of the Alexandrite laser was discovered by J. C. Walling et al. in 1979 [106]. After the development of crystal growth techniques, Alexandrite

became the first commercial tunable solid state lasers with a tunability range of 700 - 820nm for the fundamental wavelength. The extension of the spectral region to the UV and IR can be obtained through nonlinear processes including SHG (second harmonic generation) and SRS (stimulated raman scattering). In 1980, J.C. Walling reported a 6.5 W CW Alexandrite laser using Mercury arc lamp pumping [107]. Longitudinal pumping of Alexandrite by a krypton laser exhibited very high efficiency, with slope efficiencies of up to 51% [108]. A long pulse average power of 150W at 125Hz and 750nm was obtained by J. C. Walling in 1985 [15]. Alexandrite has a long upper state lifetime of 260 μ s, comparing to 67 μ s and 170 μ s for Cr:LiSAF and Cr:LiCAF respectively. This makes Alexandrite suitable for Q-switched operation as it allows a significant amount of energy to be stored in the system. For example, Q-switched pulses with an energies of 2J and 40ns duration at a pulse rate of 20Hz has been observed [15]. In active Mode-locked operation, a pulse duration of 160ps was demonstrating using an acousto-optic modulator [15]. Pulses as short as 8ps were also reported from passive mode-locking using a saturable absorber [109]

Most of the earlier work on Alexandrite was based on lamp-pumping or pumping by other lasers, such as argon and krypton lasers, which makes the whole system inefficient and expensive [110], [111]. The first diode-pumped Alexandrite laser was demonstrated in 1990 by R. Schep allowing a prospect of compact laser setups and an efficient pump system [112]. However, the output power was limited to a few mW. The recent availability of high power red diodes allows efficiency pump Alexandrite laser at high power level.

In this work, we will focus on Alexandrite lasers using high power red diode at 636nm as pump sources. The aim of this chapter is to provide a general understanding of Alexandrite and its properties, overview of prior laser performance and its applications. Firstly, the physical properties of Alexandrite will be described. This will be followed by laser properties that include a description of the unique energy levels of Alexandrite, which leads to an ability to increase the performance at elevated temperature, and the effect of excited state absorption (ESA). The spectral variation of the ESA cross section $\sigma_{esa}(\lambda)$ in the Alexandrite lasers plays an important role on its performance as a laser. In the second part,

pump sources for Alexandrite will be discussed, comparing between lamp-pumping and diode pumping in details. Following by a thermal analysis of diode pumping in an end-pumped configuration, which is the main pumping configuration of Alexandrite laser in this thesis. Finally, this chapter will be concluded by the applications of Alexandrite, including those that are current and potential future applications.

4.2 Alexandrite Physical Properties

Alexandrite is a natural gemstone which is well known for its hardness and the property that it changes color from bluish-green to red, depending on the lighting condition. As a laser material Alexandrite, or Chromium-doped chrysoberyl ($\text{Cr}^{3+}:\text{BeAl}_2\text{O}_4$) can be grown by melting mixture of aluminum oxide (Al_2O_3), beryllium oxide (BeO) and chromium oxides (Cr_2O_3) and using technique called the Czochralski method [113]. The structure of Alexandrite is shown in Figure 4.1. The host material Chrysoberyl has an orthorhombic structure Pnma , which has four molecules per unit cell. The aluminum ions (Al^{3+}) are octahedral coordinated with Oxygen ions, and occur in two unequal crystal field sites; mirror symmetry and inversion symmetry. When the chromium ions (Cr^{3+}) replaces some of the Al^{3+} ions in a BeAl_2O_4 crystal, it was found that 78% of the Cr^{3+} ions reside in the mirror symmetry site and the remaining 22% in the inversion sites [114]. The mirror symmetry site usually has the major effects on Alexandrite laser properties, and the inversion sites are mostly inactive to the absorption and emission properties.

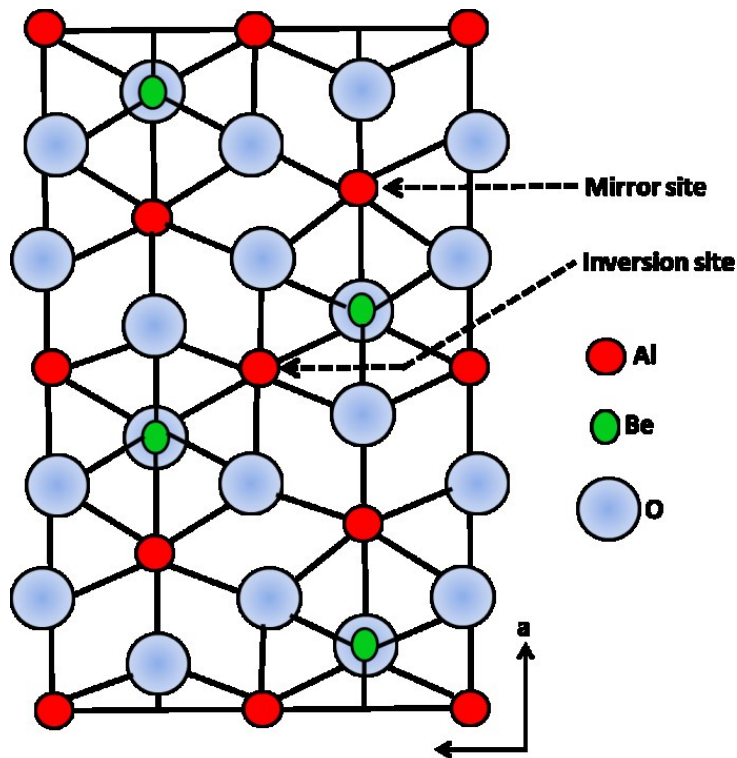


Figure 4.1: C-axis view of structure of Chrysoberyl.

Compared to Nd:YAG and other tunable lasers, Alexandrite has a relatively low emission-cross section ($\sim 7 \times 10^{-21} \text{ cm}^2$ at room temperature). However, Alexandrite has high thermal conductivity, good strength and hardness, chemical stability and high fracture limit, which holds advantages for high power laser applications. A CW laser with a power of over 60W has been achieved in an Alexandrite rod with size 6mm in a diameter and 10mm in length in 1985 [15]. Table 4.1 shows some of the optical and mechanical properties of Alexandrite at room temperature relative to Nd:YAG and some others important tunable lasers (Ti:Sapphire and Cr:LiSAF).

	Alexandrite	Nd:YAG	Ti:Sapphire	Cr:LiSAF
Peak wavelength	760	1064	790	850
Tuning range	700-820	-	660-1180	780-1010
Stimulated emission cross section[$\text{cm}^2 \times 10^{-20}$]	0.8	28	28	4.8
Spontaneous lifetime[μs]	260 (T=298k)	230	3.2	67
Linewidth [THz]	53	0.135	100	83
Doping density [at%]	0.05-0.30	1	0.1	Up to 15
Thermal expansion [$10^{-6}/\text{k}$]	E/b 6.1	7.5	~ 5	22
Thermal conductivity [W/cmK]	0.23	~ 0.14	0.33	0.03
Melting point [$^{\circ}\text{C}$]	1870	1970	2040	766
Hardness [kg/mm^2]	2000	1320	-	-

Table 4.1: The optical and mechanical properties [3], [17], [18][115].

4.3 Alexandrite Laser Properties

4.3.1 Energy Levels

The energy level system of Alexandrite is shown in Figure 4.2. Figure 4.2 (a) shows the energy levels in a configuration coordinate diagram. When the ion is pumped to the 4T_2 or 4T_1 bands, it has a rapid non-radiative decay to both the bottom of the 4T_2 bands and the long-lived 2E level. Alexandrite can operate as a 3-level or 4-level laser. The 3-level laser scheme is shown in Figure 4.2 (b). The laser transition occurs from the 2E level to the ground level (4A_2). The emission wavelength of Alexandrite at this transition is at 680.3nm at room temperature. This level is actually a doublet R_1 (680.3nm) and R_2 lines (678.5nm) but the 680.3nm has the stronger cross-section for lasing [116]. This transition is, in fact, similar to that of ruby. However, when operated as a 3-level laser it has high threshold, fixed wavelength and relatively low efficiency.

The important operating regime of Alexandrite is as a 4-level system. In a 4-level system, as shown in Figure 4.2 (c), the lasing transition occurs from the lower

energy level of the 4T_2 to the vibrationally excited level ${}^4A_2^*$. This results from a displacement of equilibrium coordinate for 4T_2 level. From the vibrationally excited level of 4A_2 , the rest of the energy will dissipate as a phonon relaxation, returning the ions in the unexcited ground state. As there are effective continuums of vibrationally excited levels of 4A_2 , therefore, the fluorescence emission has a broad spectrum, which ranges from $\sim 650\text{-}870\text{nm}$.

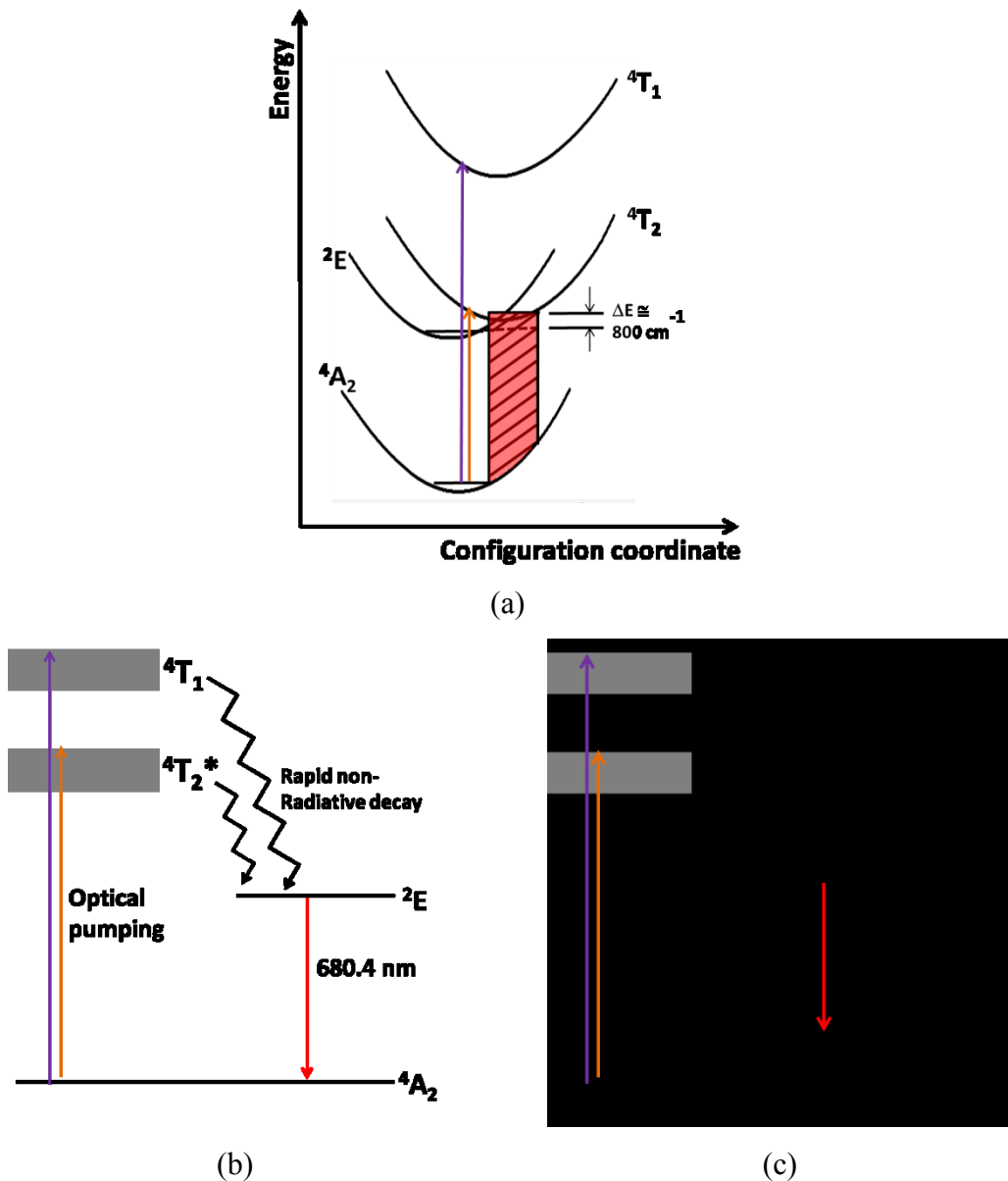
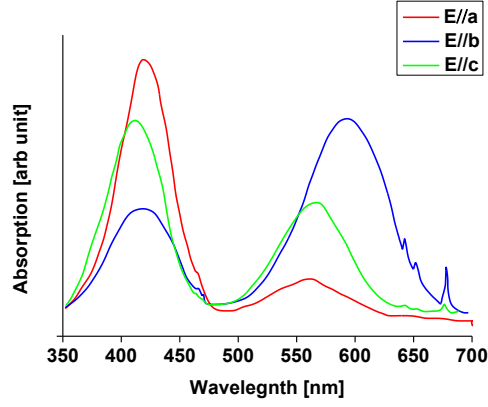
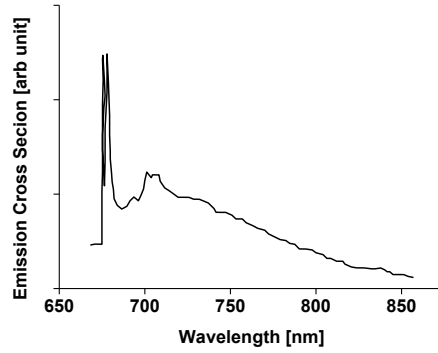


Figure 4.2: (a) Simplified energy diagram of Alexandrite in configuration coordinate (adapted from [18]). (b) Energy level shows 3-level diagram of Alexandrite laser (c) Energy level shows 4-level diagram. A star indicates mean vibrationally excited level.

One important characteristic of Alexandrite is the polarization dependence of the absorption and emission spectra. The absorption spectrum of Alexandrite is shown in Figure 4.3 (a). The absorption bands spread from 300nm (not shown in graph) to ~700nm [114]. There are two broad bands centered around 420nm and 580nm, resulting from the transition from ground state to the two vibronic bands 4T_1 and 4T_2 respectively. Alexandrite is biaxial because of the orthorhombic structure of the host material. The polarization of the absorbed light $E//a$ is highest at the 420nm band, while the $E//b$ is highest at the 580nm band. There is a main sharp absorption doublet line at ~680nm, occurring from the transition from the ground state to the 2E level (R-line). The absorption of Alexandrite is, in fact very similar to the absorption of Ruby. Figure 4.3 (b) shows the fluorescence emission spectrum at room temperature of Alexandrite of the $E//b$ polarization. Light emitted from the Alexandrite laser always has a polarization of $E//b$, due to the ~10 times higher emission cross section when compared to the other two polarizations. The fluorescence spectrum shows strong emission R_1 , R_2 lines at 680.3nm and 678.5nm respectively. The sharp lines are accompanied by a broad spectrum from vibronic band (4T_2) which has its peak at a longer wavelength.



(a)



(b)

Figure 4.3: (a) Absorption spectra of Alexandrite for 3 different polarizations and (b) fluorescence emission spectra of Alexandrite for E//b [data taken from [114]]

4.3.2 Temperature Dependent Characteristics

The vibronic band 4T_2 and the long lived level 2E are in thermal equilibrium, where the fraction of each level is given by Boltzmann distribution. They are very close in energy ($\Delta E \sim 800 \text{ cm}^{-1}$) so the lowest level of 4T_2 band has non-negligible population filling. Due to a fast internal conversion ($< 1 \text{ ps}$), thermalisation among these levels occurs rapidly. In this case, the effective lifetime can be calculated by [18],

$$\frac{1}{\tau_{eff}} = \frac{f_{2E}}{\tau_E} + \frac{f_{2T}}{\tau_T} \quad \text{Eq. 4.1}$$

where f_{2E} is the fraction of the total population of level 2E and f_{2T} is the fraction of the total population of level 4T_2 . The radiative lifetime of the 4T_2 level (τ_T) is $6.6\mu\text{s}$ and the radiative lifetime of the 2E level (τ_E) is 1.5ms . According to the Boltzmann's distribution,

$$f_{2T} = \frac{e^{-(\Delta E / kT)}}{1 + e^{-(\Delta E / kT)}} \quad \text{Eq. 4.2}$$

where ΔE is the energy difference between 4T_2 and 2E ($\sim 800\text{ cm}^{-1}$), and $f_{2E} = 1 - f_{2T}$. As ΔE corresponds to only a few kT , the effective lifetime of Alexandrite is strongly temperature dependent. Figure 4.4 shows the effective lifetime as a function of temperature. The effective lifetime of Alexandrite at room temperature is approximately $260\mu\text{s}$. The lifetime reduces to $\sim 95\mu\text{s}$ at $150\text{ }^\circ\text{C}$.

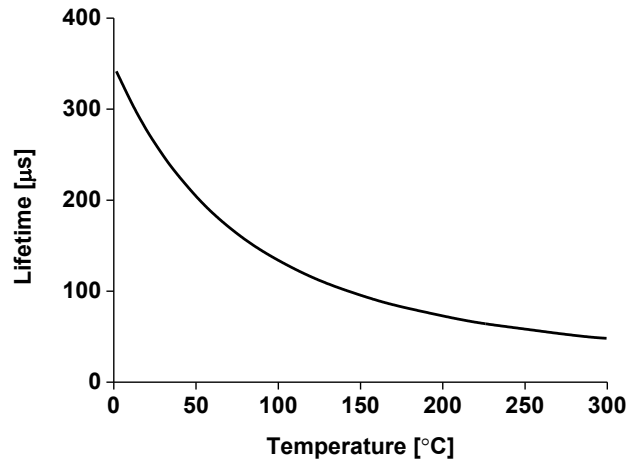


Figure 4.4: Effective lifetime as a function of temperature.

The effective emission cross-section (σ) for the 4T_2 level can be described as,

$$\sigma_{eff} = f_{2T} \sigma_{TA} \quad \text{Eq. 4.3}$$

where σ_{TA} is the actual emission cross section from 4T_2 to 4A_2 . As temperature increases, f_{2T} increases, and therefore σ_{eff} also increases. Figure 4.5 shows σ of Alexandrite with increasing temperature [54]. The σ_{eff} of Alexandrite at room temperature is $\sim 7 \times 10^{-21}\text{ cm}^2$ at 755nm . This value increases by approximately 5 times as temperature increases to $300\text{ }^\circ\text{C}$. Increasing temperature also shifts the emission cross section peak to a longer wavelength. This is because the ions from

ground state populate to a higher level with increasing temperature. Therefore, as the population at the level near the ground increases, there is increasing ground-state absorption at short wavelengths resulting in the peak emission at lower laser photon energy (longer wavelength).

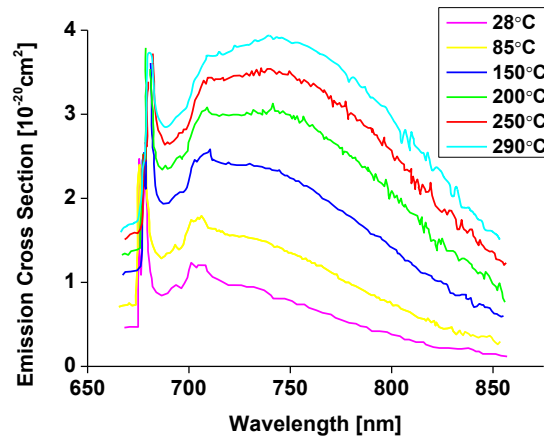


Figure 4.5: Emission spectra of Alexandrite as is varied temperature [data taken from [54]].

4.3.3 Excited State Absorption (ESA)

Excited state absorption occurs when a pump or laser photon is absorbed by Cr ion in the Alexandrite upper laser level (4T_2), promoting it to a higher energy level. In Alexandrite, the ions then non-radiatively decay back to the upper laser level (4T_2). ESA is a loss mechanism as it loses photon but does not contribute to gain of the laser. The effect of ESA is usually to increase the lasing threshold and reduce the laser efficiency. Figure 4.6 (a) shows the ESA cross-section in the pump band of Alexandrite (410 – 670nm) [53]. The graph shows that pump ESA cross-section in Alexandrite is in the same order as magnitude of the ground state absorption cross-section. Therefore, a portion of the pump energy can be directly lost as ESA heating. The loss from ESA becomes more significant as the population in the upper laser level increases.

ESA in the lasing region has an important impact on Alexandrite laser performance, as it decreases the gain and has a direct impact on the Alexandrite tuning range. Figure 4.6 (b) shows the ESA cross section of Alexandrite (red) and the emission cross section (blue) from 700nm to 850nm at 28°C [117]. The graph shows the

emission cross-section σ_{eff} decreases monotonically from 700nm. The ESA cross-section σ_{esa} , however, decreases and reaches a minimum at ~ 768 nm. As the laser gain is proportional to $\sigma_{eff} - \sigma_{esa}$, the optimum lasing wavelength is formed in the intermediate ~ 750 - 760 nm range. The tuning range of Alexandrite is cut off ~ 700 nm at a short wavelength end and ~ 830 nm at a long wavelength end.

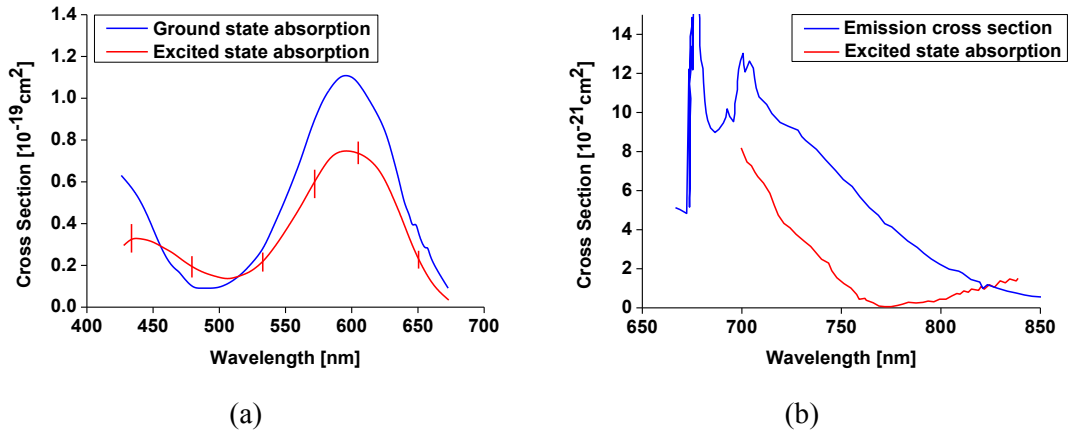


Figure 4.6: (a) ESA and ground state absorption cross-section of the Alexandrite for E//b axis [data taken from [53]] (b) ESA and emission cross section of Alexandrite measured at 28°C [data taken from [117]].

4.4 Pump Sources for Alexandrite

There are two main types of radiation pump source for solid state lasers: lamp pumping and laser diodes pumping. The light generated from lamps is broadband, composed of both line and continuous components ranging from UV to the infrared. For efficient pumping, it is important that the spectrum of the pump source matches the absorption band of the gain medium. As Alexandrite has a broad absorption spectrum ranging from ~ 400 - 690 nm, pumping is possible from different lamp sources [15], [107].

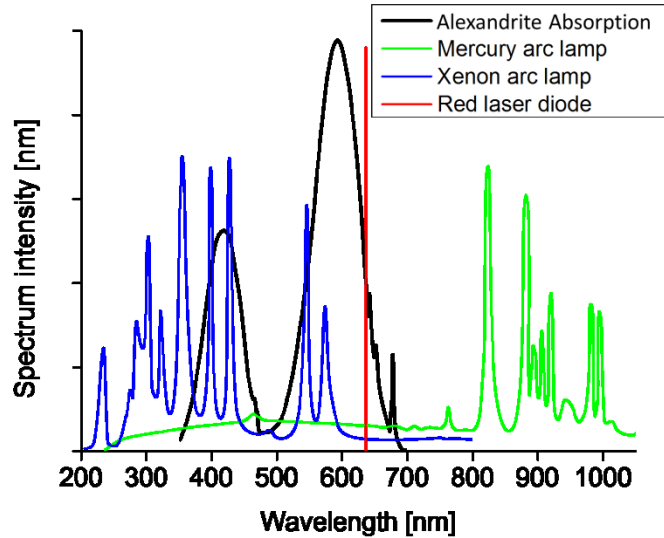


Figure 4.7: Absorption spectra of Alexandrite for E//b, along side with spectra from flashlamps and red laser diode used in this study.

Figure 4.7 shows the absorption spectrum of absorption of Alexandrite, alongside the spectral output from Mercury and Xenon arc lamp. The advantage of lamp pumping is the relatively low cost and an ability to provide very high output power. Under CW operation, output powers of over 60W have been achieved from Hg-arc lamp [15]. Alexandrite has also been operated in both Q-switched and mode-locked mode of operation. Lamp pumping in Alexandrite has been developed for over 20 years and is still commonly commercially used. However, the slope efficiency (η_s) obtained through lamp pumping is usually limited to only a few percent. This is due to the geometry of the system, where in practice only $\sim 50\%$ of the light being coupled to the gain medium. Moreover, a significant proportion of the spectrum from the lamp is not being absorbed. Another disadvantage of lamp pumping is the thermal load. As the ions is typically pumped to higher energy level above the upper laser level, consequently, the ions non-radiative decay to the upper laser level and the energy lost as heat. The thermal loads deposited in the gain medium can lead to thermal lensing and thermally induced stress. Problems associated with thermal lensing will be discussed in detail in Section 4.6. Table 4.2 summaries the performance of the Alexandrite laser using lamp pumping in the literature.

Pump Source	Operation Mode	Pump	Pump	output	Pulse	Pulse	Mode	Slope	Year
		power	energy	power	energy	duration	(M-squared)	efficiency	
		[kW]	[J]	[W]	[J]			[%]	
Hg arc	CW	3	-	6.5	-	-	Multimode	0.8	80 [107]
Hg arc	CW	6	-	60	-	-	Multimode	1.5	85 [15]
Xe arc	CW	8	-	20	-	-	Multimode	0.5	85 [15]
Xe arc	CW	-	-	2	-	-	TEM ₀₀	-	85 [15]
Hg arc	CW	8	-	17	-	-	-	0.5	93 [118]
-	Q-switched	-		-	>1J	<30ns	Multimode	1	82 [119]
Xenon flashlamp	Q-switch	-	280	-	0.18	-	-	0.1	91 [120]
flashlamp	Q-switch	-	90	-	0.014	~100ns	TEM ₀₀	0.04	80 [121]
Flashlamp	Mode-locked	-	-	0.02	-	22ps	TEM ₀₀	-	[109]
Xenon flashlamp	Gain-switched	-	208	-	0.24	85ns	-	-	12 [122]

Table 4.2: Summary of earlier work on lamp pump Alexandrite laser.

Compared to flash lamps or arc lamps, laser diodes have very narrow bandwidths (usually a few nm). The red line in Figure 4.7 indicates the narrow bandwidth of a laser diode used for pumping Alexandrite in this study. As the pump laser diode can be chosen to have a wavelength matched to the line/band of specific solid state material, high pump absorption efficiency (η_p) can usually be achieved. In this scenario the pump photons excite to just above the upper state level, which increase the quantum efficiency (η_Q) and significantly reduce thermal loading in the medium. Diode pumping usually provides an order of magnitude improvement in efficiency compared to lamp pumping. The first diode pumped Alexandrite laser was demonstrated by Scheps in 1990, where the slope efficiency of 25% was obtained. Another advantage of diode pumping is the ability to match the pump beam with the fundamental mode in the gain medium, especially when using an end-pumping geometry. Disadvantages of using laser diodes is that they can be costly and are very sensitive to electro-static discharge. However, with proper operation, high power laser diodes can have a lifetime of over 20,000 hours [16]. Another pump source for Alexandrite is the frequency-doubled Nd:YAG or Nd:YVO₄ laser. They generate narrow bandwidths at wavelength of ~532nm [123].

Second Harmonic Generation(SHG) of a laser can also provide high efficiency in both CW and pulse operation. However, the setup for generating 1064nm and frequency doubling is very complicated, and increases the cost of the whole system. Table 4.3 show a summary of Alexandrite laser output using laser pumping in the literature.

Pump Source	Pump wavelength [nm]	Mode	Pump power [W]	output power [mW]	Pulse energy [mJ]	Pulse duration	Mode (M-squared)	Slope efficiency [%]	Year
Krypton Laser	647	CW	1.6	600	-	-	-	51	83 [108]
Dye laser	645	CW	0.3	150	-	-	-	64	93[124]
SH of Nd:YVO ₄	532	CW	5	1420	-	-	TEM ₀₀	36	06[123]
Single-mode diode	680	CW	2x0.005	-	-	-	-	25	90 [125]
Multimode diode	640	CW	2x0.25	25	-	-	-	28	93 [124]
Tapered diode	678	CW	1	168	-	-	~2.4	38	13 [126]
Tapered diode	678	CW	1	200	-	-	~2.4	34	13 [126]
Argon laser	515	mode-locked	3	10	-	35ps	-	-	89 [111]

Table 4.3: Summary of earlier work on laser pumped Alexandrite laser.

4.5 Thermal Effect for End Pumped Laser Geometry

For high power end pumped laser systems, thermal effects can be severe as the pump energy is delivered into a small area of the gain medium. For rod shaped gain media, a common method to mount the rod is by sandwiching it in a copper cooled heat sink, as shown in Figure 4.8.

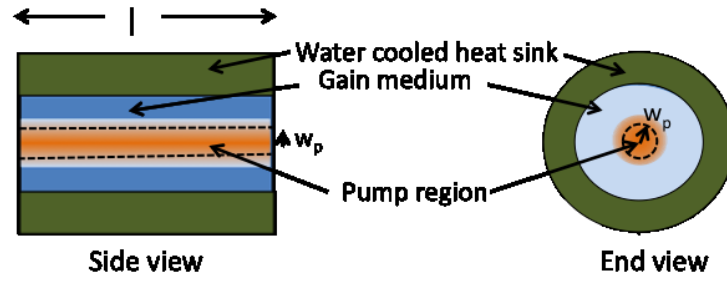


Figure 4.8: Side view and end view of end-pumped laser rod. W_p is the $1/e^2$ radius of the Gaussian transverse pump beam profile.

To simplify modeling the temperature distribution in the gain media we use the fact that the thermal conductivity of the copper is much higher than the gain media (>17 times higher than Alexandrite), so heat energy can be considered to only flow outwards in the radial direction to the outer edges of the rod which is maintained at a fixed temperature by the heat sink. For a Gaussian pump beam, the temperature difference between the rod and the heat sink can be calculated by [127],

$$\Delta T(r, z) = \frac{\alpha P_h \exp(-\alpha z)}{4\pi K} x \left[\ln\left(\frac{r_b^2}{r^2}\right) + E_1\left(\frac{2r_b^2}{w_p^2}\right) - E_1\left(\frac{2r^2}{w_p^2}\right) \right] \quad \text{Eq. 4.4}$$

where P_h is the pump power results in heating, K is the thermal conductivity of Alexandrite, r_b is the radius of the rod and W_p is the pump radius. Figure 4.9 shows the calculated temperature distribution in conductively cooled end-pumped Alexandrite laser rod (2mm x 10mm). This calculation is based on a Gaussian pump transverse beam profile. For a 1W dissipated power, the maximum temperature difference of ~ 7 K arises at the front face of the crystal ($z=0$).

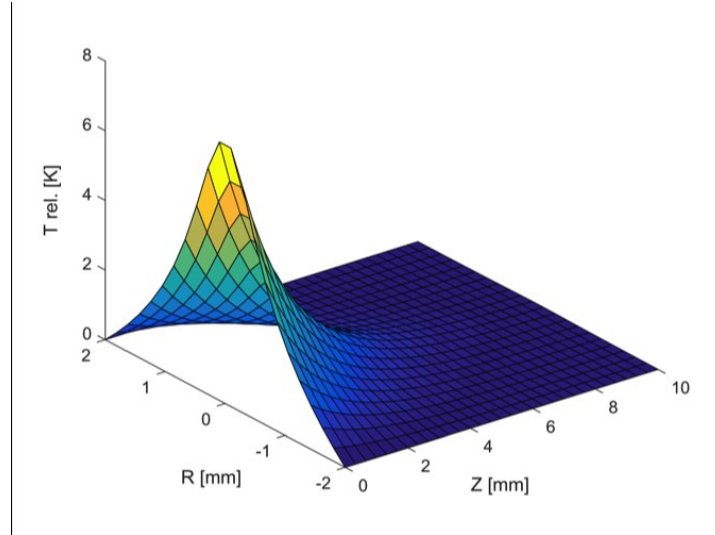


Figure 4.9: Calculated temperature distribution in an end-pump Alexandrite rod laser for thermal dissipated power of 1W based on thermal modeling of CW end pumped solid state lasers. Along the rod axis (in the z-direction), the heat source is assumed to be constant radius of 0.5mm and the heat power decays exponentially due to pump absorption.

As mentioned in Chapter 1, thermal lensing is the most common problem that highly effect laser performance. Thermal lensing not only reduces the cavity stability range in an end-pumped system, but also introduces a phase aberration, which decreases the beam quality. In general, for a low to medium pumping intensity, the refractive index changes due to temperature (dn/dT) is comparatively much more pronounced than thermally induce stress and bulging at end face. For a Gaussian pump beam incident on the rod, considering refractive index changes occurs from the temperature dependent refractive index (dn/dT), the effective focal length of the whole rod can be expressed as [128]

$$f(r) = \frac{2r^2 f(0)}{w_p^2 (1 - \exp(-2r^2/w_p^2))} \quad \text{Eq. 4.5}$$

where $f(0)$ is the effective focal length thermal lens at of the rod axis ($r=0$), which can be expressed as [128],

$$f(0) = \frac{\pi K w_p^2}{P_h (dn/dT)} \quad \text{Eq. 4.6}$$

Across the pump face, the temperature distribution and thus the thermal lensing, is a function of the pump radiation. For a top-hat pump beam, the lens power at the center of the beam has two times less lens power than for a Gaussian pump beam [129]. In addition, the thermal lens is unaberrated within the pump region where $r \leq W_p$. It is worth noted that even though Alexandrite is anisotropic, the measured value of dn/dT of Alexandrite is almost isotropic [130].

4.6 Alexandrite Applications

4.6.1 Current Applications

The unique characteristics of wide tuning range and the ability to operate in CW and pulsed operations, including Q-switch and mode-locking, make Alexandrite laser sources excellent for many applications. Alexandrite was first developed for military purposes by AlliedSignal Corp in 1985. Since then, it has been used in light detection and ranging (LIDAR) applications. Recently, Alexandrite has been widely used in dermatology applications.

Dermatology: Lasers have become increasingly popular in dermatological applications such as hair removal, tattoo removal, vein removal and skin treatment. Alexandrite (700-820nm), along with other lasers such as Nd:YAG (1064nm) and ruby (694nm), has its own unique advantages and disadvantages. In 1977, the FDA (Food and Drug Administration) approved the use of Alexandrite lasers operating at 755nm. The Alexandrite laser wavelength matches the high absorption of melanin in follicular hairs, and allow for their removal without damaging the surrounding areas. Hair reduction of over 70% after a multiple treatment had been reported [131].

Q-switched Alexandrite lasers, Nd:YAG and ruby lasers have been approved and are commercially available for tattoo removal. In general, more than one laser might be used in combination for most effective results [132]. Alexandrite laser could be used to totally remove black/blue ink and also be used for totally removing green ink which Nd:YAG laser cannot use to remove effectively [132][133]. However, as

this wavelength range is well absorbed by melanin, care must be taken when using these lasers as they can cause damage to melanocytes, which can lead to transient hypopigmentation.

Lidar applications: Lasers are an important source for active remote detection and for the monitoring of atmospheric gases. The wavelength tuning range of a laser source is an important factor for lidar application, particularly for trace gas monitoring using differential absorption LIDAR (DIAL). Alexandrite offers wavelength with a tunability fundamental tuning range from 700-820nm, covering high absorption lines of both water vapor and oxygen. It has been used as a laser source for water-vapor measurement [134]. Alexandrite also has been used as a laser source for measurement of potassium density and temperature profile of the mesopause region based on D₁ line of potassium at 770nm [135].

4.6.2 Potential Applications

Airborne Lidar applications: In the past, Alexandrite lasers are mainly based on lamp pumping which makes Alexandrite lasers not suitable for airborne Lidar. However, the availability of high power laser diode sources, diode-pumped Alexandrite sources can be highly efficient and compact. This makes Alexandrite lasers potential alternative sources for Nd:YAG in airborne lidar applications. Currently, Q-switched Nd:YAG is the main laser source for lidar application. However, Nd:YAG lacks flexibility for wavelength tuning. Nd:YAG delivers a fixed wavelength at 1064nm and other wavelengths can be achieved through SHG (532nm), THG (355nm) or other OPO processes, which reduces the overall efficiency significantly. Alexandrite offers wavelength with a fundamental tuning range from 700-820nm, which covers the “red-edge” of vegetation [136]. This makes Alexandrite a suitable source for determining canopy heights. In addition, the blue/UV region of the spectrum, which is suitable for quantifying cloud/aerosol interaction, could be achieved in a single step via SHG.

Fluorescent Microscopy: Mode-locked Ti:Sapphire lasers have been sources for multiphoton fluorescent microscopy [137], providing a wide tuning range from 690nm -1050nm, with a pulse duration of ~50-100 fs. However, due to

the lack of appropriate laser diode pump sources, Ti:Sapphire usually requires a complicated pump source and set up, which makes the whole system become expensive. Alexandrite, which operates over a similar part of the spectrum, has the capability to be directly diode pumped. This leads to potential for low cost and highly efficient source, which makes Alexandrite lasers a potential alternative for these applications.

4.7 Conclusion

This chapter provided background knowledge of the Alexandrite laser. The first section described the crystal properties and the polarization dependent characteristics of Alexandrite. The energy level scheme, both 3-level (analogous system as ruby) and 4-level, was explained. This included the unique temperature dependent characteristics of Alexandrite, in which the emission cross section increases, while the lifetime decreases with increasing temperature. ESA, which is an important loss mechanism and also limits the tuning range of Alexandrite, was described.

The advantages and disadvantages of lamp pumping and diode pumping were described. The two techniques were compared, based on previous results in the literature. The main advantage of diode-pumping was the efficiency (\sim an order of magnitude higher than lamp pumping). The main thermal effect for diode pumped solid state lasers, especially for end pumping configurations, which is the thermal lensing was described analytically. Finally, the applications of Alexandrite were presented, showing the interesting potential of using Alexandrite laser as an alternative laser source in some applications.

5 Preliminary Design and Operation of Alexandrite Lasers

5.1 Introduction

This chapter aims to provide the foundations of Alexandrite laser operation with pumping by a high power red diode module. Firstly, the optical and spatial characteristics of the red diode module will be investigated. The optical beam delivery system will be described. Following that, the design of an optical mount for an Alexandrite rod which allows high thermal contact and avoids damage from thermal expansion will be presented. A compact laser cavity which yields high power ($>26\text{W}$) and high efficiency ($\sim 49\%$) will be described. The cavity will then be extended to obtain transverse single mode operation (TEM_{00}) using three cavity configurations: free-extended cavity, extended cavity with a spherical lens in the positive branches of the g-parameter, and cavity with spherical lens in the negative branches of the g-parameter. The laser output power, efficiency and the advantages and disadvantages of each cavity configuration will be described. In order to reduce the thermal load at the end of the crystal, the pump beam was split in half and each half used to pump at both ends of the Alexandrite crystal (double-end-pumping). In this section, the wavelength tunability of Alexandrite will be demonstrated using a self-seeding method. Finally, the performance of end-pumping will be compared with that of side pumping in bounce geometry which was conducted by colleagues in the same group.

5.2 Pump Laser Diode

Recently, high power red diode lasers have become commercially available. The diode used in this study is a diode laser module IS38.1, from DILAS, consisting of 7 diode mini bars that are optically-stacked in free-space producing an output with overall size $\sim 5 \times 5$ mm. The center wavelength is at ~ 638 nm with a bandwidth of <1.5 nm. The pump radiation is in the high absorption band of the Alexandrite crystal. The output power as a function of pump current is shown in Figure 5.1. In CW operation, the maximum output power of 66W CW could be delivered at 14A current and with water-cooling at a temperature of 16°C . Higher output power could be obtained at lower temperatures. Note that the pump module can deliver over 100W in Quasi-CW operation at a current of 20A. As the current increases, the effective diode temperature also increases, resulting in a shifting of the wavelength. Figure 5.1 shows the spectrum for three pumping levels. In all cases, the bandwidth was less than 1.5nm. The pump peak wavelength shifted by 0.3nm/A .

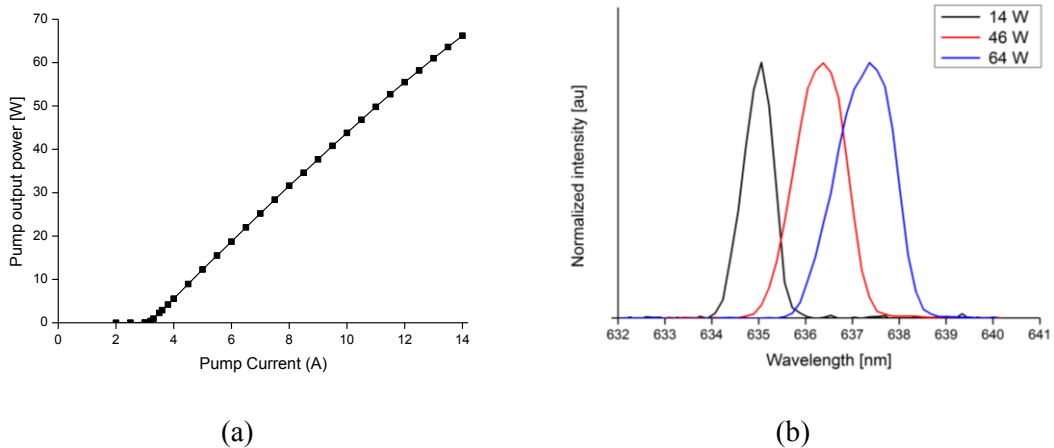


Figure 5.1: Optical pump characteristics in CW operation. (a) pump output power as current varies and (b) spectrum of laser diode bar at three different pump powers in CW operation.

One of the problems with end-pumping was with the optical delivery system for the diode radiation. The radiation from the diode consists of 7 bars separated by 0.8mm and the overall beam size is >5.0 mm square, as shown in Figure 5.2(a). The M-squared values were 265 and 23 for the horizontal and vertical direction,

respectively. By using two different cylindrical lenses, 30mm focal length in the horizontal direction and 250mm focal length in the vertical direction the quasi-circular shaped beam shown in Figure 5.2 (b) could be achieved. The beam width (FWHM) at the focal point in both the horizontal and vertical directions was $\sim 0.3\text{mm}$.



Figure 5.2: Laser diode beam profile (a) before optical shaping and (b) after optical shaping.

5.3 Alexandrite Laser Crystal

Two Alexandrite crystal rods from Northrop Grumman with 4mm diameter and 10mm length were used in this study. The crystals were AR coated at 755nm on both faces. The pump absorption coefficient of the 0.13% and 0.22% Cr^{3+} doped concentrations, tested using a He-Ne laser at 633nm, were 3.9 and 5.4cm^{-1} respectively. The optical mount for the laser rods was designed to achieve high thermal contact between the rods and the cooling system, as shown in

Figure 5.3. Water cooling was used in this system. The water was passed through the top and the bottom plates of the crystal to maintain a symmetric heat distribution in the crystal. A piece of indium foil was placed between the crystal rod and the holder to ensure high thermal contact. Four springs were used to attach the upper and lower parts of the holder together. These springs compressed the rod but reduced the risk of damage to the rod when thermal expansion occurred.

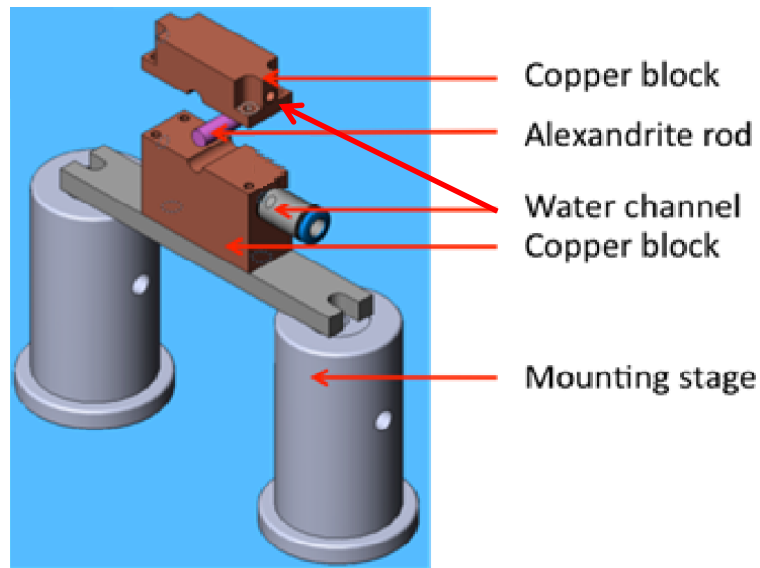


Figure 5.3: Optical mount for laser rod

5.4 Compact Laser Cavity

The first experiment was constructed using a compact cavity. The experimental setup is shown in Figure 5.4. This cavity configuration consists simply of two mirrors, a high reflectivity back mirror (BM) and an output coupler (OC) placed close to the Alexandrite crystal. This allows the generation of a high output power laser. In this section, laser cavity parameters such as OC reflectivity, lasing wavelength, beam quality and intracavity loss factor will be investigated.

The pump beam was shaped using a VCL of 250mm focal length and an HCL of 30mm focal length to obtain a circular shape with ~ 0.3 mm FWHM in both directions at the pump face of the crystal. Both VCL and HCL were AR coated at the pump wavelength of ~ 640 nm. The red diode pumped the Alexandrite rod through the back cavity mirror (BM). The back mirror has high transmission at the pump wavelength ($T > 95.0\%$) and high reflectivity ($R > 99.8\%$ at 755nm). The polarization of the laser diode was near-linear (95% purity) and parallel to the b-axis of the crystal. This resulted in absorption of the beam over the length of the crystal of 95% and 97% for 0.13 at. % doped and 0.22 at.% doped respectively. The

BM has high transmission at the pump wavelength (from 600-700nm) and has high reflection at the lasing wavelength (from 700– 800nm). Output couplers (OC) with reflectivities of 95%, 97%, 98%, and 99% at 755nm were investigated in the compact cavity. The cavity length was approximately 15mm and pumping by both CW and Quasi-CW operation of the pump laser was used.

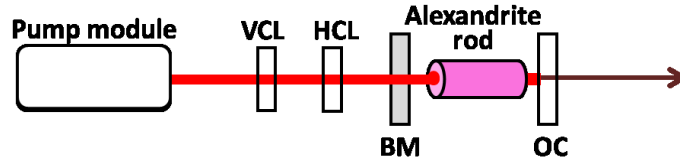


Figure 5.4: Schematic diagram of a compact cavity end pump system

5.4.1 CW Operation

Figure 5.5 shows the output power as a function of absorbed pump power for different OC reflectivities. For all of these results, the laser cavity was optimized at maximum pumping level. The graph shows the highest output power (~21W) was achieved with 99% OC reflectivity. The output power reduced at lower OC reflectivity. The lasing threshold increases for low OC reflectivity as expected, apart from at 99% OC reflectivity.

One of the factors impacting the slope efficiency is the output coupling efficiency (η_{oc}) which relates to the ratio of the useful loss (transmission of the OC) and total loss including the non-useful (intracavity loss), which can be described as [17],

$$\eta_{oc} = \frac{T_{oc}}{T + \delta} \quad \text{Eq. 5.1}$$

where T_{oc} is the transmission of the OC and δ is the intracavity loss where T and δ are assumed to be small. This output coupling efficiency is directly proportional to the laser slope efficiency [17]. However, Figure 5.5 shows that the slope efficiency decreases at lower OC reflectivities. The unexpected reduction in slope efficiency indicates that there is some inversion dependent loss which can come from energy transfer upconversion or pump excited state absorption. Pump excited state

absorption has been noted in Alexandrite [53][138] and we believe this to be the main responsible loss mechanism.

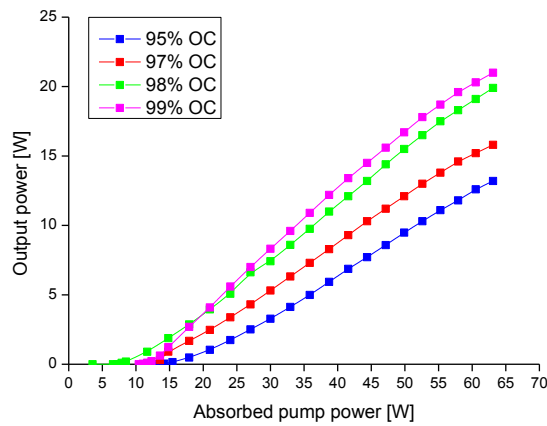


Figure 5.5: Output power as a function of absorbed pump power for different OC reflectivities.

In order to increase the laser efficiency, the pump beam size was reduced in the vertical direction using a VCL with a focal length 150mm. This produced a non-circular pump beam with FWHM of 0.2mm and 0.35mm in the vertical and horizontal direction respectively. Figure 5.6 shows the output power as a function of absorbed pump power for two different pump beam sizes. The results show that the smaller pump beam size increased the slope efficiency from 42% to 49%. The maximum power of 26.2W was achieved from 66.2W absorbed pump power.

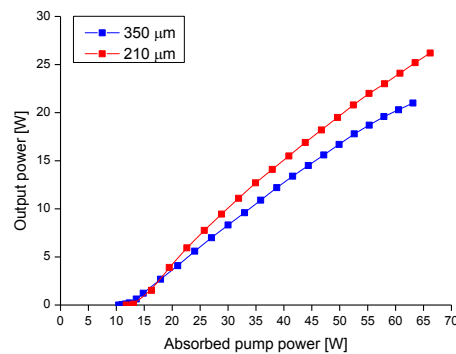


Figure 5.6: Output power as a function of absorbed pump power for circular pump beam size with FWHM of 0.35mm and fast-axis pump beam size reduced to 0.21mm.

Figure 5.7 shows the far-field intensity profile of the beam at 26.2W output power. Spatially, the beam is clearly multimode for both axes. The M-squared was measured using the ISO11146-1 method based on the second moment beam size. The M-squared of the laser was measured to be 22.4 and 16.0 in the horizontal and vertical directions respectively.

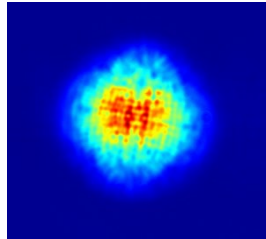


Figure 5.7: Spatial profile of the beam at 26.2W output power. The beam was highly multimode.

5.4.2 Quasi-CW Operation

In order to reduce the problems associated with heating and thermal lensing, running the laser in Quasi-CW was investigated. Figure 5.8 shows the output power at a diode pump duration of 1ms at 100Hz repetition rate (10% duty cycle) using 95% and 97% output reflectivity. For 97%OC reflectivity, an average output power of 15.8W was achieved from 6.4W pump power, with an average slope efficiency of $\sim 32\%$. The results shows no sign of turn-over and in fact, the slope efficiency increases. The final slope efficiency (measured from 3W to 6.4W) was 36%, which was 4% higher compared to 32% for CW operation using the same reflectivity OC.

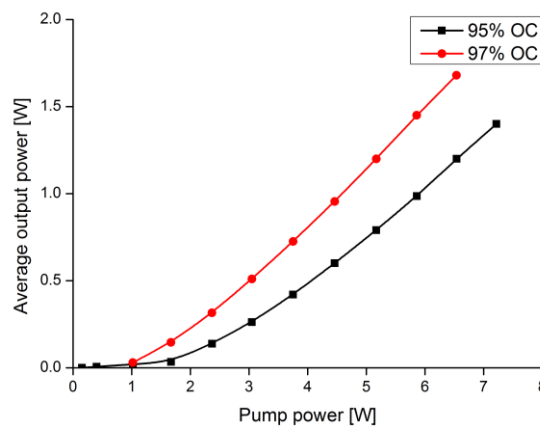


Figure 5.8: Average output power against pump power with 95% and 97% output coupler reflectivity.

5.4.3 Lasing Wavelength

Figure 5.9 (a) shows Alexandrite peak wavelength as a function of absorbed pumped power for the CW diode pumping case. As the pump power was increased, the lasing wavelength shifted by 0.12nm/W of pump power. This wavelength shift could be associated with the increasing temperature of the gain medium [139]. The lasing bandwidth (FWHM) of Alexandrite narrows from about 4nm at 20W pump power to 2.3nm near 60W, as shown in Figure 5.9 (b).

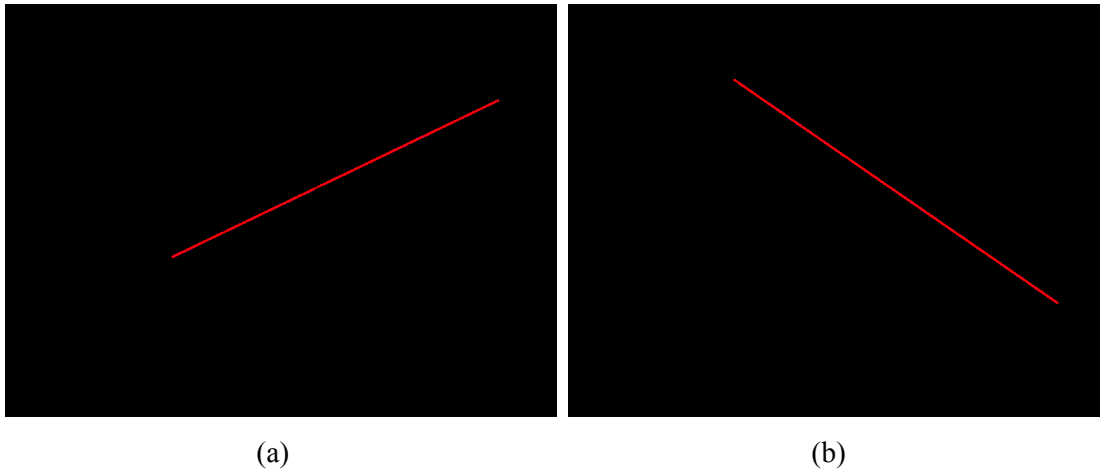


Figure 5.9: (a) Alexandrite lasing peak wavelength as a function of absorbed of pump power. (b) Lasing bandwidth FWHM of Alexandrite as a function of absorbed pump power.

5.4.4 Beam Quality

Figure 5.10 shows the M-squared spatial quality of the beam from the compact cavity as a function of absorbed CW pump power. As the absorbed pump power was increased, the M-squared in both horizontal and vertical direction increased. This degradation of the M-squared beam quality could due to the increased of thermal lensing, which proportional to the absorbed pump power. Thermal lensing did not only reduce the fundamental mode size in the gain medium, but increased aberrations. To obtain single mode operation, a different cavity configuration is required. Single mode operation will be discussed in the next section.

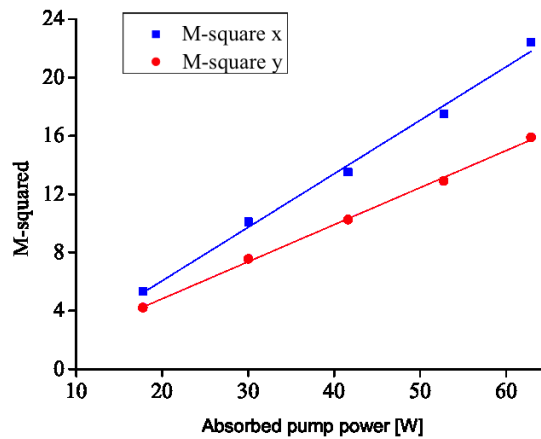


Figure 5.10: The M-squared of the output beam as current in the compact cavity varies.

5.4.5 Intracavity Loss

Internal loss in solid-state lasers in general is very small. However, for a low gain laser such as Alexandrite, intracavity losses can have a large effect on laser performance. Using a Findlay-Clay analysis, intracavity loss for a 4-level laser system can be described as [140],

$$P_{th} = P_0 \left[1 + \frac{\ln(1/R)}{L} \right] \quad \text{Eq. 5.2}$$

where P_{th} is threshold pump power, P_0 is pump threshold power for zero output coupling, R is the output coupler reflectivity and L is the total cavity round trip loss. The equation shows that the threshold pump power changes linearly with the natural log of the inverse of the reflectivity. Figure 5.11 shows the experimental threshold pump power at various OC reflectivities. The best linear fit to the experimental data was $y = 185.2x + 0.5$. According to the Eq. 5.2, the cavity round trip loss (L) calculated from the slope efficiency was estimated at 0.3 +/- 0.1%.

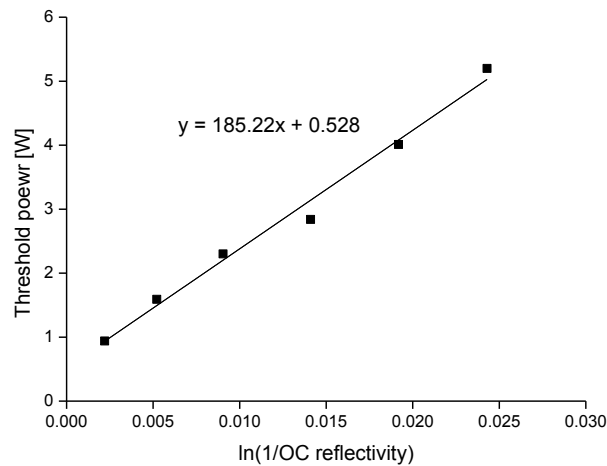


Figure 5.11: Threshold power versus natural log of the inverse of OC reflectivity.

5.5 Extended Cavity for Single Mode Operation

Single mode laser output is required for many applications. In this section, different cavity configurations are designed and investigated. This section starts simply with an extended compact cavity without an intracavity lens. This cavity has relatively high efficiency due to it having no insertion loss. This section is followed by investigating an extended cavity with spherical lens. The positions of the spherical lens and the cavity lengths are calculated to operate either in the positive region or negative region of cavity stability diagram.

5.5.1 Extended Compact Cavity

One way of obtaining single mode operation and still have high extraction efficiency is by extending the OC arm to increase the fundamental mode size in the crystal, as shown in Figure 5.12. M-squared beam quality as a function of cavity length at 40W pump power is shown in Figure 5.13. The M-squared decreased in both horizontal and vertical directions with increasing OC arm length.

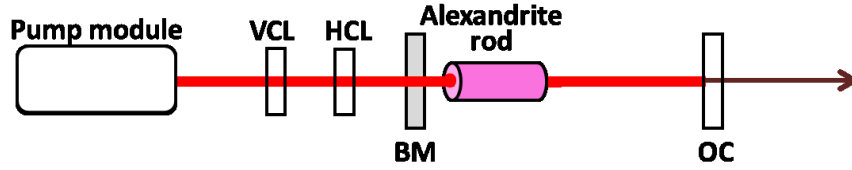


Figure 5.12: Schematic diagram of a compact cavity in single mode operation

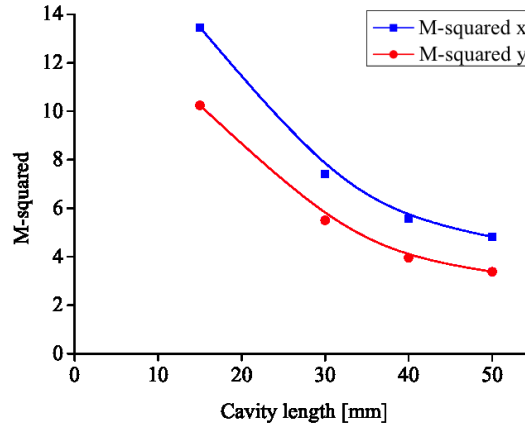


Figure 5.13: M-squared beam quality as a function of cavity length at 40W pump power.

In each cavity length, a near diffraction-limited beam can be obtained only in a small pump power range. Figure 5.14 (a) shows the beam (M -squared ~ 1.1) with an output power of 1.3W that was achieved using 5.5W pump power. This corresponds to an optical to optical efficiency of 23.6%. However, the ratio of the laser mode size (w_L) to the pump size (w_p) is high in this configuration and thus, the beam quality depends highly on thermal lensing. As the power increases, and thus the thermal lensing increases, the beam quality is degraded as shown in Figure 5.14 (b) for 15.5W pumping ($M_x^2 = 1.7$ $M_y^2 = 1.2$) and Figure 5.14 (c) for 18.7W pumping $M_x^2 = 2.4$ $M_y^2 = 1.7$.

In addition, the thermal lensing also limits the cavity stability region. That is, if the cavity length was longer than the focal length of thermal lensing, the cavity became unstable and lasing was observed to cease.

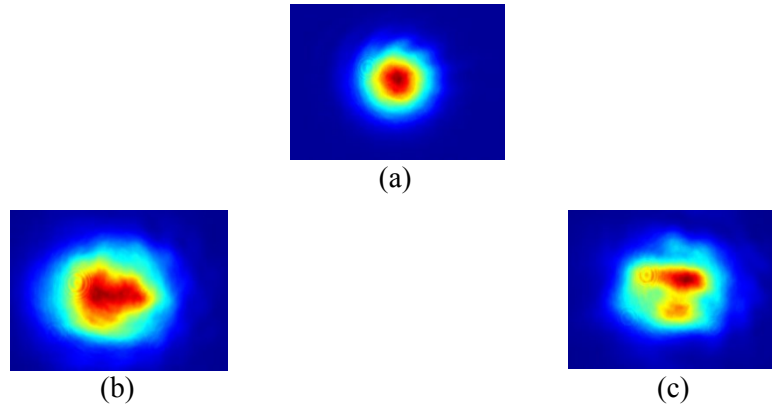


Figure 5.14: Beam profile using a compact cavity for (a) 5.5W pumping (b) 15.5W pumping (c) 18.7W pump power.

5.5.2 Extended Cavity with Internal Spherical Lens

A different cavity configuration was designed to achieve single mode output with high power in QCW or CW operation. The experimental set up is shown in Figure 5.15. The spherical lens (SPL) was placed near the output coupler (OC).

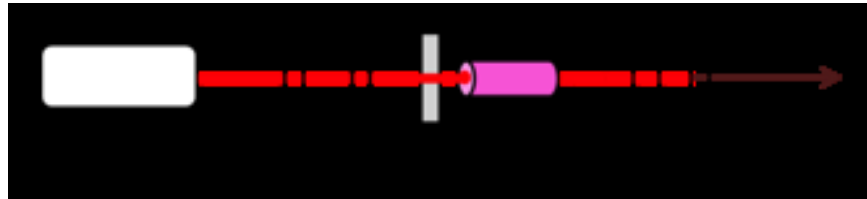


Figure 5.15: Extended cavity with internal spherical lens using positive region of the g-parameter stability diagram.

The combination of the SPL and OC ($R = 95\%$) act as a spherical curved mirror OC with a radius of curvature (R_2) equal to the focal length of the lens. The crystal was placed close to the BM therefore, as the pump power increased, the back mirror acted as if it was a curved mirror with a radius of curvature (R_1), which was proportional to the thermal lens. The g-parameter discussed in section 1.4.3 can be reduced to,

$$g_1 = 1 - \frac{L}{R_1} \quad \text{and} \quad g_2 = 1 - \frac{L}{R_2} \quad \text{Eq. 5.3}$$

and the stability condition can be written as [55] ,

$$0 < g_1 g_2 < 1$$

Eq. 5.4

The cavity stability can be described using the stability diagram which is a plot of the g_1 and g_2 plane, as shown in Figure 5.16 where the blue area represents the stable region.

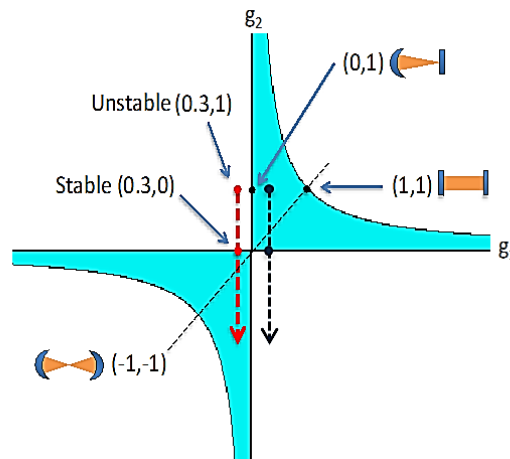


Figure 5.16: Stability diagram and mode profiles. The blue area represents the stable region.

5.5.2.1 Positive region of g-parameter

In this configuration, the spherical lens focal length and cavity length were chosen to yield positive values of both g_1 and g_2 . In this configuration, the total cavity length was 145mm. A spherical lens of focal length 200mm was placed at 130mm away from the BM. This gives a constant g_1 of ~ 0.3 . Without pumping, as there was no thermal lens, g_2 was equal to 1. As the pump power increased, and thus the thermal lensing increased, the resonator moved along a straight line as shown by the blue arrow in Figure 5.16. Figure 5.17 shows the average output power as pump power was varied. Pumping at 1ms pulse duration at 100Hz repetition rate (10% duty cycle), an average output power of 0.74W was obtained from 6.68W absorbed pump power. This corresponds to 11.1% optical to optical efficiency, compared to 18.5% in the compact cavity. The laser efficiency in this configuration was lower than the extended cavity with no lens due to the smaller laser mode spot size and intracavity loss from the spherical lens. The M-squared at 0.74W average output power was 1.6 in the horizontal direction and 1.3 in the vertical direction.

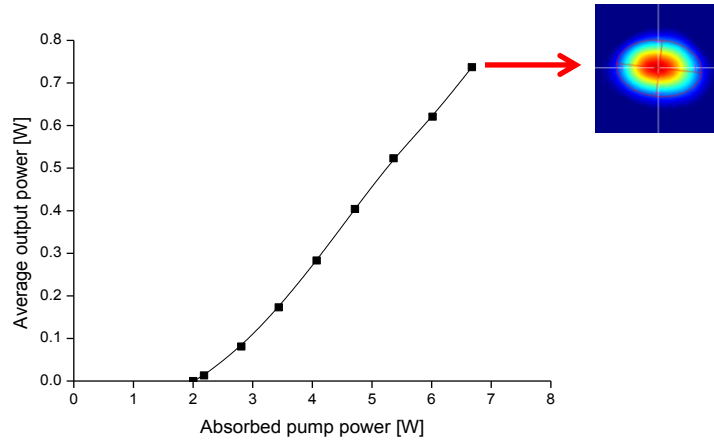


Figure 5.17: Average output power as a function of absorbed pump power.

As shown in Figure 5.16, when the pump power increases, the cavity moves along the blue line and finally out of the stability zone. Figure 5.18 shows the spatial profile after the cavity become unstable. It was observed that the cavity became unstable in both horizontal and vertical directions at the same point. The cavity became unstable at an absorbed of pump power ~ 22 W.

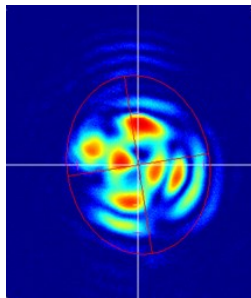


Figure 5.18: Spatial profile of the unstable resonator with pump power of at ~ 22 W.

5.5.2.2 Negative region of g-parameter

The negative branch of the g-parameter utilizes the presence of thermal lensing to operate in the stable region. This cavity has the advantage over the positive branch as it can operate with higher thermal lensing. However, the disadvantage of this configuration was the presence of an intracavity focal point. This could lead to a potential damage of optical components or air breakdown [17]. However, at the peak powers used in this experiment, this problem could be neglected [141]. The cavity stability can be described using the stability diagram which is a plot of the g_1 and g_2 plane, as shown in Figure 5.16. In this configuration, the total cavity length

was 200mm. A spherical lens of focal length 150mm was placed at 182mm away from the BM. This gives a constant g_1 of ~ -0.3 as shown by the red dotted line in Figure 5.16. The cavity initially operated in the unstable region. As the pump power increased, and thus the thermal lensing increased, the resonator moved along a straight line as shown by the red arrow. Above a certain thermal lensing power the g_2 parameter become negative too, and the product of g_1 and g_2 became positive and moved into the stable region.

Moreover, this cavity has a significantly smaller fundamental laser mode size in the laser rod compared to the positive g -parameter region (less than half the size from a calculation by Magni) [55]. This also reduces the degradation due to the thermal lens. However, smaller spot size reduces the extraction efficiency of the laser. The cavity length was optimized to 220mm, when using a spherical lens with focal length of 150mm placed at 180mm from the BM. An average power of 4.1W was obtained using 47W pump power with 1ms pulse duration at 800Hz repetition rate (80% duty cycle). This corresponded to an optical to optical efficiency of 8.7%. The spatial profile is shown in Figure 5.19. The output beam was single mode, with $M_x^2=1.2$ and $M_y^2=1.4$. Therefore, operating with negative g_1 and g_2 , with the appropriate focal length lens provided a promising cavity configuration for TEM₀₀ with high output power, high repetition rate Quasi-CW or CW operation.

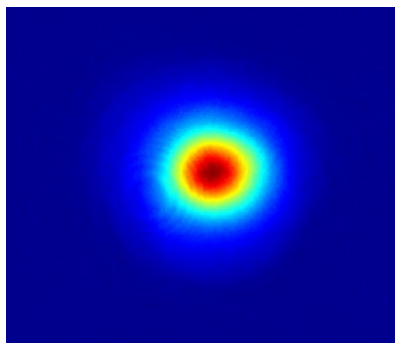


Figure 5.19: Beam profile at 4.1W average output power

5.5.3 Double-End-Pumping

One of the main problems of end pumping is thermal lensing. Not only does it degrade the beam quality but also reduces the efficiency of the laser. Moreover,

power scaling is more challenging as the excited state absorption at the pump wavelength in Alexandrite is high, the same order of magnitude as the ground state absorption [53]. The high absorption of the pump energy is turned into heat. Double-end-pumping can improve thermal lensing by distributing the inversion between the two rod ends and the heat is deposited on both sides of the crystal. Double-end-pumping has been proven to improve thermal lensing, allowing higher pump power, and thus increasing output power [142].

Figure 5.20 shows the schematic diagram of a compact cavity with double end pumping. High reflectivity mirror 1 (HR1) reflected half of the pump beam horizontally to HR4. The rest of the beam was reflected by HR2 onto HR3. By cutting the pump beam in half, the M^2_x improved from $M^2_x = 265$ to $M^2_x = 122$ on path A and to $M^2_x = 171$ on path B. There was no significant difference of M^2_y . By using a VCL with 150mm focal length and an HCL 30mm with focal length, the focused pump beam spot size (FWHM) was $\sim 0.2\text{mm}$. For double-end-pumping, the Alexandrite laser cavity was folded into an L-shape with a 45 degree dichroic mirror (DM) to allow pumping from both sides and separate the laser output. The back mirror (BM) and the dichroic mirror (DM) were placed as close as possible to the end of the rod. The DM has high reflectivity at 755nm, and high transmission at 636nm at 45 degrees angle of incidence. The total cavity length for the folded compact cavity using double end pumping was 33mm.

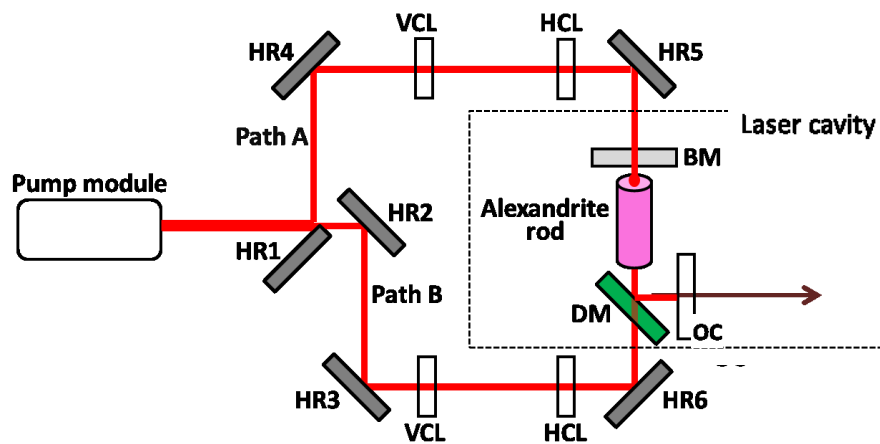


Figure 5.20: Schematic diagram of the folded compact cavity with double end pumping.

Figure 5.21 shows the output power as a function of absorbed pump power for (a) CW operation with single end pumping (pumped by path A only) and double end pumping using the same cavity configuration. Comparing the two pumping systems, double end pumping shows lower threshold pump power and higher slope efficiency ($\sim 32\%$ and $\sim 26\%$ for double end pumping and single end pumping, respectively). For CW operation, the output power of 3.5W at the absorbed pump power of 19.7W was achieved with a single end pumping. The output power of 8.4W was achieved at 32.6W pumping with double-end-pumping. The output power was limited by cavity stability due to thermal lensing. Therefore, as expected, double end pumping allowed a higher pumping level before approaching the unstable region.

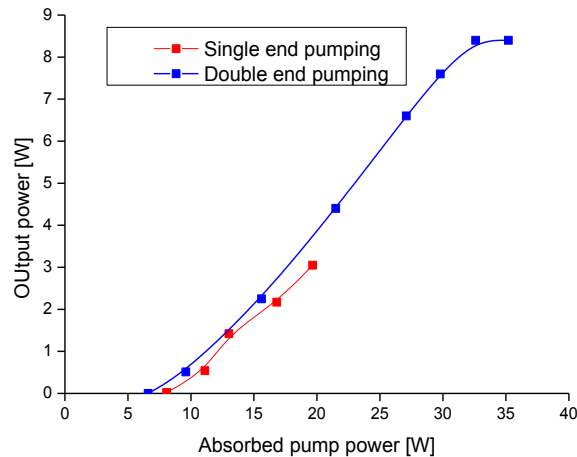


Figure 5.21: CW output power as a function of absorbed pump power for single and double end pumping. The pump power in both single and double end pumping was limited by the cavity stability.

5.6 Spectral Properties of Alexandrite

Figure 5.22 shows the spectrum of an Alexandrite laser that is commonly observed in different alignments of a compact cavity using the same pump power level. Figure 5.22 (a) shows the spectrum of an Alexandrite laser with an optical bandwidth (FWHM) of $\sim 3\text{nm}$. By slightly misaligning the laser cavity, optical

filtering effects with free spectral ranges of $\sim 1\text{nm}$ and $\sim 5\text{nm}$ were observed, as shown in Figure 5.22 (b) and (c). The spectral properties of Alexandrite will be studied further in chapter 6.2.

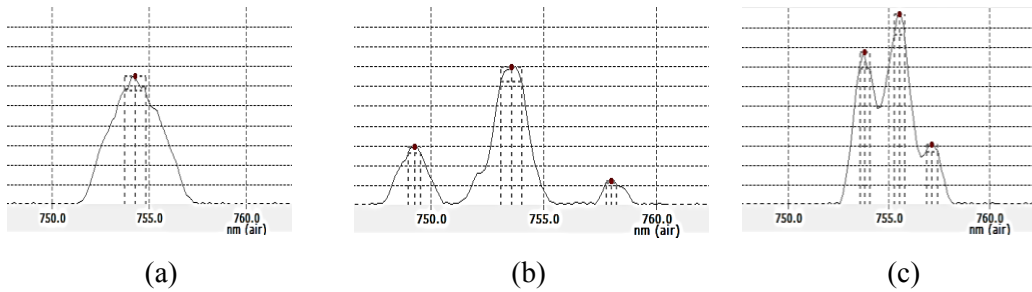


Figure 5.22: Spectrum of the laser in a compact cavity with alignments that give (a) no filtering effect, (b) filtering effect with free spectral range of $\sim 5\text{nm}$, (c) filtering effect with the free spectral range of $\sim 1\text{nm}$.

5.6.1 Wavelength Tuning

There are various methods for wavelength control of tunable lasers. A common method of wavelength tuning is using a birefringent filter (BIFI) or prism inside the resonator as a tuning element [143][144]. Injection seeding has also been demonstrated to be a very effective method of wavelength control in Alexandrite lasers [145].

In this study, Alexandrite wavelength tuning was achieved by self-seeding from outside the main cavity, using an 1800 lines/mm holographic grating in a Littrow configuration. The experimental system is shown in Figure 5.23. Retro-reflected 1st order output self-seeds the main cavity thereby tuning the laser wavelength.

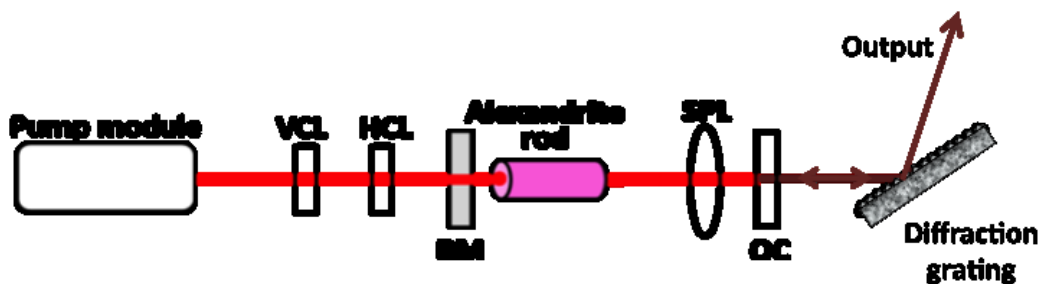


Figure 5.23: Alexandrite TEM_{00} laser design for wavelength tuning.

Figure 5.24 shows the output power as wavelength was tuned between ~ 730 - 799 nm. The Alexandrite could be tuned smoothly from 730 nm to 799 nm. The output power was maximum at ~ 760 nm.

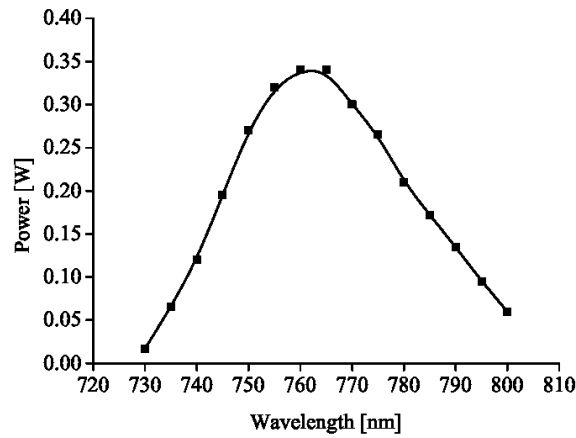


Figure 5.24: Tuning curve of Alexandrite laser

Figure 5.25 shows the spectrum of the tuned Alexandrite laser for (a) 730 nm and (b) 755 nm. The spectral bandwidth was narrower than 1 nm, with the measurement of bandwidth being limited by the resolution of the spectrometer. Figure 5.25 (c) shows the spectrum at 800 nm. The maximum tunable wavelength was limited to ~ 800 nm in this demonstration as the transition at 755 nm was not sufficiently suppressed in the main cavity.

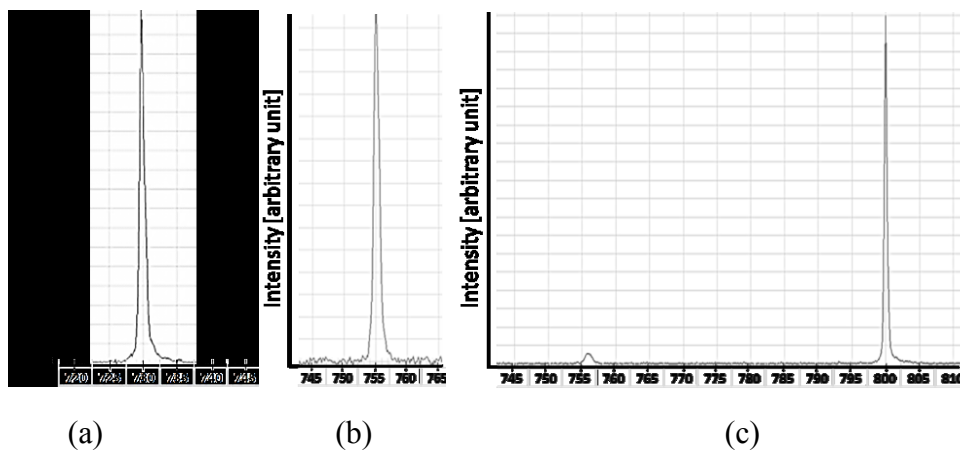


Figure 5.25: Spectrum of Alexandrite laser wavelength tuning using self-seeding method.
 (a) Peak wavelength at 730 nm (b) Peak wavelength at 755 nm (c) Peak wavelength at 800 nm.

5.7 Comparison to Side Pumping in a Bounce Geometry

Geometry

In our group, side pumping in a bounce geometry configuration has also been studied. The main advantages of side pumping are the simpler diode pump delivery and the higher pump volume which leads to a potential reduction in the effects of thermal load on the crystal. Therefore, side pumping is more appropriate for power scaling. In a bounce geometry, the laser experiences total internal reflection at the pump face of the crystal at a grazing incidence angle. Figure 5.26 shows the experimental setup for side pumping in bounce geometry configuration. The VCL has a focal length of 80mm. The back mirror (BM) and output coupler (OC) (97% reflectivity) were placed close to the crystal. This geometry is, in general, used in high absorption cross section gain media, such as Nd:YVO₄, [48][62]. Alexandrite, however, has relatively low ground state absorption cross section, $\sim 0.5 \times 10^{-19} \text{ cm}^2$, compared to $\sim 6 \times 10^{-19}$ for Nd:YVO₄ [146][53]. As shown in Figure 5.26, some of the pump energy is deposited outside the lasing region. This leads to lower efficiency when compared to end pumping.

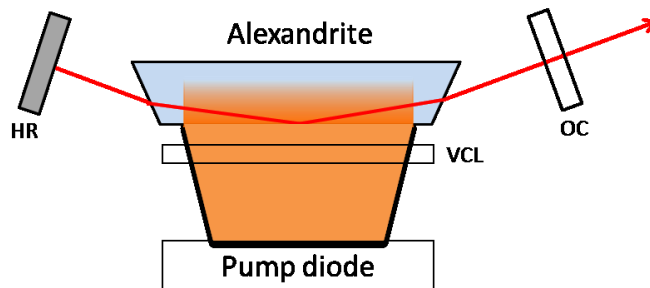


Figure 5.26: Side pumping in a compact cavity in a bounce geometry configuration.

Figure 5.27 shows the output power as a function of absorbed pump power for side pumping in the bounce geometry. The output power as a function of absorbed pump power for the compact end pumping geometry of section 5.3 with the same OC reflectivity ($R = 97\%$) is also plotted for comparison. The lasing threshold for side pumping was over 2 times higher than for end pumping. The slope efficiency was 32% for end pumping and 26% for side pumping. Lower threshold and higher efficiency were achieved in end pumping as expected due to high pump power

density and high pump laser mode spatial overlap. Note that both cavity configurations have specific advantages and disadvantages. However, for this pumping level, end pumping was superior in both pumping threshold and laser efficiency.

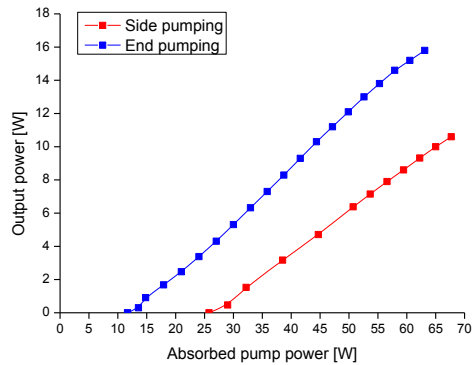


Figure 5.27: Output power as a function of absorbed pump power for side pumping in a bounce geometry configuration and end pumping case for comparison.

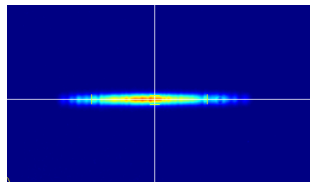


Figure 5.28: Spatial profile at 57W pump power for the bounce geometry.

Figure 5.28 shows the spatial profile at 57W absorbed pump power for the bounce geometry. The beam is highly multimode in horizontal direction. This is due to the nature of bounce geometry configuration, in which the small gain profile in the vertical direction is well matched with the fundamental mode. However, in the horizontal direction, the gain is much larger than the fundamental mode, allowing higher order transverse modes to oscillate.

5.8 Conclusion

This chapter firstly introduced a pump laser diode module for Alexandrite laser. The laser diode produces output power of over 60W at 638nm. The Alexandrite crystal rod holder was designed to allow good thermal contact and reduce risk of damage when thermal expansion occurs. High output power and high efficiency were achieved in the compact cavity. The compact cavity was investigated using different OC reflectivities. The highest output power of 26.2W with slope efficiency of 49% was achieved from 66.2W absorbed pump power using a 99% OC. The results show that lower OC reflectivity tends to have higher threshold and lower slope efficiency. It is believed that the unexpected decrease in slope efficiency indicates some inversion dependent loss mechanism, which is believed to be pump excited state absorption.

In order to obtain single mode (TEM_{00}) operation, three extended cavity designs were proposed and investigated. Firstly, by simply extending the length of the compact cavity, a single mode output power of 1.3W was obtained from 5.5W absorbed pump power, corresponding to 23.6% efficiency. However, the beam quality degraded as the pump power increased. Secondly, the extended cavity with internal spherical lens using the positive branch of the g-parameters was set up using QCW pumping (10% duty cycle). An output power of 0.74W was obtained from 6.68W pump power (11.1 % efficiency). At increasing pump power, again, the cavity became unstable. Lastly, the extended cavity with internal spherical lens using the negative branch was investigated. This configuration was designed to operate stably in high power operation. In this study, an average power of 4.1W was obtained using 47W pump power (8.7% efficiency). Later, double-end-pumping was investigated. Splitting the pump beam into half to pump both sides of the crystal not only improved thermal effects, but also improved the horizontal pump beam quality by a factor of two. This resulted in a lower threshold and higher slope efficiency.

Wavelength tuning was also demonstrated using a self-injection seeding method with an external grating in the Littrow configuration. The wavelength could be tuned smoothly from ~730nm to ~799nm.

Finally, the operation of the end-pumped configuration was compared with side pumping in a bounce geometry configuration. Side pumping has the advantage of higher pump volume and thus, reduces the thermal load in the crystal. However, in Alexandrite, end pumping is shown to provide higher efficiency and better beam quality.

6 Enhanced Alexandrite Laser Towards Remote Sensing Application

6.1 Introduction

Remote sensing is an essential tool for remote detection and for the monitoring of atmospheric gases and has led to an improved understanding of physical and chemical processes in the atmosphere. There are two types of remote sensing: passive remote sensing and active remote sensing. Passive remote sensing is more commonly used as it relies on the energy that is naturally available, the most obvious example being the radiation transmitted from the sun. Passive remote sensing requires only a receiver instrument to detect either reflected or emitted energy from the observed scene. However, for passive remote sensing based on reflection of the sun's radiation, detection can only take place during the daytime. In contrast, active remote sensing relies on its own transmitter. The transmitter sends pulses of energy to the observed scene and a receiver detects the reflected or backscattered signals. Active remote sensing offers multiple advantages over passive remote sensing such as the ability to measure regardless of the time of day i.e. day or night. Also active remote sensing offers the ability to measure distances to observed scenes. For example, by using pulsed light sources, such as pulsed lasers, to measure differences in the arrival times of reflected pulses of light from a scene. As a result, active remote sensing has proved to be an invaluable technique for ground, airborne and satellite based measurements [147].

The most common type of active remote sensing that includes the ability to measure distances is referred to as *lidar*, a word that is a fusion of *radar* and *light*. In general, when pulsed lasers are used in lidar instruments as transmitters they are

required to have high pulse energies and high peak powers to overcome signal attenuation and background noise. Also to provide good spatial and temporal resolution, they are required to have good beam quality and to generate short pulses. Finally for speed higher repetition rates are desirable but this will be limited by the temporal resolution requirements.

Currently an exciting field for the application of lidar for satellite based measurements, for example, to monitor the weather[148], [149]. A particular challenge for satellite-based lidar has been the designing of compact and cost effective instruments that are efficient and that offer long-term stability in their performance are crucial [150]. Finally they will need to withstand the harsh environment of space.

A common type of laser used for satellite based lidar measurements that has been developed over the laser few decades is based on the Q-switched Nd:YAG laser [150][151], [152][153]. For lidar applications Nd:YAG lasers have been designed to achieve pulse durations ranging from ~ 1 -100ns with repetition rates ranging from ~ 1 Hz to > 1 KHz and with pulse energies ranging from ~ 1 to >100 mJ [153]–[156][157][158]

Recently our group has focused on Alexandrite as a gain medium because it has a number of intrinsic properties that mean that in some instances it can offer superior performance compared to Nd:YAG based pulsed lasers. In particular, Alexandrite has a higher thermal conductivity (~ 2 times higher than Nd:YAG) and a higher fracture limit (~ 5 times higher than Nd:YAG)[15] which means it can potentially be used to make a more efficient high power laser. Also, Alexandrite offers more flexible wavelength tunability in the near IR region and it is more efficient than Nd:YAG based lasers at generating high power in the UV region. This latter point is due to the fact that its UV light can be generated by a single second harmonic generation (SHG) step rather than through third harmonic generation (THG) or other optical parametric oscillator (OPO) processes for Nd:YAG.

The aim of this chapter is to develop Q-switch Alexandrite lasers towards the requirements of satellite-based remote sensing applications. Specifically this work is motivated by ESA's need for lasers suitable for altimetry and backscatter lidar

applications. For altimetry lidar they require high repetition rate (\sim KHz) and short pulse duration (\sim ns) lasers while for backscatter lidar they require low repetition rate (\sim Hz) and high pulse energy (\sim 10mJ) lasers. This chapter focusses on backscatter lidar requirements but future work could easily extend this system to altimetry applications and this is discussed in chapter 7.

The first part of this chapter focuses on optimising the laser efficiency (further from chapter 5). To do this, the pump beam quality is improved and a high temperature oven for the Alexandrite crystal is implemented. The characteristics of the Alexandrite laser as a function of temperature (up to 150 °C) is studied in CW and short pump pulse operation. It is noted that the oven was designed and built by other colleagues in the group but its operation and Alexandrite characteristics was performed by the author. The second part of this chapter is to demonstrate Alexandrite laser performance in a Q-switching operation. Different cavity designs are presented. Each design has its advantages and disadvantages, which could be optimised for suitable remote sensing applications. Some important parameters for remote sensing applications such as pulse energy, efficiency and pulse duration will be investigated. Before finishing the chapter, the efficiency of second harmonic generation of Alexandrite laser to deep blue and UV region is demonstrated.

6.2 Diode Pumped Beam Shaping

One of the main difficulties for achieving efficient end pumping is having a very different beam quality factor in two orthogonal planes of the pump module. The pump module used in this system has an M-squared of 265 \pm 3 and 23 \pm 1 for the horizontal and vertical directions respectively. This makes it particularly difficult to focus down to a small spot size with a long Rayleigh length in the horizontal direction. Several techniques have been proposed to solve this problem [129], [159], [160]. However, these result in a loss in efficiency or require a complicated design.

In this work, we used a simple beam shaping technique to improve the M_x^2 . A schematic diagram from the top view of the pump beam shaping arrangement is shown in Figure 6.1. All of the mirrors, M1-M4, are highly reflective at the pump

wavelength. Mirror M1 splits half of the pump beam in the horizontal direction and sends it to M3. The other half of the beam is incident upon M2. Mirror M2 then reflects the beam to M4 which is lower than M3. Mirror M4 then reflects the beam in the same direction as the beam from mirror M3 but lies below it. This setup improves the beam quality in the horizontal direction, the M-squared value drops from 265 ± 3 to 162 ± 2 . However, as the beams stack on top of each other, the M-squared in a vertical direction increases from 23 ± 1 to 53 ± 1 . The M-squared ratio of horizontal and vertical direction is therefore redistributed. Its ratio is improved from $>10:1$ to approximately $3:1$.

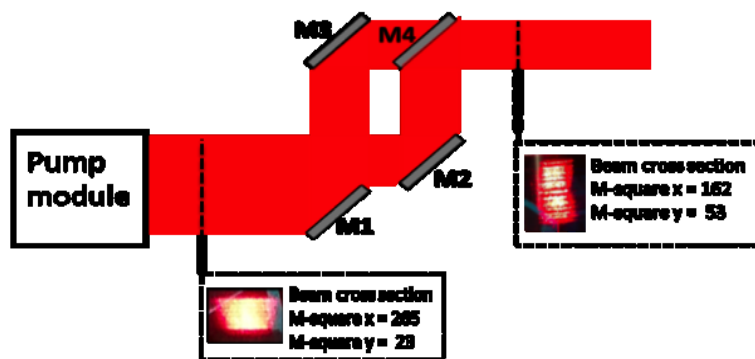


Figure 6.1: Schematic diagram of a pump beam shaper (top view).

The improved pump beam was then focussed with a vertical cylindrical lens (VCL) of focal length 150mm followed by a horizontal cylindrical lens (HCL) of 50mm to produce a focussed beam that was approximately circular in shape. The beam spot size in the horizontal direction had a FWHM of 0.27mm and in the vertical direction had a FWHM of 0.20mm. The beam Rayleigh lengths were 2.1mm and 4.1mm in the horizontal and vertical directions respectively.

6.3 High Temperature Alexandrite Crystal Operation

6.3.1 Temperature Control Oven

As mention in section 4.3.2, the laser properties of Alexandrite such as upper state lifetime and gain cross-section are temperature dependent. To investigate and attempt to enhance the laser output and efficiency of Alexandrite laser, a high temperature oven was designed and constructed. Figure 6.2 shows the design of the high temperature which was based on a thermal electric cooler (TEC). The Alexandrite crystal (0.22% doped) was sandwiched between two aluminium blocks. The TEC was placed under the bottom of the aluminium block to control the temperature (heating or cooling), using a feedback from a temperature sensor, which was placed inside the bottom aluminium plate. The other side of the TEC was connected to a copper the heat sink which had a cavity inside to allow cooling with a circulating water system. The water temperature was kept at 30°C. The heat from the oven was removed by the TEC by the Peltier effect. The temperature could be controlled from ~20°C up to 130°C without the laser running. However when the laser was running the controllable temperature was allowed to be as high as 150°C because of the heat generated in the crystal i.e. the quantum defect and other non-radiative decay processes. As the TEC was at the bottom of the oven, it created a temperature difference between the top and bottom of the aluminium plates on the order of a few degrees.

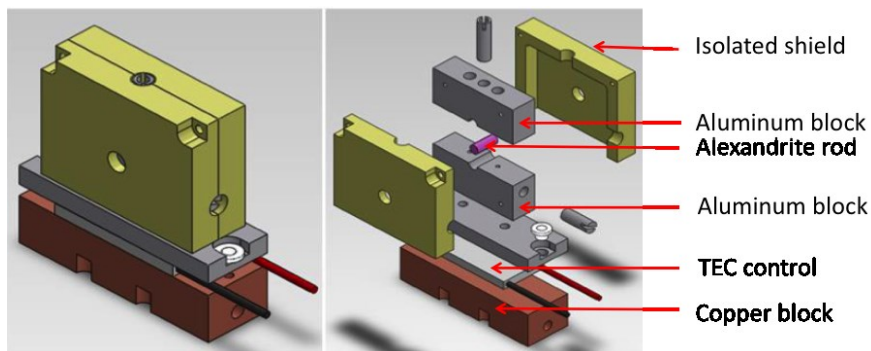


Figure 6.2: Temperature control oven [161]

6.3.2 Laser Performance

A compact laser cavity set up is shown in Figure 6.3. The 0.22 at. % doped Alexandrite rod ($L=10\text{mm}$, $\phi = 4\text{mm}$) was operated in the temperature controlled oven. The back mirror (BM) and the output coupler (OC) were placed in close proximity to the oven (width of oven = 20mm). The cavity was 27mm. This was slightly longer than the compact cavity in chapter 5 due the size of the oven. A vertical cylindrical lens with a focal length of 150mm and horizontal cylindrical lens with a focal length of 50mm were used to create a pump-beam spot size of 0.27mm and 0.20mm at the crystal in the horizontal and vertical directions respectively. The output coupler reflectivity was 95%.

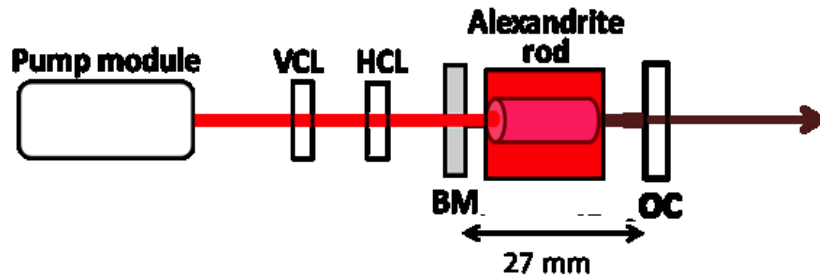


Figure 6.3: Schematic diagram of compact cavity in a high temperature oven

6.3.2.1 CW operation

The Alexandrite laser properties as a function of temperature were first investigated in CW operation. Figure 6.4 shows the lasing threshold pump power as a function of crystal holder temperature in the range of 20°C to 150°C. The lasing threshold pump power had a minimum value at ~60°C. At a lower and higher temperature, the threshold pump power increases. The minimum threshold at ~60 °C indicated that the laser has the highest gain at this temperature.

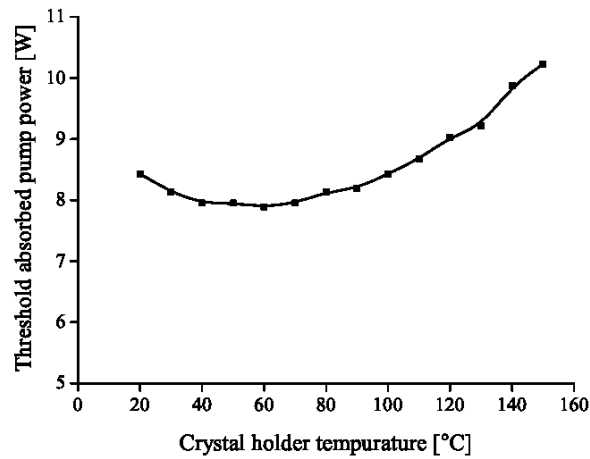


Figure 6.4: Threshold absorbed pump power as a function of crystal holder temperature.

Figure 6.5 (a) shows the output power as a function of temperature at 22W pump power. The result shows the output power reduced dramatically as temperature increases across the range. To investigate the decreasing of output power further, the output powers as a function of the absorbed pump power at few different temperatures were measured, as shown in Figure 6.5 (b). The graph shows the output power increases with absorbed pump power and has a roll over at high absorbed pump power for the higher temperature. The slope efficiency, measured at the straight part of the curve from the threshold to ~ 22 W absorbed pump power, was 29% (at 30°C), 25% (at 60°C), 19% (at 100°) and 10% at 150°C. The slope efficiency decreased by a factor of almost three fold as the temperature was increased from 30°C to 150°C. This indicated that there was some loss that increases as increasing temperature. The roll-over of the output power was mainly due to the thermal lensing at high pump power which moved the resonator to an unstable region. It was noted that the roll over tends to occur at lower absorbed pump power at higher temperature. This could come from an increased excited state absorption (ESA) with temperature [162][54]. Another contributing factor could be an increase in the quantum defect because a shift in the centre wavelength occurred at the same time (see Figure 6.7).

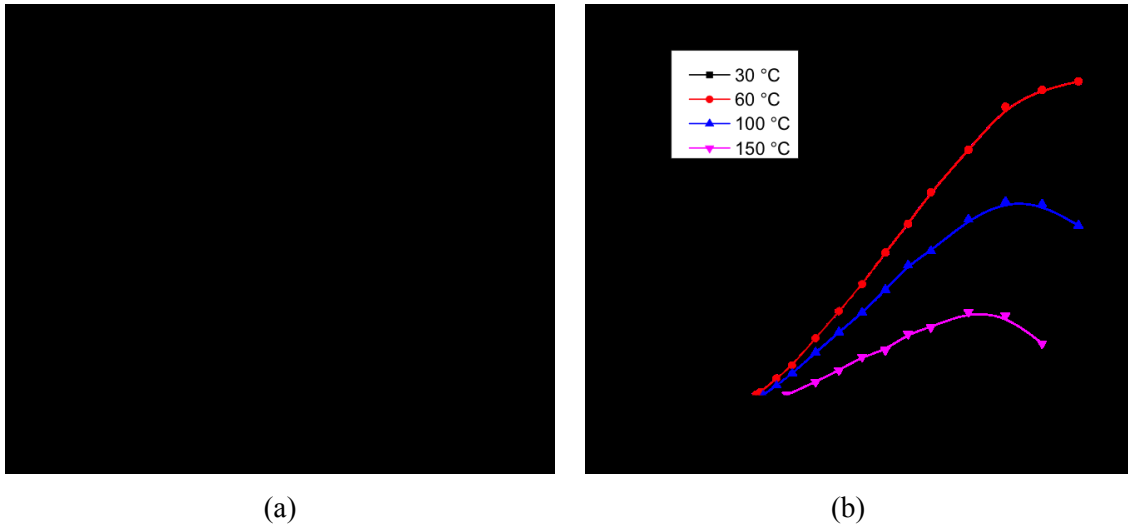


Figure 6.5: (a) Output power as a function of crystal holder (i.e. the oven) temperature for 22W CW pump power. (b) Output power as a function of absorbed pump power.

Figure 6.6 shows an example of a spectrum of the laser output. In general, the spectrum contains two or more narrow peaks ($<1\text{nm}$ FWHM) with a separation of $\sim 4\text{nm}$ to $\sim 5\text{nm}$. In this study, the peak wavelength was defined as the wavelength with highest intensity, which was point B in Figure 6.6.

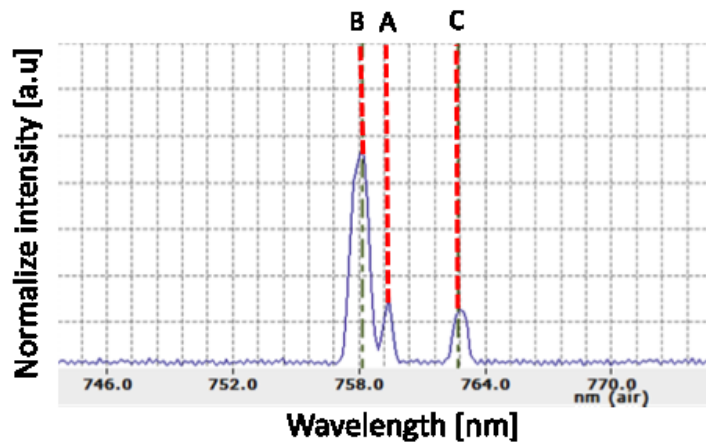


Figure 6.6: Spectrum of the Alexandrite laser output. The spectrum contains three peaks marked A, B and C.

Figure 6.7 shows spectrum of lasing output wavelength as a function of temperature for three values of pump power. The wavelength shifted discretely towards longer wavelength as temperature increased. The wavelength increased from $\sim 750\text{nm}$ to $\sim 762\text{nm}$ for 3W Quasi-CW pump power and from $\sim 752\text{nm}$ to $\sim 772\text{nm}$ for 22W CW

pump power and ~758nm to ~772nm for 31W CW pump power. Comparing between 3W of Quasi-CW pump power and 31W of CW pump power, at the same crystal oven temperature, there was a difference in peak wavelength of ~10nm. This indicated the temperature at the centre of the rod was approximately 100°C higher than crystal the oven temperature for the CW pump power.

Figure 6.7 shows that the wavelength increased discretely like a staircase with a “jump” of ~4nm to ~5nm. In fact, the wavelength did not “jump” spontaneously. As increasing temperature, the longer wavelength peaks became stronger and finally dominate the other one. The spectral feature can be explained by the nature of the birefringence of Alexandrite. This creates an optical filtering with a free spectral range (FSR) given by [163],

$$FSR = \frac{\lambda_0^2}{\Delta n L} \quad \text{Eq .6.1}$$

Where λ_0 is the centre wavelength, Δn is the difference between the refractive index of the two crystallographic axes and L is the round trip length of the Alexandrite crystal ($L = 20\text{mm}$). Using the refractive index of b and c axis of the crystal around 750nm ($n_b = 1.742$, $n_c = 1.735$) [115], the calculated FSR was ~4.0nm. As λ_0 increases at higher temperature, the FSR also increases. It is noted that within the certain range of temperature, the wavelength peak tends to move continuously to shorter wavelength. This results from the temperature dependent refractive index ($d\Delta n/dT$) of the crystal, which was ~ -0.07nm.K⁻¹.

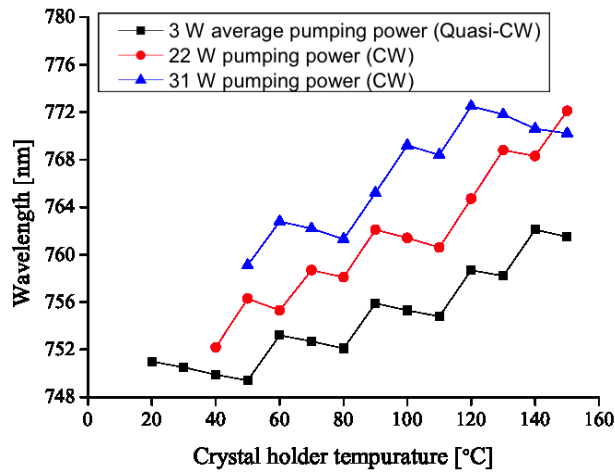


Figure 6.7: Wavelength of Alexandrite laser as a function of oven temperature for 3W average pump power for quasi CW (with pump pulse duration of 2ms at a repetition rate of 2Hz), 22W and 31W for CW pumping levels.

6.3.2.2 Pulsed pump operation

Temperature dependence of Alexandrite in pulsed operation was investigated using 150 μ s pump pulse duration at a repetition rate of 1kHz. This pump pulse duration was the same order of magnitude as the upper state lifetime (τ_f) of the Alexandrite crystal across the oven temperature range (i.e. 20 °C to 130 °C).

Figure 6.8 shows the average threshold pump power at varying holder temperatures. The threshold pump power had a minimum value at \sim 130 °C. At a lower and higher temperature, there was an increase in the threshold power. This indicated that the laser had the highest gain at this temperature.

The behaviour of threshold pump power could be explained by considering the three key parameters that affect the threshold pump power, i.e. the emission cross section (σ_e) and fluorescent lifetime (τ_f) and the excited state absorption (ESA). The threshold pump power varies proportionally with the ESA, and inverse-proportionally to the τ_f and σ_e . While the threshold pump power in CW operation was found minimum at \sim 60°C, the minimum value for 150 μ s pump pulse operation was at a significantly higher temperature of \sim 130°C. As discussed in Section 4.3, the lifetime (τ_f) of Alexandrite is expected to be \sim 260 μ s at 20 °C and decrease down to \sim 80 μ s at 150 °C. Therefore, for 150 μ s pump pulse duration, the

lifetime (τ_f) at low temperature is significantly longer than the pump pulse duration. Thus, the increase of the stimulated emission cross-section (σ_e) initially has higher effect than the decrease in the lifetime (τ_f) on the net gain. Therefore, the threshold value was initially reduced with increasing temperature. However, at temperatures above 130 °C, the lifetime (τ_f) dropped significantly below the pump pulse duration causing an increase in the threshold pump power.

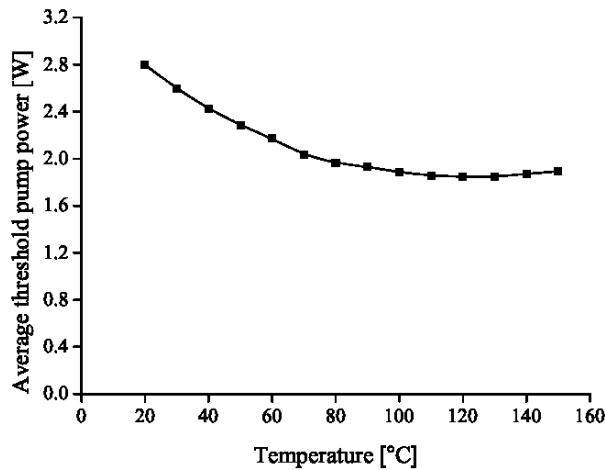


Figure 6.8: Threshold pump power as a function of crystal holder temperature.

Figure 6.9 (a) shows the average output power as a function of crystal holder temperature at 7.9W pumping level. The result shows the power increases with increasing crystal holder temperature and has an optimum value at 90 °C and 7.9W pumping level. To investigate further, the average output power as a function of absorbed pump power for different crystal holder temperatures were measured, as shown in Figure 6.9. In Figure 6.9 (b) the slope efficiency was 25% (at 20°C), 29% (at 60°C), 30% (at 90°), 28% (at 120°C) and 24% (at 150°C), when measured at the straight part of the power curve for each temperature. The highest slope efficiency and also the highest output power were obtained at ~90 °C.

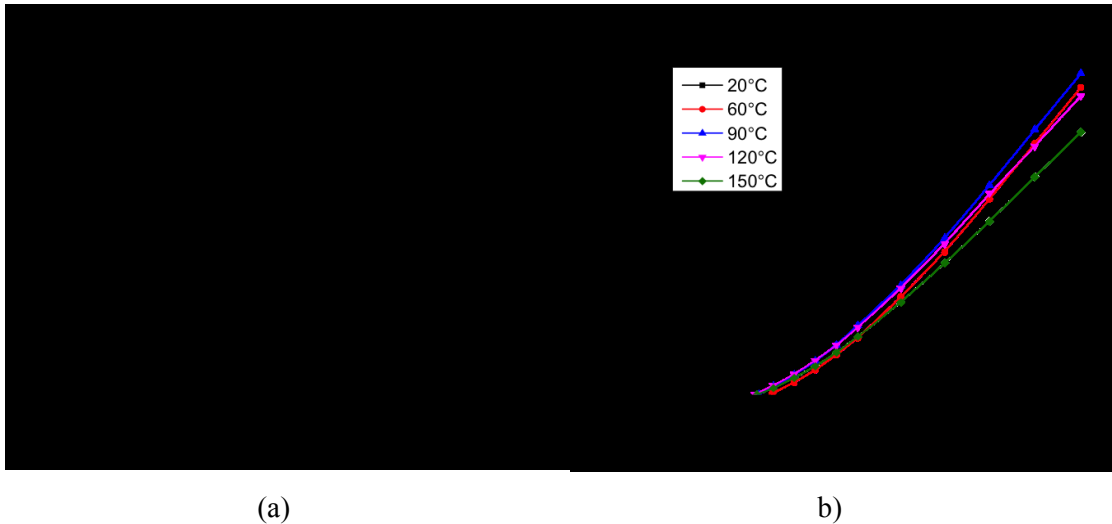


Figure 6.9: (a) Average output power as a function of crystal holder temperature for 7.9W pumping using 150 μ s pump duration at a repetition rate 1kHz. (b) Average output power as a function of absorbed pump power for various crystal holder temperature.

6.4 Q-switching

The section considers Q-switched Alexandrite lasers that are suitable for lidar applications that require high pulse energy and peak power in a range of tens of nanoseconds, such as backscattered lidar. Therefore this section will incorporate Q-switching for high peak power and short pulse duration. Alexandrite is suitable for Q-switching as it has long upper state lifetime ($\sim 260\mu$ s at room temperature), which allows a generation of high pulse energy. Previously Q-switching Alexandrite with a high pulse energy (>100 mJ) and pulse duration in a range of tens to hundreds of nanoseconds has been demonstrated [120], [164]. However, to the best of our knowledge, all the Q-switched Alexandrite lasers previously demonstrated are based on lamp pumping, which results in very low efficiency (optical to optical efficiency of $<1\%$) [120], [164]. Pumping with a high power diode laser would improve laser efficiency, allow compact design and offer long-term stability, making Alexandrite an potential laser sources for remote sensing.

This section starts by describing Q-switching for the Alexandrite laser system. The Q-switching was based on electro-optic (EO) switching due to the faster switching

time when compared to acousto-optic (AO), this was discussed in section 1.6. The use of a Pockels cell as an EO modulator will be discussed, along with two important delay times in Q-switch system, the electrical delay time and pulse build up time. After that, the Q-switched experimental results will be presented in a compact cavity and an extended cavity with an intracavity lens. Finally, the effect of pump pulse duration and temperature in Q-switched laser operation on some important parameters such as laser slope efficiency, pulse energy and pulse duration will be presented.

6.4.1 Q-switching for Alexandrite Laser System

Electro-Optic (EO) modulation was used for Q-switching. The EO modulator was a BBO Pockels cell attached with DC voltage. BBO was chosen for the Pockels cell material as it has many desirable properties for high power and high pulse repetition rate lasers, such as (i) high transmission (>98%) from the UV to the mid-infrared region, (ii) the high optical damage threshold allows high power operation and (iii) the low capacitance allows fast switching with minimal piezoelectric ringing. A BBO crystal with dimensions of 3x3x30mm, AR coated at ~760nm, along with its case was sourced from company EKSMA. A image and a technical drawing of the BBO Pockels cell is shown in Figure 6.10

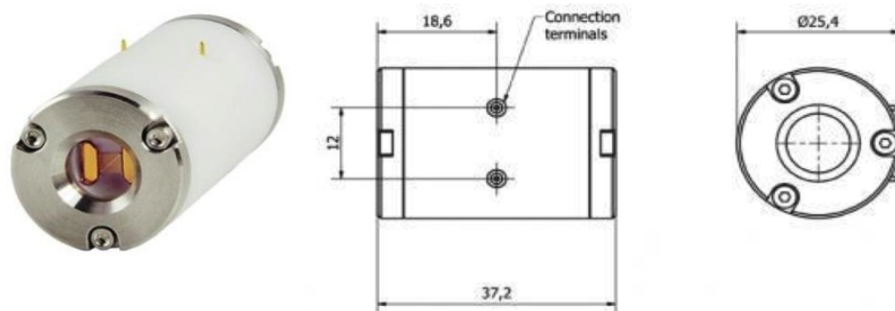


Figure 6.10: BBO Pockels cell module (dimensions in millimeter). Data from company EKSMA.

Initially, the Pockels cell response time was tested using a laser diode lasing at 780nm as a probe beam. The experimental set up is shown in Figure 6.11. The polarizer was placed after the Pockels cell and aligned so the laser diode was transmitted efficiently through it. The transmitted signal was measured after the

polarizer using a photodiode. When the Pockels cell was “off”, light travelling through the cell experienced no phase shift, therefore, transmitted through without losses. When the Pockels cell was “on”, light travelling through the cell experienced a phase shift of $\pi/2$. Therefore, some of the light was reflected by the polarizer. The Pockels cell was operated at 2kV. This voltage was found to be near the quarter-wave voltage where a modulation depth of $\sim 50\%$ was achieved. Figure 6.12 shows an oscilloscope trace of a TTL input signal sent to the Pockels cell (yellow) and the photo diode signal (pink). When the TTL signal was switched off, the actual Pockels cell off time was delayed by $\sim 350\text{ns}$. The Pockels cell rise time, measured from 30% to 70%, was $< 2\text{ns}$. This value was limited by the electrical pulse generator and load capacitance used to drive the Pockels cell to switch between polarization states.

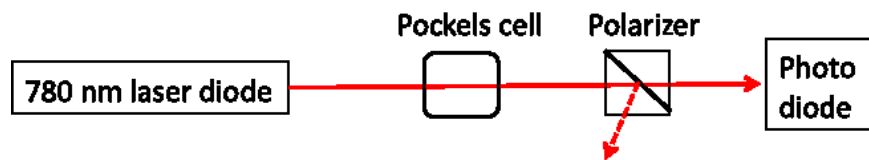


Figure 6.11: Experimental setup for testing Pockels cell response

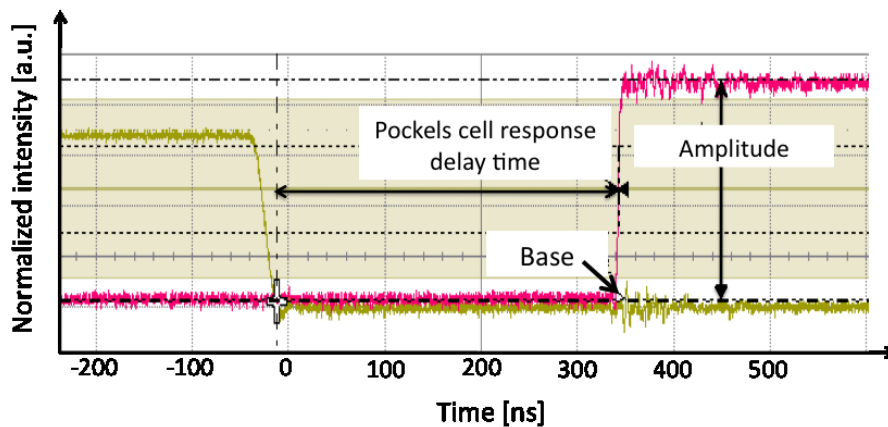


Figure 6.12: Oscilloscope trace of a TTL signal (yellow) delivered to the Pockels cell and photo diode (pink).

Figure 6.13 shows the cavity configuration for Q-switching operation in a compact cavity. The advantage of this cavity is its simplicity as the Pockels cell is simply placed between the gain medium and the OC. When the Pockels Cell was “on”, for each pass the cell introduced a phase shift of $\pi/2$. After the light travelled through

Pockels cell on the return path, the polarization was rotated by 90 degrees from its original polarization. As Alexandrite is a birefringent laser gain media, rotating the polarization by 90 degrees switched the polarization to the low gain axis of the Alexandrite. This technique is usually referred to as the gain-coefficient switching technique [164]. This technique minimizes insertion losses as it requires no polarizer or Brewster plate. This is useful for achieving high pulse energy and high efficiency which is important for Alexandrite as it has a low emission cross section. However, every second round trip, the light was rotated by 180 degrees, which returned to the high gain axis of Alexandrite. Therefore, the Pockels cell hold-off, in principle, was limited to twice the threshold pump power of the cavity [164].

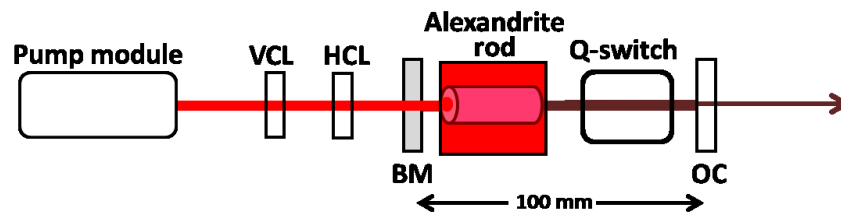


Figure 6.13: Schematic diagram of a compact Q-switching cavity.

Figure 6.14 (a) shows traces of pump pulse intensity (black), Pockels Cell electrical signal (blue) and Q-switch pulse intensity (red) as a function of time. The Pockels cell “on” time relative to the starting of the pump pulse is called the electrical delay time (T_{elec}). The optimum T_{elec} is the time that produces the highest output energy in a single pulse, which in general is slightly larger than the time of maximum inversion [120]. The optimum T_{elec} is different in each specific system, depending on pump pulse duration, temperature or loss factor. In order to optimize the Q-switching pulse energy in each experiment, the Q-switching modulation signal was adjustable independently to the pump laser.

Figure 6.14 (b) shows the close up picture for Figure 6.14 (a) near the Q-switch pulse. The traces show that after the Pockels cell is “off”, there is a delay time before the Q-switch pulse appeared. This delay time is called build up time ($T_{build\ up}$), measured from the when the Pockels cell is actually “off” (at ~ 350 ns after the TTL signal was off as shown in dotted purple line) to the $1/e$ value of the rising

edge of the Q-switch pulse. The $T_{\text{build up}}$ typically varies from a few hundreds of nanoseconds to μs for Alexandrite, depending purely on the cavity dynamics.

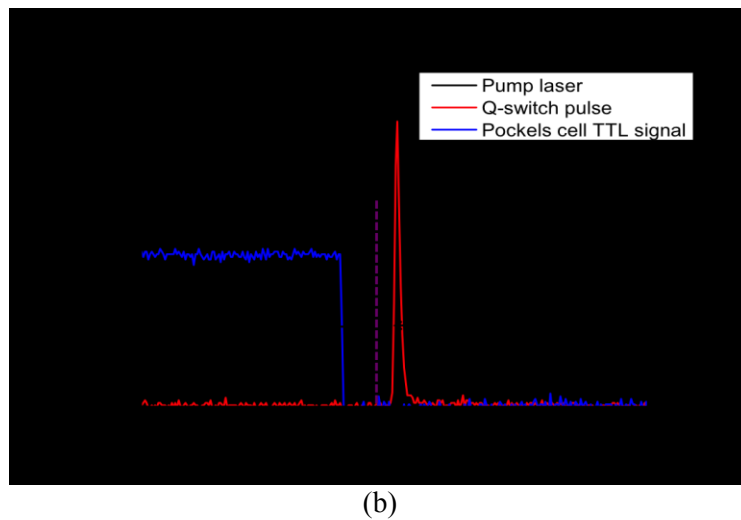
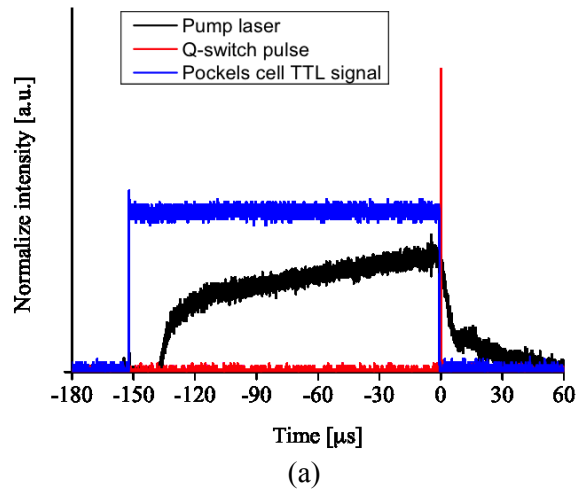


Figure 6.14: (a) Traces of pump pulse (black), Pockels Cell TTL electrical signal (blue) and Q-switch pulse (red) as a function of time. (b) Close up picture (a). The blue shows the real time Pockels cell switch off. The graph shows the pulse $T_{\text{build up}}$ of $\sim 0.35\mu\text{s}$.

6.4.2 Q-switching Experimental Results

6.4.2.1 Compact Cavity

The compact cavity set up is shown in Figure 6.13. In the compact cavity, the cavity length was $\sim 100\text{mm}$, pumping at $150\mu\text{s}$ pump pulse duration at 100Hz . The oven temperature was controlled at $80\text{ }^\circ\text{C}$. Figure 6.15 shows the pulse energy as a function of absorbed pump energy at 100Hz . The Q-switched pulse energy showed a sign of turnover at the absorbed pump power above $\sim 10\text{mJ}$. The initial slope efficiency (η_i) measured from threshold pulse energy to 7mJ was 19.3% and the final slope efficiency (η_f) measured from 8mJ to 13mJ was 7.9% . The blue straight line shows linear fit of the whole power range. The average slope efficiency (η_{ave}) was 11.6% . The Q-switching pulse energy of 1mJ with a pulse duration of 66ns achieved from the absorbed pump power of 13.2mJ . This corresponds to an optical to optical efficiency of 7.5% .

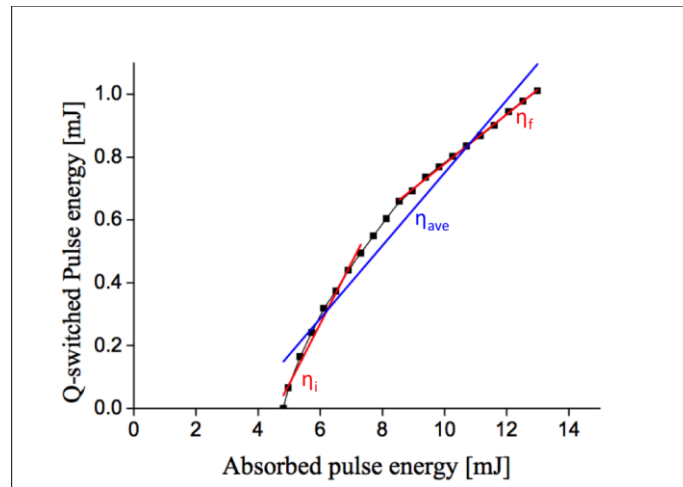


Figure 6.15: Q-switching pulse energy with varying absorbed pump pulse energy

The beam profile at full pumping level is shown in Figure 6.16 (a) The M_x^2 was 1.3 ± 0.1 and M_y^2 was 1.2 ± 0.1 . The peak spectrum is at 753.4nm , with a FWHM of 0.5nm , as shown in Figure 6.16

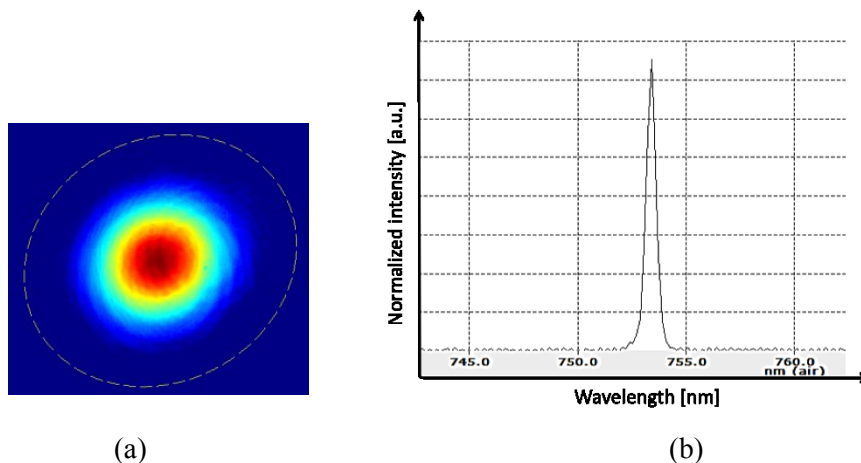


Figure 6.16: Q-switching output at 13.2 absorbed pump pulse energy
(a) beam profile and (b) spectrum.

Figure 6.17 shows the Q-switch pulse energy as a function of absorbed pump power at higher pulse repetition rate of 500Hz. The maximum pulse energy was 0.89mJ achieved from 10.3mJ pumping with good beam quality. The pulse duration at 0.89mJ was 72ns. The graph shows that there was a drop in the Q-switch pulse energy at 8.5mJ. At this point, the Q-switch pulse trace showed a main Q-switch pulse accompanied by a small pulse (post-pulse).

In principle, polarization switching can operate up to twice the threshold value of the cavity [164]. This agrees with the results as the pulse energy dropped at 8.5W for 500Hz. However, in this experiment, a clean Q-switching pulse was achieved with the pump power above twice the threshold value. As threshold power was proportional to the laser mode size, it was possible that the laser mode size above 8.5W was larger than the mode size at low temperature. Therefore, the threshold pump power of the Q-switch pulse energy between 9.0W to 10.2W was, in fact, higher than 4.1mJ.

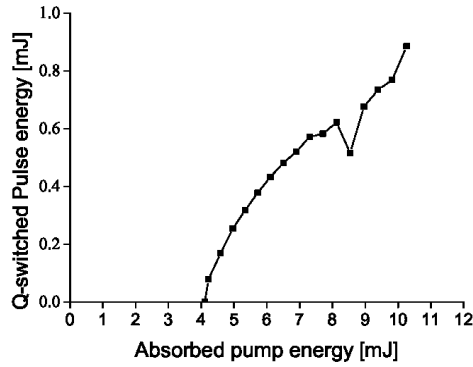


Figure 6.17: Q-switching pulse energy with varying absorbed pump pulse energy.

The beam profile of a Q-switched pulse at 0.89mJ is shown in Figure 6.18. The M^2_x was 1.25 +/- 0.05 and M^2_y was 1.15 +/- 0.03. The spectrum is shown in Figure 6.18 (b). The discrete spectral peaks are seen with a separation of ~4.5nm. The highest peak was at 757.3nm. The spectral peak separation matches the birefringence filtering effect of the Alexandrite crystal discussed in section 6.3.

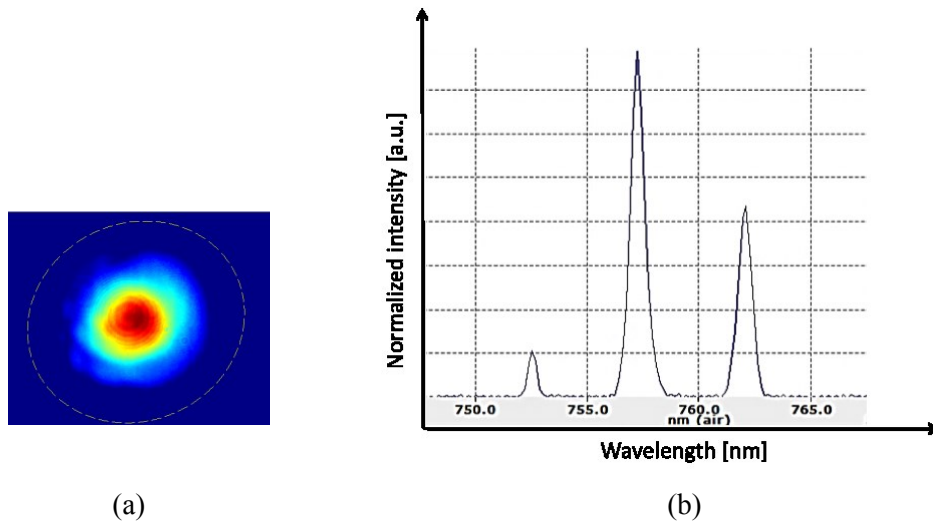


Figure 6.18: Q-switching output at 10.3W pump power (a) spatial beam profile and (b) spectrum.

6.4.2.2 Extended cavity with intracavity lens

The limitation of the compact cavity was that the thermal lensing highly affected the beam quality and cavity stability. In this section, an intracavity lens was inserted to match the laser mode size with the fundamental mode in the crystal. This allowed

the generation of a single mode whilst operating at high power with high repetition rate.

Firstly, we investigated the effect of temperature on an extended cavity in free-running operation. The schematic diagram of the extended cavity is shown in Figure 6.19. The intracavity focusing lens of 120mm focal length was placed 130mm from the back mirror (BM). The total cavity length was ~200mm. The Brewster plate (BS) was inserted between the gain medium and the intracavity lens. The Brewster plate was a 5mm thick plano/plano uncoated substrate placed at the Brewster angle.

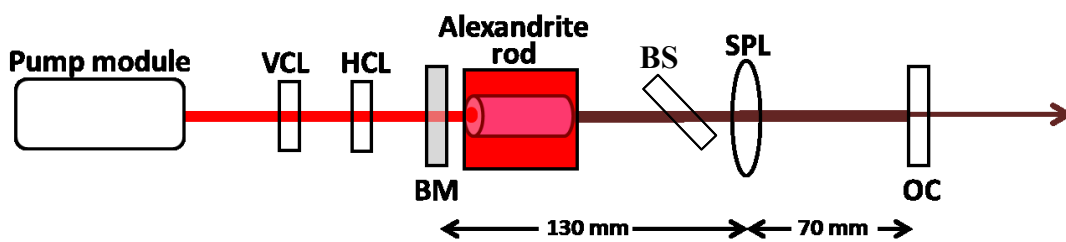


Figure 6.19: Schematic diagram of extended cavity with intracavity lens in free-running operation.

Figure 6.20 shows the free running pulse energy with increasing temperature with pulse pumping at 0.2ms at a repetition rate of 500Hz. A pulse energy of 0.7mJ at 20°C was achieved from 13mJ pumping energy. The pulse energy increases with temperature to a maximum of 1.2mJ at ~110°C. Figure 6.20 also shows an image of the beam quality at 20°C. The beam M-squared at 20 °C was 1.8 and 1.4 for the horizontal and vertical directions respectively.

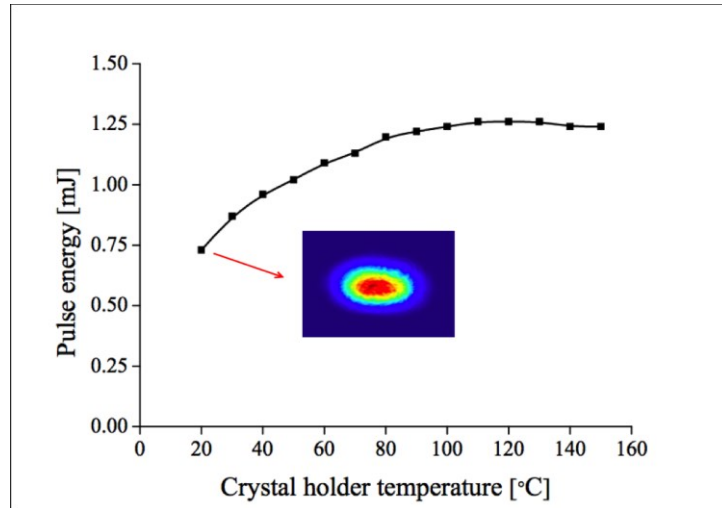


Figure 6.20: Free running pulse energy as a function of temperature, pumping at 0.2ms pulse duration at a repetition rate of 500Hz.

A disadvantage of operating at high temperature is the degradation of the beam quality. Figure 6.21 shows the variation in M-squared as a function of crystal holder temperature. At 20°C, the beam M-squared was 1.8 and 1.4 for the horizontal and vertical directions respectively. The M-squared increases almost linearly in both directions with increasing temperature throughout the whole temperature range. The degradation of the beam was mainly due to thermal lensing, which could come from an increasing of ESA which increases with temperature [54]. However, some of the degradation could be improved by adjusting the cavity, therefore changing the g_1 , g_2 , parameters in order to optimize the beam quality at the optimum temperature.

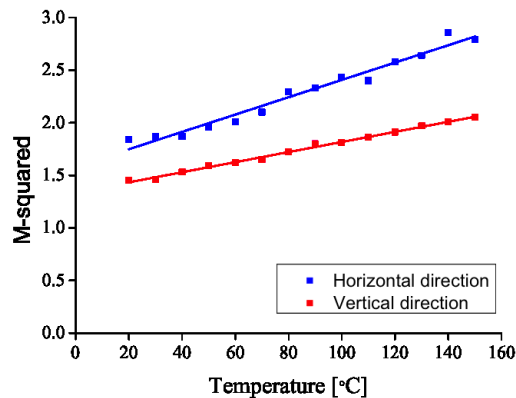


Figure 6.21: Free running M-squared as a function of temperature.

For Q-switch operation, the Pockels cell was placed in the cavity. As this configuration has smallest laser mode size near the back mirror (BM) and larger mode size between the spherical lens (SPL) and the output coupler (OC), the Pockels Cell was placed near the SPL between the spherical lens and the OC to prevent optical damage. Figure 6.22 shows the experimental setup for Q-switching using an extended cavity. The Brewster plate was introduced into the cavity between the gain medium and the SPL to extend pumping energy range. When the Pockels cell was 'on', the light after passing through Pockels cell on the return path experienced losses of $\sim 10\%$ per surface. This allowed Q-switching laser to operate at higher power than twice threshold pump power. The Brewster plate used in this system was a plano-plano uncoated substrate. The OC used in this set up had 95% reflectivity.

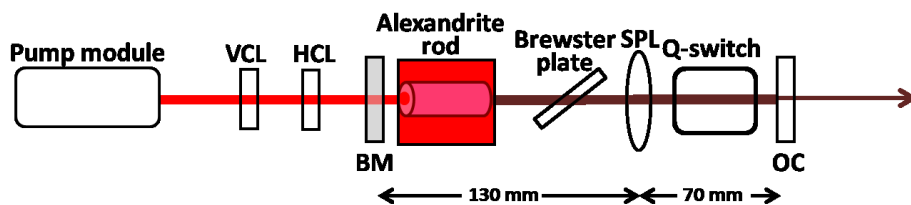


Figure 6.22: Schematic diagram of Q-switching using an extending cavity

Figure 6.23 shows Q-switched pulse energy as a function of absorbed pump energy using $150\mu\text{s}$ pump pulse duration at a repetition rate of 500Hz. The Q-switch pulse energy of 0.76mJ was achieved from absorbed pump energy of 13.5mJ . The slope efficiency measured at the straight part of the graph from the threshold to 8mJ absorbed pump power was 9.5%. The graph shows the Q-switch pulse energy initially increases with the absorbed pulse energy. At high absorbed pulse energies (above $\sim 10\text{mJ}$), the Q-switch pulse energy saturated.

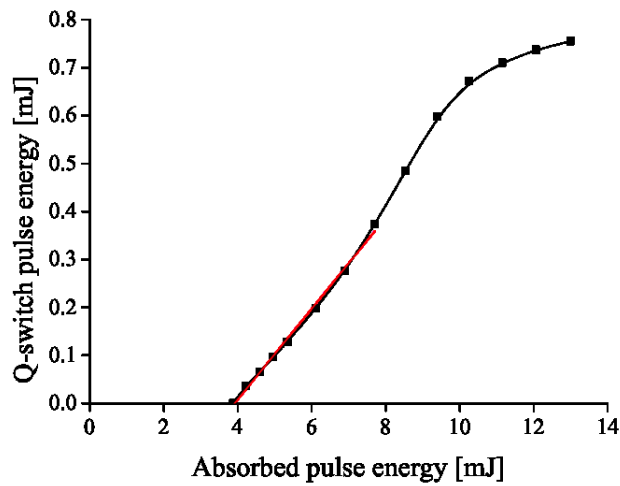


Figure 6.23: Pulse energy as a function of absorbed pump energy using 150 μ s pump pulse duration at a repetition rate of 500Hz. The oven crystal temperature was set at 80 $^{\circ}$ C.

Figure 6.24 shows the temporal, spatial and spectral profile of Q-switch output energy at 0.76mJ. The Q-switch pulse duration (FWHM) was 82ns. The beam quality was near TEM₀₀ with an M-squared of \sim 1.5 and \sim 1.3 in a horizontal and vertical direction respectively. Figure 6.23 (c) shows the spectrum of the output laser. The highest peak wavelength was at 756nm. Discrete spectral peaks with separations \sim 4.5nm were observed.

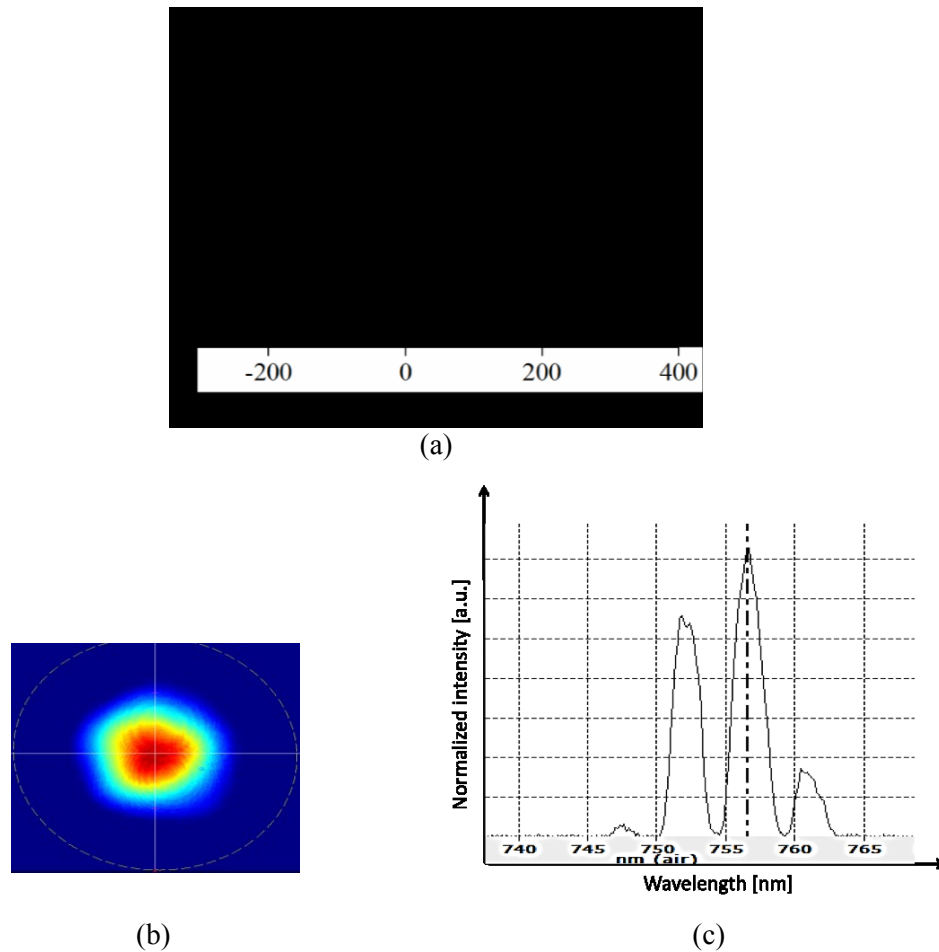


Figure 6.24: (a) the temporal, (b) the spatial and (c) the spectral profile of Q-switch output laser at 0.76mJ at a repetition rate of 500Hz using extended cavity with intracavity lenses.

Figure 6.25 shows the Q-switch pulse energy as a function of absorbed pump pulse energy for 100 μ s, 150 μ s, and 200 μ s and 250 μ s pump pulse durations at a repetition rate of 500Hz. The Q-switch at all pump pulse durations initially increases linearly with the absorbed pump pulse energy. At high absorbed pump-pulse energies, (above \sim 10mJ), the Q-switched pulse energies turned over. The threshold pump energies obtained from Figure 6.25 were 3.2 (for 100 μ s), 3.9 (for 150 μ s), 4.2 (for 200 μ s) and 4.4 (for 250 μ s). This indicated that shorter pump pulse duration led to a lower absorbed pump energy threshold.

As for the shorter pump pulse durations, a higher current was required to drive the pump laser diode to obtain the same absorbed pump pulse energy. Therefore for 100 μ s, in this experiment, no more measurements were made above 7mJ for

absorbed pump pulse energy because of the limit of the maximum current of the laser (which was 22A).

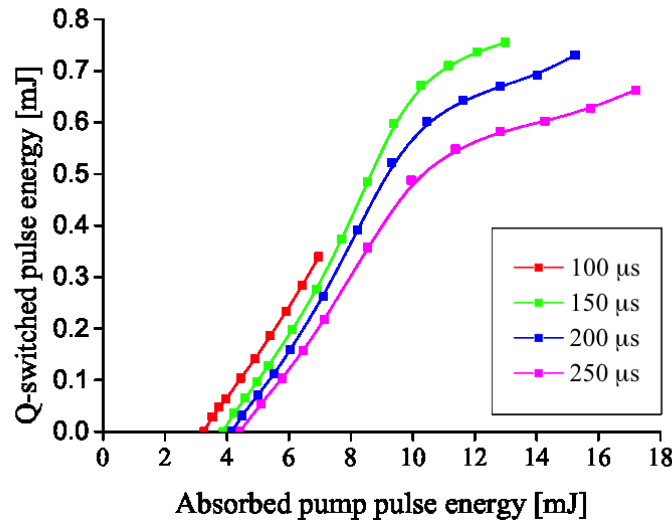


Figure 6.25: Q-switched pulse energy as a function of absorbed pump energy at a repetition rate of 500Hz using four different pump pulse durations.

To achieve an efficient pumping for a pulsed pump system, it is important to look at the dynamical behaviour of the gain medium. The time behaviour of population inversion, $N(t)$ and the pump rate (R_p) is shown in Figure 6.26. By assuming the pump pulse is a step function i.e. the pump rate is zero for time $t < 0$ so $R_p(t) = 0$ and is constant for the time $0 < t < t_p$, where t_p is the pump pulse duration, so $R(t) = R_p = \text{constant}$. If the cavity is ‘closed’ during the pumping time, the population inversion $N(t)$ can then be described as [18],

$$N(t) = N_{\infty} [1 - \exp(-t / \tau_f)] \quad \text{Eq. 6.2}$$

where N_{∞} is the asymptotic value, given by $N_{\infty} = R_p \tau_f$, and τ_f is the excited state lifetime. As shown Figure 6.26, initially the population inversion increases linearly with time but this rate of increase slows and it asymptotically tends to N_{∞} . Therefore, for efficient operation of the laser, the pump pulse duration should be no more than the order of the lifetime, τ_f as pumping for a time $t \gg \tau_f$ would lead to small gains in the population inversion $N(t)$. The pump efficiency (η_c) can be calculated by,

$$\eta_c = \frac{N(t)}{R_p t} = \frac{\tau_f}{t} (1 - e^{-t/\tau_f}) \quad \text{Eq. 6.3}$$

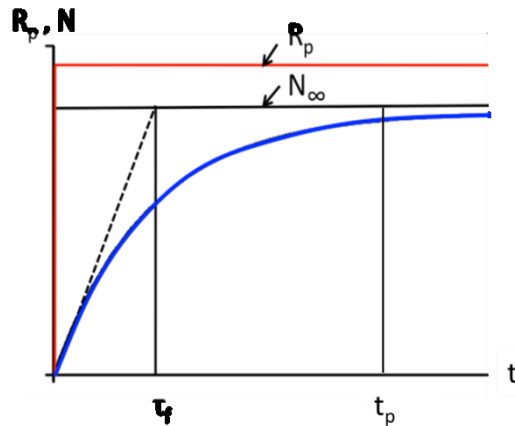


Figure 6.26: Time behavior of population inversion (N) as shown in blue and pump rate (R_p) as shown in red, assuming the cavity is “closed” during the pumping time $0 < t < t_p$,

6.4.3 Pulse Duration and Pulse Build Up Time

The effect of absorbed pump energy and temperature on output pulse duration and pulse build-up time was investigated using a Q-switched Alexandrite laser system in an extended cavity with an intracavity lens described in Figure 6.22.

Figure 6.27 (a) shows the build-up time ($T_{\text{build-up}}$) as a function of absorbed pump energy for five different temperatures. The $T_{\text{build-up}}$ decreases as pump energy is increased for all measured temperatures. The results indicated that the build-up time has a hyperbolic relation with the absorbed pump energy ($T_{\text{build-up}} \propto 1/E_{\text{pump}}$). At the same pump power, the $T_{\text{build-up}}$ of Alexandrite decreases as temperature increases. The reduction of $T_{\text{build-up}}$ at higher temperature could have resulted from increased gain due to an increase of emission cross-section.

Figure 6.27 (b) shows the pulse duration as a function of absorbed pump energy. The result shows a similar trend to the $T_{\text{build-up}}$. As the pump energy or the temperature increases, the gain increases. This not only reduces the $T_{\text{build-up}}$, but also the time required to deplete the population inversion.

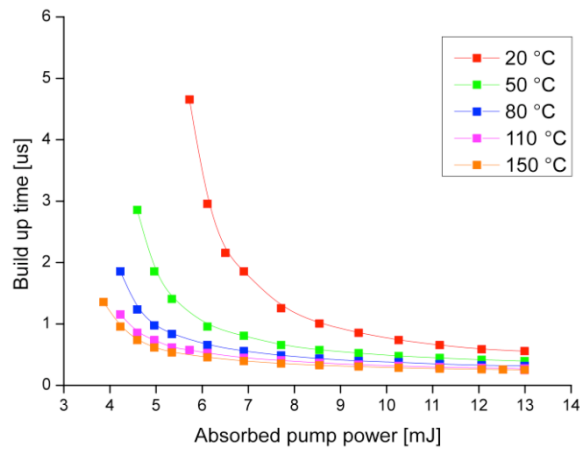


Figure 6.27: Q-switch build up time as a function of absorbed pump power for 5 different temperatures using 150 μ s pump pulse duration.

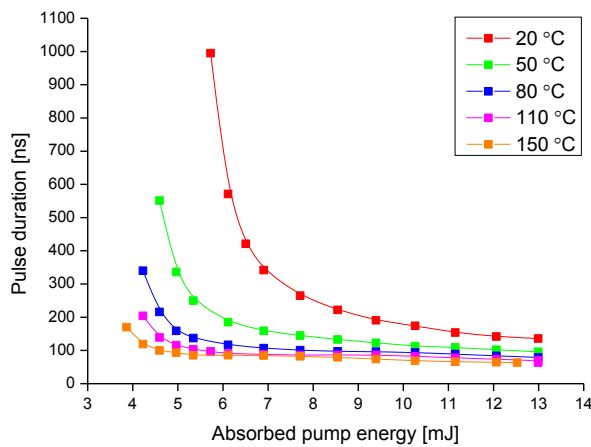


Figure 6.28: Q-switch pulse duration time as a function of absorbed pump power for 5 different temperatures using 150 μ s pump pulse duration.

6.5 Second Harmonic Generation

For remote sensing of cloud and aerosol density or Rayleigh scattering in the atmosphere, laser wavelengths in the UV region are important. For satellite-based active remote sensing UV lasers only based on THG of Nd:YAG (at 355nm) or other OPO processes have been used to date [151]. However, this design has a low

wall-plug efficiency of a few % for THG at 355nm[165], [166]. In contrast to Nd:YAG designs, Alexandrite can be used to generate high power laser light in the UV region (350 - 410nm) more efficiently via second harmonic generation (SHG). Previously pulse energies over 100mJ at 378nm with a second harmonic conversion efficiency of 31% have been achieved via frequency doubling of Q-switching lamp-pumped Alexandrite laser [167].

To investigate the potential Alexandrite for satellite-based active remote sensing with UV light, a BBO crystal was placed at the output of an Alexandrite seed laser which was operating at a centre wavelength of 755nm (as shown in Figure 6.29). The BBO crystal was chosen because of its ability to phase match to the Alexandrite wavelength region, good nonlinear optical coefficient, high damage threshold and high transmission between the UV and mid-infrared [168][167].

Figure 6.29 shows the experimental setup for SHG. For high SHG conversion efficiency, high peak power pulses at 1kHz were realised for the fundamental by using a laser oscillator with cavity dumped Q-switching. As this oscillator was not the focus of this work it is detailed in [160]. Briefly, the fundamental laser had a high beam quality TEM₀₀ (with an M-squared of 1.18 and 1.24 in a horizontal and vertical respectively), the pulse duration was fixed at ~ 3ns at all pump pulse energies and the wavelength was fixed at 758nm (using an internal birefringence filter). After the oscillator, the fundamental beam was focused by a spherical lens (f = 100mm) into a BBO crystal of dimensions 4x4x10mm for SHG. After the crystal, a prism was used to separate the second harmonic beam from the fundamental.

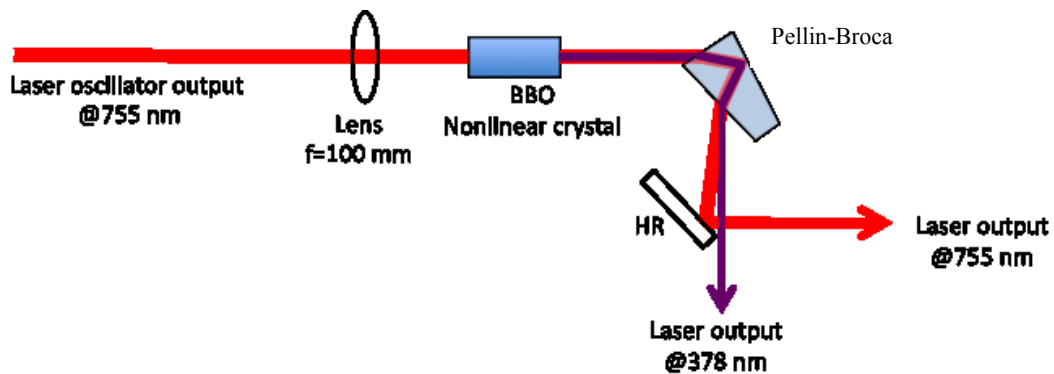


Figure 6.29: Experimental setup for second harmonic generation (SHG).

Figure 6.1 shows the UV output pulse energy as a function of laser oscillator output pulse energy (at 758nm) incident at the BBO nonlinear crystal. At incident pulse energy of 396 μJ , the UV pulse energy of 184 μJ was achieved. This corresponded to conversion efficiency of $\sim 47\%$. It is noted that the system was not optimised which indicated that higher conversion efficiency should be achievable.

Figure 6.31 shows the spectrum of the fundamental and the second harmonic radiation. The spectrum FWHM for both 758nm and 379nm was $<1\text{nm}$ although the precision of this measurement was limited by the resolution of the spectrometer.

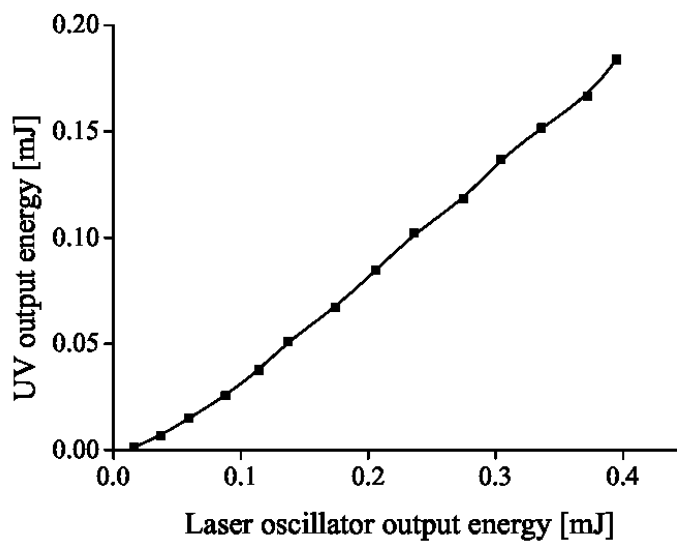


Figure 6.30: UV output energy (at 379nm) as a function of laser oscillator output energy (at 758nm).

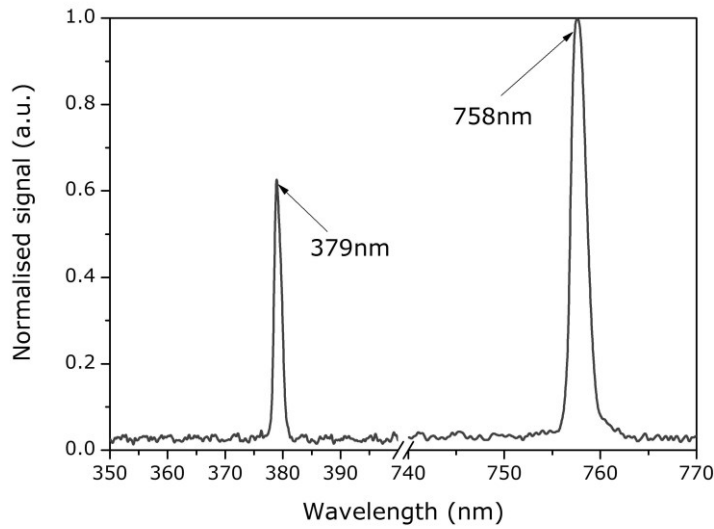


Figure 6.31: Spectrum of fundamental and second harmonic wavelength of the Alexandrite laser.

6.6 Conclusion

For the first time, Q-switched operation has been demonstrated in a diode-pumped Alexandrite laser. This chapter describes the development of a Q-switched Alexandrite laser towards meeting the requirements of satellite based remote sensing, which include high pulse energy and peak power with high efficiency.

One of the main difficulties for achieving efficient end pumping is having a very different beam quality factor in two orthogonal planes of the pump module. Initially, the beam quality of the pump diode was improved. The M-squared was improved from the ratio of the M-squared between the horizontal direction and vertical direction of $\sim 10:1$ to $\sim 3:1$. To enhance Alexandrite efficiency further, a high temperature oven was designed and constructed. The oven can operate at temperatures up to 150°C . In CW operation, the output power and slope efficiency decreased with increasing temperature between 20°C and 150°C . In short pump pulse operation there was an optimum temperature for output power and slope efficiency. For $150\mu\text{s}$ pump pulse duration, the temperature was $\sim 90^{\circ}\text{C}$. This optimum temperature differed from CW operation as increasing temperature

initially has a very small effect on the net gain due to the upper state lifetime being higher than the pump pulse duration. The laser output spectrum of Alexandrite contains two or more peaks with a separation of $\sim 4\text{nm}$ and whose separation increases with increasing temperature. This separation matched the birefringent-filtering of free-spectral range of Alexandrite of $\sim 4\text{nm}$ at a centre wavelength of 750nm .

The second part, which is the main part of this chapter, describes the operation of Q-switched Alexandrite laser systems. Electro-optic Q-switching based on a BBO Pockels cell was used due to the fast switching time in comparison to acousto-optic (AO) switching. This section discussed Pockels cell modulator properties along with two important delay times, electrical delay time and build up time, in a Q-switching system. Q-switched operation of Alexandrite was investigated in two cavity configurations: free space extended cavity and extended cavity with a spherical lens.

In a free space extended cavity, Q-switched pulse energy of 1mJ with pulse duration of 66ns at 100Hz was achieved from 13.2mJ of absorbed pump pulse energy. The beam quality was TEM_{00} with an M-squared of 1.3 and 1.2 in the horizontal and vertical direction respectively. The Q-switch pulse energy initially increases linearly with absorbed pump pulse energy, with a slope efficiency of 19.3%, before turning over at high absorbed pump energy (over 1mJ).

In an extended cavity, the laser mode was controlled with an intracavity lens to match the fundamental mode in the crystal. This allowed the generation of a single mode whilst operating at high power and high repetition rate. However, the laser efficiency was smaller than in a free-space extended cavity. In the extended cavity with an intracavity lens, a Q-switched pulse energy of 0.76mJ with pulse duration of 82ns at 500Hz was achieved from 13.5mJ pump pulse energy. The M-squared of the beam was measured to be 1.5 and 1.3 in the horizontal and vertical direction respectively.

The Q-switched operation section finished with an investigation of pulse duration and build-up time ($t_{\text{build-up}}$) as a function of absorbed pump pulse energy at five different temperatures. The results showed that both the pulse duration and the

build-up time decreased with increasing absorbed pump pulse energy. At the same pumping level, higher temperatures produced shorter pulse duration and build up time. This can be explained by the increasing temperature of the crystal increasing the emission cross section and hence gain. Therefore, the Q-switched pulses required a shorter time to develop.

This chapter finished with a demonstration of frequency doubling of Alexandrite to the UV region using a BBO nonlinear crystal. The fundamental laser output was obtained from a cavity damped Q-switching operation. A maximum output energy of $\sim 0.4\text{mJ}$ at 758nm at a repetition rate of 1kHz was achieved. An output pulse duration of $\sim 3\text{ns}$ was achieved regardless of the absorbed pump energy. A maximum SH output energy of 0.18mJ was achieved at 379nm . This corresponds to a conversion efficiency of $\sim 47\%$. The current frequency doubling system was, in fact, not optimised which indicated that higher conversion efficiency should be achievable.

7 Conclusion

The aim of this work was to develop advanced diode pumped solid-state laser sources for applications in industry and remote sensing. This final chapter summarises key elements of the work presented in this thesis, highlights some important results and proposes some suggestions for future work.

This thesis began with an introduction to diode pumped solid-state lasers. The solid-state material (host and active ions) and diode pumping geometries were described. Thermal issues that can arise in a laser system were presented, including the generation of heat, impact on laser oscillation and cavity stability. Finally, some important methods for generating pulsed laser output such as Q-switching, mode-locking and gain switching which were used throughout this thesis were described.

7.1 Bounce Geometry Oscillator

7.1.1 Summary

Chapter 2 introduced the bounce geometry configuration. The concept of bounce geometry, suitable gain media and heat generation and thermal loading in the bounce geometry were presented. A demonstration of bounce geometry based on Nd:YVO₄ lasing at 1342nm was presented. An output power of 15.9W in multimode operation was achieved with 30% optical to optical efficiency using a compact cavity. To obtain TEM₀₀ laser output, the compact cavity was adapted to an asymmetric cavity. The asymmetric cavity utilised thermally induced lensing to match the fundamental laser mode with the gain medium. This allowed the generation of high power laser output of 10.5W at 53W pump power with good beam quality ($M_x^2 = 1.13$ and $M_x^2 = 1.47$). For pulsed operation, Q-switching was demonstrated using an acousto-optic modulator. A Q-switched TEM₀₀ pulse with an

average power of around 10W was achieved. Q-switched pulses were obtained with pulse repetition rates from 40 - 460kHz. The maximum pulse energy (162 μ J) was achieved at 40kHz.

Mode-locking based on the nonlinear mirror method was also demonstrated. The intensity dependence of the nonlinear mirror was provided by a combination of a nonlinear crystal (BIBO) and a dichroic output coupler. A self-started mode locked pulse train with a repetition rate of 113MHz with an average power of 9.1W was achieved from a pump power of 53 W. Results from the autocorrelation trace show that the main mode locked pulse, with a pulse duration of 10.3ps, was accompanied by many satellite pulses.

7.2 Versatile Pulse Laser Sources for Industrial Applications

7.2.1 Summary

Chapter 3 presented a study of the use of a low power, gain-switched diode seed and ultra-high gain bounce geometry Nd:YVO₄ amplifier system to create a versatile pulsed source at 1064nm. The seed was a laser diode driven by an electrical driving circuit which allows independent control of the pulse duration and pulse repetition rate. The pulse duration ranged from 3.5ns to over 10 μ s and the pulse repetition rate from single shot to 2MHz, limited by the diode driving circuit. The key features of the bounce amplifier were presented. A small signal gain as high as 50 dB was achieved from a pre-amplifier with just 24W pumping with well-preserved beam quality. The pre-amplifier output power was limited by amplified spontaneous emission (ASE). A second amplifier (power amplifier) was necessary for further power scaling. With the power amplifier, an average power of ~14W was achieved for a diode seed input with 188 μ W power and 100ns pulse duration at 100kHz. The highest peak power was obtained at lowest repetition rate. For 3.5ns pulse duration, a peak power of 42 kW was achieved at 50kHz. It is noted here that this study

provided some guidelines for the use of the bounce geometry amplifier for flexible pulse amplification.

7.2.2 Future work

This amplifier could be further developed to achieve higher pulse energies and average powers by using one or more additional amplifiers. This could be useful for applications that require the laser cutting system to work as quickly as possible but with lower precision. Alternatively if high precision cutting is required, higher peak powers could be realized by changing the seed laser for one with sub-nanosecond or picosecond pulses. The pulse duration in this work was only limited by the laser diode driver.

One problem of a square seed input pulse, as shown in chapter 3, was that the amplified pulses have a sharp rising edge followed by exponential decay due to gain saturation. This is a common problem encountered when trying to build a high gain amplifier. One way to further develop the system is to use active pulse shaping by controlling the electrical driving circuit to the seed laser diode [95]. By carefully controlling the input seed form, one can compensate for gain saturation to achieve the desired amplified pulse shape. For example a triangular pulse shape has been shown to compensate for gain saturation to produce a square output shape.

7.3 Alexandrite Lasers

7.3.1 Summary

Chapters 4, 5 and 6 were focused on the Alexandrite laser. Chapter 4 provided an introduction to the Alexandrite laser. Firstly, Alexandrite crystal properties were compared to other tuneable lasers. This was followed by a description of the unique temperature dependent characteristics of Alexandrite in which the emission cross-section increases and the lifetime decreases with increasing temperature. Excited state absorption (ESA), which is an important loss mechanism and also limits the tuning range of Alexandrite, was also described. Two pumping schemes

(lamp pumping and laser diode pumping) were compared, based on previous results in the literature. Thermal issues in laser diode in end-pumping geometry, which was used in the study of Alexandrite laser in this thesis, was described analytically. Finally, in chapter 4, current applications and interesting potential applications of Alexandrite lasers were presented.

Chapter 5 demonstrated Alexandrite laser pumping by a high power diode laser. The laser diode was capable of producing a CW output power of over 60W at 638nm. A simple compact cavity was used which provided 26.2W CW output power with the slope efficiency of $\sim 49\%$. This output power is more than an order of magnitude higher than previously reported values from diode-pumped Alexandrite lasers.

For single mode (TEM_{00}) operation, three extended cavity designs were investigated: free-space extended cavity, extended cavity with internal spherical lens using the positive branch and extended cavity with internal spherical lens using the negative branch of the g-parameters. In the free-space extended cavity, a single mode output power of 1.2W was obtained from 5.5W absorbed pump power, corresponding to 23.6% efficiency. However, the cavity become unstable at higher pump power. In the extended cavity with internal spherical lens using the positive branch, single mode lasing with an output power of 0.74W was obtained from 6.68W QCW diode pump power. At higher pump power, again, the laser became unstable. Higher power single mode operation could be achieved from the extended cavity with internal spherical lens using the negative branch. In this cavity, a single mode with an average output power of 4.1W was obtained using 47W pump power.

Double end pumping was also investigated. To do this, the pump beam was cut in half (horizontally) and sent to pump both sides of the Alexandrite crystal in order to improve thermal effects and also improve the pump beam quality horizontally by a factor of two. The results showed double end pumping had a lower threshold and higher slope efficiency.

In chapter 5, the wavelength tuning was also demonstrated using a self-injection seeding method with an external Littrow grating setup. In this study, the wavelength was tuned smoothly from ~ 730 to 799nm. This chapter finished by comparing the

operation of the end-pumped configuration with the side pumping in a bounce geometry configuration. The result showed that end-pumping gave higher efficiency and better beam quality.

The flexibility of wavelength tuning in the near IR region and the ability to generate high efficiency UV light by a single step second harmonic generation (SHG) makes Alexandrite lasers an interesting alternative laser source for satellite-based remote-sensing applications. In chapter 6, which was the last experimental chapter of the Alexandrite laser, the development of a Q-switched Alexandrite laser working towards meeting the requirements of satellite-based remote sensing applications was described.

Firstly, to enhance Alexandrite laser performance, the pump beam quality of the laser diode was improved. The ratio of the beam quality was improved from the ratio of the M-squared between the horizontal direction and vertical direction of $\sim 10:1$ to $\sim 3:1$. Secondly, a high temperature oven, which could operate at temperatures up to $150\text{ }^{\circ}\text{C}$, was designed and constructed. When using the high temperature controlled oven, for CW operation, the output power and slope efficiency decreased with increasing temperature between 20°C and 150°C , while for $150\mu\text{s}$ pump pulse duration, the optimum temperature was found to be at $\sim 90^{\circ}\text{C}$.

The second part of chapter 6 was about the operation of Q-switched Alexandrite laser systems. A Q-switching Alexandrite laser was obtained using electro-optic Q-switching based on a BBO Pockels cell. In a free-extended cavity, Q-switched pulse energy of 1mJ with pulse duration of 66ns was achieved from 13.2mJ of absorbed pump pulse energy at a repetition rate of 100Hz . In the extended cavity with spherical lens, the laser mode was controlled to match the fundamental mode in the crystal, allowing the generation of higher average power at a high repetition rate. In this cavity, Q-switched pulse energy of 0.76mJ with a pulse duration of 82ns with good beam quality at a repetition rate of 500Hz was achieved from 13.5mJ pump pulse energy. The pulse duration and the pulse build up time were found to decrease with increased pump pulse energy or increased temperature.

Chapter 6 finished with a demonstration of frequency doubling of Alexandrite to the UV region using a BBO nonlinear crystal. Second harmonic output energy of

0.18mJ (at 379nm) was achieved from ~0.4mJ fundamental output laser energy (at 758nm). This corresponds to a conversion efficiency of ~47%. The frequency doubling results were obtained from an un-optimised system, indicating that higher conversion efficiency should be achievable.

7.3.2 Future Work

For lidar applications efficiency is critical. The current Alexandrite laser design proposed in this work could be improved in the following ways:

- By investigating laser operation with different Cr³⁺ doped concentrations
- By using a better beam quality laser diode pump laser
- By using a Brewster cut Alexandrite crystal instead of a Brewster plate in order to decrease the intracavity loss in the Q-switching system.

For applications that require better signal to background ratios or longer ranges than the current system, higher pulse energies (tens of mJ) could be achieved by using a Q-switched Alexandrite laser. This could be realised by using a pump laser diode or multiple laser diodes that can deliver higher pump powers.

For higher temporal resolution, shorter pulse durations could be realised by using the cavity damped Q-switched system used in Chapter 6 and described in [160].

Another interesting area of work could focus on designing a mode-locking Alexandrite laser. Alexandrite is similar to Ti:Sapphire in that it has a broad gain bandwidth in the infrared region that is suitable for a generation of ultra-short pulses. Mode-locked Ti:Sapphire lasers have found numerous applications as a light source for microscopy and industry. Mode-locked Alexandrite lasers based on lamp-pumping have previously been reported with pulse durations of a few tens of picoseconds [111], [169], [170]. A diode-pumped mode-locked Alexandrite laser with low-cost potential and/or high power would be interesting to develop.

References

- [1] T. H. Maiman, Stimulated Optical Radiation in Ruby, vol. 187, no. 4736. 1960.
- [2] M. E. Fermann and I. Hartl, “Ultrafast Fiber Laser Technology,” IEEE J. Sel. Top. Quantum Electron., vol. 15, no. 1, pp. 191–206, 2009.
- [3] S. Hooker and C. Webb, Laser Physics. Oxford University Press, 2010.
- [4] M. Ikeda and S. Uchida, “Blue-violet laser diodes suitable for blu-ray disk,” Phys. Status Solidi Appl. Res., vol. 194, no. 2, pp. 407–413, 2002.
- [5] W. Steen and J. Mazumder, Laser Material Processing. Springer Science & Business Media, 2010.
- [6] D. Vij and K. Mahesh, Medical Applications of Lasers. Springer Science & Business Media, 2013.
- [7] T. Jujii and T. Fukuchi, Laser Remote Sensing. CRC Press, 2005.
- [8] G. Jim P., H. J. Zeiger, and C. H. Townes, “Molecular Microwave Oscillator and New Hyperfine Structure in the Microwave Spectrum of NH^{3+} ,” Phys. Rev., vol. 95, no. 1, p. 282, 1954.
- [9] A. L. Schawlow and C. H. Townes, “Infrared and Optical Masers,” Phys. Rev., vol. 112, no. 6, pp. 1940–1949, 1958.
- [10] J. E. Geusic, H. M. Marcos, and L. G. Van Uitert, “Laser oscillations in nd-doped yttrium aluminum, yttrium gallium and gadolinium garnets,” Appl. Phys. Lett., vol. 4, no. 10, pp. 182–184, 1964.
- [11] F. P. Schäfer, “Organic Dye Solution Laser,” Appl. Phys. Lett., vol. 9, no. 8, p. 306, 1966.

- [12] A. Javan, W. R. Bennett, and D. R. Herriott, "Population inversion and continuous optical maser oscillation in a gas discharge containing a He-Ne mixture," *Phys. Rev. Lett.*, vol. 6, no. 3, pp. 106–110, 1961.
- [13] O. G. Peterson, "cw operation of an organic dye solution," *Appl. Phys. Lett.*, vol. 17, no. 6, p. 245, 1970.
- [14] E. A. Arbabzadah, C. C. Phillips, and M. J. Damzen, "Free-running and Q-switched operation of a diode pumped Er:YSGG laser at the 3 μm transition," *Appl. Phys. B*, vol. 111, no. 2, pp. 333–339, 2013.
- [15] J. C. Walling, D. F. Heller, and H. Samelson, "Tunable Alexandrite Lasers: Development and performance," *Quan. Elec. IEEE*, vol. 21, no. 10, pp. 1568-1581. 1985.
- [16] R. Scheps, *Introduction to Laser Diode-Pumped Solid State Lasers*. SPIE The International Society for Optical Engineering, 2001.
- [17] W. Koechner, *Solid-State Laser Engineering*, Sixth. Springer Science & Business Media, 2006.
- [18] O. Svelto, *Principles of Lasers*, Fifth. Springer, 2010.
- [19] P. F. Moulton, J. G. Manni, and G. a. Rines, "Spectroscopic and Laser Characteristics of Er,Cr:Ysgg.," *IEEE J. Quantum Electron.*, vol. 24, no. 6, pp. 960–973, 1988.
- [20] E. C. Honea, R. J. Beach, S. B. Sutton, J. a. Speth, S. C. Mitchell, J. a. Skidmore, M. a. Emanuel, and S. a. Payne, "115-W Tm:YAG diode-pumped solid-state laser," *IEEE J. Quantum Electron.*, vol. 33, no. 9, pp. 1592–1600, 1997.
- [21] P. A. Budni, L. A. Pomeranz, M. L. Lemons, C. A. Miller, J. R. Mosto, and E. P. Chicklis, "Efficient mid-infrared laser using 1.9 μm -pumped Ho:YAG and ZnGeP₂ optical parametric oscillators," *Opt. Soc. Am. B.*, vol. 17, no. 5, pp. 723–728, 2000.

- [22] Y. H. Peng, Y. X. Lim, J. Cheng, Y. Guo, Y. Y. Cheah, and K. S. Lai, "Near fundamental mode 1.1 kW Yb:YAG thin-disk laser," *Opt. Lett.*, vol. 38, no. 10, pp. 1709–11, May 2013.
- [23] A. Charlton, M. R. Dickinson, and T. A. King, "High Repetition Rate, High Average Power Er:YAG Laser at 2.94 μm ," *J. Mod. Opt.*, vol. 36, no. 10, pp. 1393–1400, 1989.
- [24] G. Huber, C. Kränkel, and K. Petermann, "Solid-state lasers: status and future [Invited]," *J. Opt. Soc. Am. B*, vol. 27, no. 11, p. B93, 2010.
- [25] D. Golla, S. Knoke, W. Schöne, G. Ernst, M. Bode, a. Tünnermann, and H. Welling, "300-W cw diode-laser side-pumped Nd:YAG rod laser," *Opt. Lett.*, vol. 20, no. 10, p. 1148, May 1995.
- [26] A. I. Zagumennyi, V. G. Ostroumov, I. A. Shcherbakov, T. Jensen, and J. P. Meyen, "The Nd:GdVO₄ crystal: a new material for diode-pumped lasers," *Sov. Quan. Elec.* vol. 1071, pp. 1992–1994, 1992.
- [27] J. R. O'Connor, "Unusual crystal-field energy levels and efficient laser properties of YVO₄:Nd," *Appl. Phys. Lett.*, vol. 9, no. 11, p. 407, 1966.
- [28] I. Sokolska, E. Heumann, S. Kuck and T. Lukasiewicz., "Laser oscillation of Er³⁺:YVO₄ and Er³⁺, Yb³⁺:YVO₄ crystals in the spectral range around 1.6 μm ," *App. Phy. B*, vol. 71, no. 6, pp. 893-896, 2000.
- [29] Y. Y. Kalisky, *The Physics and Engineering of Solid State Lasers*, Vol. 71. SPIE Press, 2006.
- [30] J. Lu, K. Ueda, H. Yagi, T. Yanagitani, Y. Akiyama, and A. A. Kaminskii, "Neodymium doped yttrium aluminum garnet (Y₃Al₅O₁₂) nanocrystalline ceramics—a new generation of solid state laser and optical materials," *Alloys and compounds*, vol. 341, pp. 220–225, 2002.
- [31] C. T. Walters, J. L. Dulaney, B. E. Campbell, and H. M. Epstein, "Nd-glass burst laser with kW average power output," *IEEE J. Quan. Elec.*, vol. 31, no. 2, pp. 293–300, 1995.

- [32] E. Snitzer and R. Woodcock, "Yb³⁺- Er³⁺ Glass laser," *Appl. Phys. Lett.*, vol. 6, no. 3, p. 45, 1965.
- [33] G. D. Baldwin, E.P. Riedel, "Measurements of Dynamic Optical Distortion in Nd-Doped Glass Laser Rods," *J. Appl. Phys.*, vol. 38, no. 7, p. 2726, 1967.
- [34] J. S. Uppal, P. D. Gupta, and D. D. Bhawalkar, "Study of thermally induced active birefringence in Nd:glass laser rods," *J. Appl. Phys.*, vol. 54, no. 11, p. 6615, 1983.
- [35] D. Krennrich, R. Knappe, B. Henrich, R. Wallenstein, and J. a. L'huillier, "A comprehensive study of Nd:YAG, Nd:YAlO₃, Nd:YVO₄ and Nd:YGdVO₄ lasers operating at wavelengths of 0.9 and 1.3 μ m. Part 1: cw-operation," *Appl. Phys. B*, vol. 92, no. 2, pp. 165–174, Jun. 2008.
- [36] A. W. Tucker, M. Birnbaum, C. L. Fincher, and J. W. Erler, "Stimulated-emission cross section at 1064 and 1342 nm in Nd : YVO₄," *J. Appl. Phys.*, vol. 48, no. 1977, pp. 4907–4911, 1977.
- [37] L. Fornasiero, T. Jensen, and G. Huber, "Excited state absorption and stimulated emission of Nd³⁺ in crystals," vol. 553, pp. 549–553, 1998.
- [38] C. R. Santos, M. R. Tonetto, C. D. Presoto, M. C. Bandéca, O. B. Oliveira Jr., S. Calabrez-Filho, and M. F. Andrade, "Application of Er:YAG and Er, Cr:YSGG lasers in cavity preparation for dental tissues: a literature review," *World J. Dent.*, vol. 3, no. 4, pp. 340–343, 2012.
- [39] S. D. Setzler, M. P. Francis, Y. E. Young, J. R. Konves and E. P. Chicklis, "Resonantly Pumped Eyesafe Erbium Lasers," vol. 11, no. 3, pp. 645–657, 2005.
- [40] K. S. Lai, P. B. Phua, R. F. Wu, Y. L. Lim, E. Lau, S. W. Toh, B. T. Toh, and A. Chng, "120-W continuous-wave diode-pumped Tm:YAG laser," *Opt. Lett.*, vol. 25, no. 21, p. 1591, Nov. 2000.
- [41] P. A. Budni, C. R. Ibach, S. D. Setzler, E. J. Gustafson, R. T. Castro, and E. P. Chicklis, "50-mJ , Q-switched , 2.09- μ m holmium laser resonantly pumped by a diode-pumped 1.9 μ m thulium laser," vol. 28, no. 12, pp. 1016–1018, 2003.

- [42] W. Koechner, "Thermal Lensing in a Nd:YAG Laser Rod.," *Appl. Opt.*, vol. 9, no. 11, pp. 2548–53, Nov. 1970.
- [43] R. A. Fields, M. Birnbaum, and C. L. Fincher, "Highly efficient Nd:YVO₄ diode-laser end-pumped laser," *Appl. Phys. Lett.*, vol. 51, no. 23, pp. 1885-1886, 1987.
- [44] S. C. Tidwell, J. F. Seamans, M. S. Bowers, and A. K. Cousins, "Scaling CW diode-end-pumped Nd:YAG lasers to high average powers," *IEEE J. Quantum Electron.*, vol. 28, no. 4, pp. 997–1009, 1992.
- [45] K. Furuta, T. Kojima, S. Fujikawa, and J. Nishimae, "Diode-pumped 1 kW Q-switched Nd:YAG rod laser with high peak power and high beam quality.," *Appl. Opt.*, vol. 44, no. 19, pp. 4119–4122, 2005.
- [46] P. E. L. Wibert, J. P. Chernoe, G. E. Company, O. B. Waddell, and L. A. Moucha, "Multiple Internal Reflection Face-Pumped Laser," U.S. patent 3,633,126., 1972
- [47] T. Kane, R. Eckardt, and R. Byer, "Reduced thermal focusing and birefringence in zig-zag slab geometry crystalline lasers," *IEEE J. Quantum Electron.*, vol. 19, no. 9, pp. 1351–1354, Sep. 1983.
- [48] J. E. Bernard and a. J. Alcock, "High-efficiency diode-pumped Nd:YVO₄ slab laser," *Opt. Lett.*, vol. 18, no. 12, p. 968, Jun. 1993.
- [49] A. Minassian, B. Thompson, and M. J. Damzen, "Ultrahigh-efficiency TEM₀₀ diode-side-pumped Nd:YVO₄ laser," *Appl. Phys. B Lasers Opt.*, vol. 76, no. 4, pp. 341–343, 2003.
- [50] A. Minassian, B. a. Thompson, G. Smith, and M. J. Damzen, "High-power scaling (>100 W) of a diode-pumped TEM₀₀ Nd:GdVO₄ laser system," *IEEE J. Sel. Top. Quantum Electron.*, vol. 11, no. 3, pp. 621–625, May 2005.
- [51] A. Giesen, H. Hiigep, A. Voss, K. Wittig, U. Brauch, and H. Opower, "Scalable Concept for Diode-Pumped High-Power Solid-State Lasers," vol. 372, pp. 365–372, 1994.

- [52] A. Giesen and J. Speiser, “Fifteen Years of Work on Thin-Disk Lasers: Results and Scaling Laws,” *IEEE J. Sel. Top. Quantum Electron.*, vol. 13, no. 3, pp. 598–609, 2007.
- [53] M. L. Shand, J. C. Walling, and R. C. Morris., “Excited-state absorption in the pump region of alexandrite,” *J. Appl. Phys.*, vol. 52, no. 2, pp. 953-955, 1981.
- [54] M.L. Shand and H. P. JenssenI, “Temperature Dependence of the Excited-State Absorption of Alexandrite,” *Quan. Elec.* vol. 19, no. 3, pp. 480–484, 1983.
- [55] V. Magni, “Resonators for solid-state lasers with large-volume fundamental mode and high alignment stability,” *Appl. Opt.*, vol. 25, no. 1, p. 107, Jan. 1986.
- [56] R. Bhandari and T. Taira, “Megawatt level UV output from $\langle 110 \rangle$ Cr⁴⁺:YAG passively Q-switched microchip laser.,” *Opt. Express*, vol. 19, no. 23, pp. 22510–22514, 2011.
- [57] J. A Morris and C. R. Pollock, “Passive Q switching of a diode-pumped Nd:YAG laser with a saturable absorber.,” *Opt. Lett.*, vol. 15, no. 8, pp. 440–442, 1990.
- [58] U. Keller, K. J. Weingarten, X. K. Franz, D. Kopf, B. Braun, I. D. Jung, R. Fluck, H. Clemens, N. Matuschek, and J. A. Der Au, “Semiconductor Saturable Absorber Mirrors (SESAM ’ s) for Femtosecond to Nanosecond Pulse Generation in Solid-State Lasers,” vol. 2, no. 3, pp. 435–453, 1996.
- [59] H. a. Haus, “Theory of Mode-locking with a Slow Saturable Absorber,” *Quan. Elec.*, vol. 11, no. 9, pp. 736-746, 1975.
- [60] H. a. Haus, “Theory of mode-locking with a fast saturable absorber,” *J. Appl. Phys.*, vol. 46, no. 7, pp. 3049–3058, 1975.
- [61] J. E. Bernard and A. J. Alcock, “High-repetition-rate diode-pumped Nd:YVO₄ slab laser,” vol. 19, no. 22, pp. 1861–1863, 1994.
- [62] M. J. Damzen, M. Trew, E. Rosas, and G. J. Crofts, “Continuous-wave Nd:YVO₄ grazing-incidence laser with 22.5 W output power and 64% conversion efficiency,” *Opt. Comm.*, ,vol. 196, no. September, pp. 237–241, 2001.

- [63] M. Frede, R. Wilhelm, and D. Kracht, "250 W end-pumped Nd:YAG laser with direct pumping into the upper laser level.," *Opt. Lett.*, vol. 31, no. 24, pp. 3618–3619, 2006.
- [64] V. Lupei, N. Pavel, and T. Taira, "Laser emission in highly doped Nd:YAG crystals under $^4F_{5/2}$ and $^4F_{3/2}$ pumping.," *Opt. Lett.*, vol. 26, no. 21, pp. 1678–80, 2001.
- [65] D. Sauder, A. Minassian, and M. J. Damzen, "High efficiency laser operation of 2 at .% doped crystalline Nd : YAG in a bounce geometry," *Opt. Exp.* vol. 14, no. 3, pp. 1079–1085, 2006.
- [66] A. Minassian and M. J. Damzen, "20 W bounce geometry diode-pumped Nd:YVO₄ laser system at 1342 nm," *Opt. Commun.*, vol. 230, no. 1–3, pp. 191–195, 2004.
- [67] M. Okida, A. Tonouchi, and M. Itoh, "Thermal - lens measurement in a side-pumped 1.3 μm Nd:YVO₄ bounce laser." *Opt. Commun.*, vol. 277, no. 1, pp. 125-129, 2007
- [68] C. Q. Wang, Y. T. Chow, L. Reekie, W. a Gambling, H. J. Zhang, L. Zhu, and X. L. Meng, "A comparative study of the laser performance of diode-laser-pumped Nd : GdVO₄ and Nd :YVO₄ crystals," *App. Phys. B.*, vol. 772, pp. 769–772, 2000.
- [69] J. C. G. Bermudez, V. J. Pinto-robledo, A. V Kir, and M. J. Damzen, "The thermo-lensing effect in a grazing incidence , diode-side-pumped Nd :YVO₄ laser," *Opt. Commun.*, vol. 210, no. September, pp. 75–82, 2002.
- [70] Ş. A. Amarande and M. J. Damzen, "Measurement of the thermal lens of grazing-incidence diode-pumped Nd:YVO₄ laser amplifier," *Opt. Commun.*, vol. 265, no. 1, pp. 306–313, Sep. 2006.
- [71] X. Yan, M. Gong, F. He, Q. Liu, X. Fu, and D. Wang, "Numerical modeling of the thermal lensing effect in a grazing-incidence laser," *Opt. Commun.*, vol. 282, no. 9, pp. 1851–1857, May 2009.

- [72] E. A. Arbabzadah, P. C. Shardlow, A. Minassian, and M. J. Damzen, "Pulse control in a Q-switched Nd:YVO₄ bounce geometry laser using a secondary cavity," *Opt. Lett.*, vol. 39, no. 12, pp. 3437–40, 2014.
- [73] J. ying Peng, J. guang Miao, Y. gang Wang, B. shan Wang, H. ming Tan, L. sheng Qian, and X. yu Ma, "High-average-power and high-conversion-efficiency continuous wave mode-locked Nd:YVO₄ laser with a semiconductor absorber mirror," *Opt. Laser Technol.*, vol. 39, no. 6, pp. 1135–1139, 2007.
- [74] C. J. S. M. Golling, R. P. K. Petermann, and G. H. U. Keller, "High-power ultrafast thin disk laser oscillators and their potential for sub-100-femtosecond pulse generation," pp. 281–295, 2009.
- [75] H. D. Sun, G. J. Valentine, R. Macaluso, S. Calvez, D. Burns, M. D. Dawson, T. Jouhti, and M. Pessa, "Low-loss 1.3-microm GaInNAs saturable Bragg reflector for high-power picosecond neodymium lasers," *Opt. Lett.*, vol. 27, no. 23, pp. 2124–6, 2002.
- [76] K. Stankov and J. Jethwa, "A new mode-locking technique using a nonlinear mirror," *Opt. Commun.*, vol. 66, no. 1, 1988.
- [77] G. M. Thomas, A. Bäuerle, D. J. Farrell, and M. J. Damzen, "Nonlinear mirror modelocking of a bounce geometry laser," *Opt. Express*, vol. 18, no. 12, pp. 12663–8, Jun. 2010.
- [78] R. Fluck, G. Zhang, U. Keller, K. J. Weingarten, and M. Moser, "Diode-pumped passively mode-locked 1.3-microm Nd:YVO₄ and Nd:YLF lasers by use of semiconductor saturable absorbers," *Opt. Lett.*, vol. 21, no. 17, pp. 1378–80, 1996.
- [79] H. Iliev, I. Buchvarov, V. Alexandrov, S. Kurimura, and V. Petrov, "Steady state mode-locking of the Nd:YVO₄ laser operating on the 1.34 μm transition using intracavity SHG in BIBO or PPMgSLT," *SPIE LASE.*, International Society for Optics and Photonics., vol. 7912, pp. 79120T–79120T–7, 2011.
- [80] H. Iliev, I. Buchvarov, and V. Petrov, "1.34-μm Nd: YVO₄ Laser Mode-Locking by Chi-2 Lensing in Periodically Poled Stoichiometric Lithium Tantalate," *Adv. Solid. Pho.*, AWA 16, Feb, 2011.

- [81] Y. H. Liu, Z. D. Xie, S. D. Pan, X. J. Lv, Y. Yuan, X. P. Hu, J. Lu, L. N. Zhao, C. D. Chen, G. Zhao, and S. N. Zhu, "Diode-pumped passively mode-locked Nd:YVO₄ laser at 1342 nm with periodically poled LiNbO₃," *Opt. Lett.*, vol. 36, no. 5, pp. 698–700, Mar. 2011.
- [82] A. E. Siegman, *Lasers*. University Science Books, 1990.
- [83] I. Freitag, A. Tünnermann, and H. Welling, "Passively Q-switched Nd:YAG ring lasers with high average output power in single-frequency operation," *Opt. Lett.*, vol. 22, no. 10, pp. 706–708, 1997.
- [84] J. J. Zayhowski and C. Dill III, "Diode-pumped passively Q-switched picosecond microchip lasers," *Opt. Lett.*, vol. 19, no. 18, pp. 1427–1429, 1994.
- [85] H. Sakai, H. Kan, and T. Taira, "Passively Q-switched Nd³⁺:YAG microchip laser," *Society*, vol. 16, no. 24, pp. 19891–19899, 2008.
- [86] A. Agnesi, F. Pirzio, G. Reali, and G. Piccinno, "Subnanosecond diode-pumped passively Q-switched Nd:GdVO₄ laser with peak power >1 MW," *Appl. Phys. Lett.*, vol. 89, no. 10, p. 101120, 2006.
- [87] P. Dupriez, a. Piper, a. Malinowski, J. K. Sahu, M. Ibsen, B. C. Thomsen, Y. Jeong, L. M. B. Hickey, M. N. Zervas, J. Nilsson, and D. J. Richardson, "High average power, high repetition rate, picosecond pulsed fiber master oscillator power amplifier source seeded by a gain-switched laser diode at 1060 nm," *IEEE Photonics Technol. Lett.*, vol. 18, no. 9, pp. 1013–1015, 2006.
- [88] H. Liu, C. Gao, J. Tao, W. Zhao, and Y. Wang, "Compact tunable high power picosecond source based on Yb-doped fiber amplification of gain switch laser diode," *Opt. Exp.*, vol. 16, no. 11, pp. 7888–7893, 2008.
- [89] A. V. Smith, B. T. Do, G. R. Hadley, and R. L. Farrow, "Optical damage limits to pulse energy from fibers," *IEEE J. Sel. Top. Quantum Electron.*, vol. 15, no. 1, pp. 153–158, 2009.
- [90] X. Délen, F. Balembois, and P. Georges, "Direct amplification of a nanosecond laser diode in a high gain diode-pumped Nd:YVO₄ amplifier," *Opt. Lett.*, vol. 39, no. 4, pp. 997–1000, 2014.

- [91] A. Agnesi, L. Carrà, F. Pirzio, and G. Reali, “Low-power 100-ps microchip laser amplified by a two-stage Nd:YVO₄ amplifier module,” *Appl. Phys. B*, vol. 109, no. 4, pp. 659–662, Oct. 2012.
- [92] A. Agnesi, L. Carra, R. Piccoli, F. Pirzio, and G. Reali, “Nd:YVO₄ amplifier for ultrafast low-power lasers,” *Opt. Lett.*, vol. 37, no. 17, pp. 3612–3614, 2012.
- [93] J. E. Bernard, E. Mccullough, and A. J. Alcock, “High gain , diode-pumped Nd : YVO₄ slab amplifier Probe beam Nd : YVO₄,” *Opt. Commun.*, vol. 109, no. 1, pp. 109–114, 1994.
- [94] M. G. Littman and H. J. Metcalf, “Spectrally narrow pulsed dye laser without beam expander.,” *Appl. Opt.*, vol. 17, no. 14, pp. 2224–7, Jul. 1978.
- [95] K. T. Vu, a Malinowski, D. J. Richardson, F. Ghiringhelli, L. M. B. Hickey, and M. N. Zervas, “Adaptive pulse shape control in a diode-seeded nanosecond fiber MOPA system.,” *Opt. Express*, vol. 14, no. 23, pp. 10996–11001, 2006.
- [96] R. Ell, U. Morgner, F. X. Kãârtner, J. G. Fujimoto, E. P. Ippen, V. Scheuer, G. Angelow, T. Tschudi, M. J. Lederer, a Boiko, and B. Luther-Davies, “Generation of 5-fs pulses and octave-spanning spectra directly from a Ti:sapphire laser.,” *Opt. Lett.*, vol. 26, no. 6, pp. 373–375, 2001.
- [97] A. Bartels, D. Heinecke, and S. A. Diddams, “Passively mode-locked 10 GHz femtosecond Ti : sapphire laser,” *Opt. Lett.*, vol. 33, no. 16, pp. 1905–1907, 2008.
- [98] R. Scheps, “Cr-doped solid state lasers pumped by visible laser diodes,” *Opt. Mater. (Amst.)*, vol. 1, no. 1, pp. 1–9, Jan. 1992.
- [99] M. Stalder, B. H. T. Chai, and M. Bass, “Flashlamp pumped Cr:LiSrAlF₆ laser,” *Appl. Phys. Lett.*, vol. 58, no. 3, p. 216, 1991.
- [100] R. Scheps, J. F. Myers, H. B. Serreze, a Rosenberg, R. C. Morris, and M. Long, “Diode-pumped Cr:LiSrAlF₆ laser.,” *Opt. Lett.*, vol. 16, no. 11, pp. 820–822, 1991.

- [101] P. M. W. French and R. Mellish, "Mode-locked all-solid-state diode-pumped Cr : LiSAF laser," *Opt. Lett.*, vol. 18, no. 22, pp. 1934–1936, 1993.
- [102] N. H. Rizvi, P. M. French, and J. R. Taylor, "Generation of 33-fs pulses from a passively mode-locked Cr³⁺:LiSrAlF₆ laser.," *Opt. Lett.*, vol. 17, no. 22, pp. 1605–1607, 1992.
- [103] S. Uemura and K. Torizuka, "Generation of 10 fs pulses from a diode-pumped Kerr-lens mode-locked Cr:LiSAF laser," *Japanese J. Appl. Phys. Part 1- Regular Pap. Short Notes Rev. Pap.*, vol. 39, no. 6A, pp. 3472–3473, 2000.
- [104] J.-M. Hopkins, G. J. Valentine, B. Agate, a. J. Kemp, U. Keller, and W. Sibbett, "Highly compact and efficient femtosecond Cr:LiSAF lasers," *IEEE J. Quantum Electron.*, vol. 38, no. 4, pp. 360–368, Apr. 2002.
- [105] M. Stalder, M. Bass, and B. H. T. Chai, "Thermal quenching of fluorescence in chromium-doped fluoride laser crystals," *J. Opt. Soc. Am. B*, vol. 9, no. 12, p. 2271, Dec. 1992.
- [106] J. C. Walling, H. P. Jentsen, R. C. Morris, E. W. O'Dell, and O. G. Peterson, "Tunable-laser performance in BeAl₂O₄:Cr³⁺," *Opt. Lett.*, vol. 4, no. 6, pp. 182–183, 1979.
- [107] J. Walling, O. Peterson, and R. Morris, "Tunable CW alexandrite laser," *IEEE J. Quantum Electron.*, vol. 16, no. 2, pp. 120–121, Feb. 1980.
- [108] S. T. Lai and M. L. Shand, "High efficiency cw laser-pumped tunable alexandrite laser," *J. Appl. Phys.*, vol. 54, no. 10, p. 5642, 1983.
- [109] V. N. Lisitsyn, V. N. Matrosov, V. P. Orekhova, E. V. Pestryakov, B. K. Sevastyanov, V. I. Trunov, V. N. Zenin, and Y. L. Remigailo, "Generation of 0.7-0.8 picosecond pulses in an alexandrite laser with passive mode-locking," *Sov. J. Quantum Electron*, vol. 12., no. 3, p. 368, 1982.
- [110] S. T. Lai and M. L. Shand, "High efficiency cw laser-pumped tunable alexandrite laser," *J. Appl. Phys.*, vol. 54, no. 10, p. 5642, 1983.

- [111] R. Frey, F. de Rougemont, and C. H. Lee, "An Actively Mode-Locked Continuous Wave Alexandrite Laser," *Opt. Commun.*, vol. 73, no. 3, pp. 232–234, 1989.
- [112] R. Scheps, B. M. Gately, and J. M. Myers, "Laser-Diode-Pumped Alexandrite Laser," *Adv. Solid-State Lasers.*, vol. 1, pp. 30-33, 1990.
- [113] C. F. Cline, D. A. Patterson, A. Examiner, and J. F. Niebling, "SYNTHETIC CRYSTAL AND METHOD OF MAKING SAME," U.S. patent 3,912,521, 1975, issued 1975.
- [114] R. C. Powell, L. Xi, X. Gang, and G. Quarles, "Spectroscopic properties of alexandrite crystals," *Phys. Rev. B*, vol. 32, no. September, pp. 2788–2797, 1985.
- [115] R. Ifflander, *Solid-State Lasers for Materials Processing*. Springer, 2001.
- [116] N. M. Trindade, A. Tabata, R. M. F. Scalvi, and L. V. de A. Scalvi, "Temperature Dependent Luminescence Spectra of Synthetic and Natural Alexandrite (BeAl_2)₄:Cr³⁺," *Mater. Sci. Appl.*, vol. 02, no. 04, pp. 284–287, 2011.
- [117] M. Shand and J. Walling, "Excited-state absorption in the lasing wavelength region of alexandrite," *IEEE J. Quantum Electron.*, vol. 18, no. 7, pp. 1152–1155, 1982.
- [118] K. Torizuka, M. Yamashita, and T. Yabiku, "Continuous-wave alexandrite laser pumped by a direct-current mercury arc lamp," *App. Opt.*, vol. 32, no. 36, pp. 7394–7398, 1993.
- [119] H. Samelson, J. C. Walling, and D. F. Heller, "Unique applications of alexandrite lasers," *Adv. Laser Technol. Appl.*, vol. v335, p.p 85-94, 1982.
- [120] F. Vqlker and S. Dong, "Active Q-switching of the alexandrite laser," *Opt. Laser Tech.*, vol. 23, no. 6, pp. 331–334, 1991.
- [121] C. L. Sam, J. C. Walling, H. P. Jenssen, R. C. Morris, and E. W. O'Dell, "Characteristics of alexandrite lasers in Q-switched and tuned operations," *Adv. Laser Eng. Appl.*, vol. 247, pp. 130-136, 1980.

- [122] C. J. Lee, P. J. M. van der Slot, and K.-J. Boller, "A gain-coefficient switched Alexandrite laser," *J. Phys. D. Appl. Phys.*, vol. 46, no. 1, p. 015103, Jan. 2013.
- [123] J. W. Kuper and D. C. Brown, "High efficiency CW green-pumped alexandrite lasers," *Laser and application in science and engineering*, p. 61000T–61000T–8, Feb. 2006.
- [124] R. Scheps, J. F. Myers, T. R. Glesne, and H. B. Serreze, "Monochromatic end-pumped operation of an alexandrite laser," *Opt. Commun.*, vol. 97, pp. 363–366, 1993.
- [125] R. Scheps, B. M. Gately, J. F. Myers, J. S. Krasinski, and D. F. Heller, "Alexandrite laser pumped by semiconductor lasers," *Appl. Phys. Lett.*, vol. 56, no. 23, p. 2288, 1990.
- [126] E. Beyatli, I. Baali, B. Sumpf, G. Erbert, A. Leitenstorfer, A. Sennaroglu, and U. Demirbas, "Tapered diode-pumped continuous-wave alexandrite laser," *J. Opt. Soc. Am. B*, vol. 30, no. 12, p. 3184, Nov. 2013.
- [127] M. E. Innocenzi, H. T. Yura, C. L. Fincher, and R. a. Fields, "Thermal modeling of continuous-wave end-pumped solid-state lasers," *Appl. Phys. Lett.*, vol. 56, no. 19, p. 1831, 1990.
- [128] W. A. Clarkson and D. C. Hanna, "Resonator design considerations for efficient operation of solid -state lasers end-pumped by high-power diode-bars," *Sci. Eng.*, pp. 327–361, 1998.
- [129] W. a. Clarkson and D. C. Hanna, "Two-mirror beam-shaping technique for high-power diode bars," *Opt. Lett.*, vol. 21, no. 6, p. 375, Mar. 1996.
- [130] B. W. Woods, S. A. Payne, J. E. Marion, R. S. Hughes, and L. E. Davis, "Thermomechanical and thermo-optical properties of the $\text{LiCaAlF}_6:\text{Cr}$ laser material," *JOSA.*, vol. 8, no. 5, pp. 970–977, 1991.
- [131] A. Waldman, Z. Rozenberg, O. Braude, and M. Slatkine, "Hair removal by selective photothermolysis with an alexandrite laser." U.S. Patent 5,879,346, issued March 9, 1999.

- [132] T. S. Alster, "Q-switched alexandrite laser treatment (755nm) of professional and amateur tattoos," *American Academy of Dermatology*, vol 33, no. 1, pp. 69–73, 1995.
- [133] M. L. Leuenberger, M. W. Mulas, T. R. Hata, M. P. Goldman, R. E. Fitzpatrick, and J. M. Grevelink, "Comparison of the Q-Switched Alexandrite, Nd:YAG, and Ruby Lasers in Treating Blue-Black Tattoos," *Dermatologic Surg.*, vol. 25, no. 1, pp. 10–14, Jan. 1999.
- [134] N. S. Higdon, E. V. Browell, P. Ponsardin, B. E. Grossmann, C. F. Butler, T. H. Chyba, M. N. Mayo, R. J. Allen, a W. Heuser, W. B. Grant, S. Ismail, S. D. Mayor, and a F. Carter, "Airborne differential absorption lidar system for measurements of atmospheric water vapor and aerosols.," *Appl. Opt.*, vol. 33, no. 27, pp. 6422–38, 1994.
- [135] U. von Zahn and J. Hoffner, "Mesopause temperature profiling by potassium lidar," *Geophys. Res. Lett.*, vol. 23, no. 2, pp. 141–144, 1996.
- [136] J. R. Miller, E. W. Hare, and J. Wu, "Quantitative characterization of the vegetation reflectance model," *Remote Sensing*, vol. 11, no. 10, pp. 1755-1773, 2016.
- [137] E. E. Hoover and J. A. Squier, "Advances in multiphoton microscopy technology," *Nature Phot.*, vol. 7, no 2. 2013.
- [138] W. R. Kerridge-Johns and M. J. Damzen, "Analysis of pump excited state absorption and its impact on laser efficiency," *Laser Phys. Lett.*, vol. 12, no. 12, p. 125002, 2015.
- [139] S. Guch, Jr. and C. E. Jones, "Alexandrite-laser performance at high temperature," *Opt. Lett.*, vol. 7, no. 12, p. 608, Dec. 1982.
- [140] D. Findlay and R. A. Clay, "The measurement of internal losses in 4-level lasers," *Phys. Lett.*, vol. 20, no. 3, pp. 277–278, 1966.
- [141] T. F. Ewanizky and J. M. Craig, "Negative-branch unstable resonator Nd:YAG laser.," *Appl. Opt.*, vol. 15, no. 6, pp. 1465–9, 1976.

- [142] A.-Y. Yao, W. Hou, Y.-P. Kong, L. Guo, L.-A. Wu, R.-N. Li, D.-F. Cui, Z.-Y. Xu, Y. Bi, and Y. Zhou, “Double-end-pumped 11-W Nd:YVO₄ cw laser at 1342 nm,” *J. Opt. Soc. Am. B*, vol. 22, no. 10, p. 2129, 2005.
- [143] I. Yorulmaz, E. Beyatli, A. Kurt, A. Sennaroglu, and U. Demirbas, “Efficient and low-threshold Alexandrite laser pumped by a single-mode diode,” *Opt. Mater. Express*, vol. 4, no. 4, p. 776, Mar. 2014.
- [144] J. Walling, O. Peterson, H. Jenssen, R. Morris, and E. O’Dell, “Tunable alexandrite lasers,” *IEEE J. Quantum Electron.*, vol. 16, pp. 1302–1315, 1980.
- [145] V. Wulfmeyer and J. Bösenberg, “Single-mode operation of an injection-seeded alexandrite ring laser for application in water-vapor and temperature differential absorption lidar,” *Opt. Lett.*, vol. 21, no. 15, p. 1150, Aug. 1996.
- [146] N. Pavel, “In-band pumping of Nd-based solid-state lasers,” *Romanian reports in physics*, vol. 60, no. 4, pp. 995–1012, 2008.
- [147] P. Carbonneau and P. Herve, *fluvial remote sensing for science and management*. John Wiley& Son, 2012.
- [148] A. Stoffelen, G. J. Marseille, F. Bouttier, D. Vasiljevic, S. de Haan, and C. Cardinali, “ADM-Aeolus Doppler wind lidar Observing System Simulation Experiment,” *Q. J. R. Meteorol. Soc.*, vol. 132, no. 619, Part b, pp. 1927–1947, 2006.
- [149] W. E. Baker, G. D. Emmitt, F. Robertson, R. M. Atlas, J. E. Molinari, D. A. Bowdle, J. Paegle, R. M. Hardesty, M. J. Post, R. T. Menzies, T. N. Krishnamurti, R. A. Brown, J. R. Anderson, A. C. Lorenc, and J. McElroy, “Lidar-Measured Winds from Space: A Key Component for Weather and Climate Prediction,” *Bull. Amer. Meteor. Soc.*, vol. 76, no. 6. pp. 869–888, 1995.
- [150] R. E. Avalyan, G.S. Gevorkyan, A.A. Glushko and K.B. Petrosyan, “Powerful Nd: YAG laser for remote sensing”, *Infrared Physics*, vol 29, no. 2-4, pp.213-214, 1989
- [151] Y. Durand, E. Chinal, M. Endemann, R. Meynart, O. Reitebuch, and R. Treichel, “ALADIN airborne demonstrator: a Doppler Wind lidar to prepare ESA’s

ADM-Aeolus Explorer mission,” in Proc. of SPIE, vol. 6296, no. c, p. 62961D–62961D–13, 2006

[152] A. E. Marini, “ATLID: The Technology Development Programme for ESA’s Satellite-borne Atmospheric Lidar,” Earth, 1998.

[153] M. J. Kavaya, S. W. Henderson, J. R. Magee, C. P. Hale, and R. M. Huffaker, “Remote wind profiling with a solid-state Nd:YAG coherent lidar system,” vol. 14, no. 15, pp. 776–778, 1989.

[154] R. S. Afzal, a W. Yu, J. J. Zayhowski, and T. Y. Fan, “Single-mode high-peak-power passively Q-switched diode-pumped Nd:YAG laser.,” Opt. Lett., vol. 22, no. 17, pp. 1314–6, 1997.

[155] R. W. Farley and P. D. Dao, “Development of an intracavity-summed multiple-wavelength Nd : YAG laser for a rugged , solid-state sodium lidar system,” vol. 34, no. 21, pp. 4269–4273, 1995.

[156] W. Krichbaumer, H. Herrmann, E. Nagel, R. Haring, J. Streicher, C. Werner, A. Mehnert, T. Halldorsson, S. Heinemann, P. Peuser, and N. P. Schmitt, “A Diode-Pumped Nd-Yag Lidar For Airborne Cloud Measurements,” Opt. Laser Technol., vol. 25, no. 5, pp. 283–287, 1993.

[157] N. S. Prasad, U. N. Singh, and F. Hovis, “High energy, single-mode , all-solid-state Nd : YAG laser,” pp. 1–5.

[158] P. Piironen and E. W. Eloranta, “Demonstration of a high-spectral-resolution lidar based on an iodine absorption filter.,” Opt. Lett., vol. 19, no. 3, p. 234, 1994.

[159] J. R. Leger and W. C. Goltsos, “Geometrical transformation of linear diode-laser arrays for longitudinal pumping of solid-state lasers,” IEEE J. Quantum Electron., vol. 28, no. 4, pp. 1088–1100, 1992.

[160] S. Yamaguchi, T. Kobayashi, Y. Saito, and K. Chiba, “Collimation of emissions from a high-power multistriple laser-diode bar with multiprism array coupling and focusing to a small spot.,” Opt. Lett., vol. 20, no. 8, pp. 898–900, 1995.

- [161] W. Guo, “Temperature-Control and Characterisation of Diode-Pumped Alexandrite Laser,” Imperial College London, 2014.
- [162] M. Shand and J. Walling, “Excited-state absorption in the lasing wavelength region of alexandrite,” *IEEE J. Quantum Electron.*, vol. 18, no. 1981, pp. 1152–1155, 1982.
- [163] S. M. Kobtsev and N. A. Sventstskaya, “Application of birefringent filters in continuous-wave tunable lasers: a review,” *Opt. Spektrosk.*, vol. 73, pp. 196–212, Jan, 1992.
- [164] C. J. Lee, P. J. M. Van Der Slot, and K. Boller, “A gain-coefficient switched Alexandrite laser,” *App. Phys.*, vol. 46. no. 1, pp. 015103, 2012
- [165] A. Agnesi, S. Dell’Acqua, E. Piccinini, G. Reali, and G. Piccinno, “Efficient wavelength conversion with high-power passively Q-switched diode-pumped neodymium lasers,” *IEEE J. Quantum Electron.*, vol. 34, no. 8, pp. 1480–1484, 1998.
- [166] C. X. Wang, G. Y. Wang, A. V. Hicks, D. R. Dudley, H. Y. Pang, and N. Hodgson, “High-power Q-switched TEM00 mode diode-pumped solid state lasers with > 30W output power at 355nm,” *Proc. SPIE.*, p. 610019, 2006.
- [167] D. Chen and J. Yeh, “Alexandrite laser frequency doubling in f3-BaB crystals,” *Opt. Lett.*, vol. 13, no. 10, pp. 808–810, 1988.
- [168] Y. Mori, Y. K. Yap, T. Kamimura, M. Yoshimura, and T. Sasaki, “Recent development of nonlinear optical borate crystals for UV generation,” *Opt. Mater. (Amst.)*, vol. 19, no. 1, pp. 1–5, 2002.
- [169] H. Search, C. Journals, A. Contact, M. Iopscience, Q. Electron, and I. P. Address, “Generation of 0.7-0.8 picosecond pulses in an alexandrite laser with passive mode-locking,” *Sov. J. Qaun. Elec.*, vol. 12. no. 3, Mar, 1982
- [170] F. Völker, Q. Lü, and H. Weber, “Passive mode-locking of an Alexandrite laser for picosecond pulse generation,” *J. Appl. Phys.*, vol. 69, no. 6, p. 3432, 1991.